Tampere University

TIMO AHO

# Advanced III–V Solar Cells with Back Reflectors

Tampere University Dissertations 342

Tampere University Dissertations 342

## TIMO AHO

# Advanced III–V Solar Cells with Back Reflectors

ACADEMIC DISSERTATION
To be presented, with the permission of
the Faculty of Engineering and Natural Sciences
of Tampere University,
for public discussion in the Auditorium TB109
of the Tietotalo Building, Korkeakoulunkatu 1, Tampere,
on 27 November 2020, at 12 o’clock.

ACADEMIC DISSERTATION
Tampere University, Faculty of Engineering and Natural Sciences
Finland

| | | |
|---|---|---|
| *Responsible supervisor and Custos* | Professor<br>Mircea Guina<br>Tampere University<br>Finland | |
| *Supervisor* | Senior Scientist<br>Antti Tukiainen<br>Tampere University<br>Finland | |
| *Pre-examiners* | Professor<br>Ned Ekins-Daukes<br>University of New South Wales<br>Australia | Doctor<br>Claus Zimmermann<br>Airbus Defence and Space<br>Germany |
| *Opponent* | Professor<br>Antonio Martí<br>Universidad Politecnica de Madrid<br>Spain | |

Cover design: Roihu Inc.

ISBN 978-952-03-1767-6 (print)
ISBN 978-952-03-1768-3 (pdf)
ISSN 2489-9860 (print)
ISSN 2490-0028 (pdf)
http://urn.fi/URN:ISBN:978-952-03-1768-3

PunaMusta Oy – Yliopistopaino
Vantaa 2020

Dedicated to my loving family: Outi, Ronja, Jonna, and Lotta

# PREFACE

The research work in this thesis was carried out at the Optoelectronics Research Centre (ORC) in Tampere University. I would like to express my sincere gratitude to my supervisor Prof. Mircea Guina for the opportunity to work as a part of his excellent research group. Whenever I had difficulties or reached a dead end, he guided me back to the right track. Thank you for your support, trust, and responsibility that you gave to me during these years.

I would like to thank the whole solar cell team for the inspiring atmosphere we have in the group. Especially, I acknowledge my instructor Dr. Antti Tukiainen for having profound discussions about solar cells, semiconductors, and physics with me. Dr. Arto Aho, Riku Isoaho, and all the other growers deserve great thanks for providing excellent solar cell samples. I am truly honored to be part of the solar cell processing team. Therefore, I want to thank Dr. Ville Polojärvi for the guidance and instructions regarding processing steps and Marianna Raappana for the linguistic revision of the manuscripts and the great exactness concerning the research work. We, as colleagues and friends, have faced many ups and downs during the time in ORC and always solved the issues. The chemists have all the solutions. Thank you also to the research assistants in our group for showing such an enthusiasm for the science and for learning. I also thank Joel Salmi for all the fun we had with the plasma machinery and cleaning the cleanroom tables (together with Marianna). Still Dallas theme is the power song when entering the cleanroom. I want to thank all the Semipub people (and the people outside the coffee room) for the interesting and delightful discussions we had. I have enjoyed the time with you a lot. Many thanks also to the laboratory staff: Ilkka, Mervi, Mariia, Maija, Pena, and Jarno, and administrative people: Anne, Eija, and Marketta. You were always there for me and made my life much easier.

An important part of this thesis was conducted in collaboration with Prof. Federica Cappelluti's group from Politecnico di Torino. Thank you Prof. Federica Cappelluti for your valuable input and analysis made for the publications. A special thanks to Dr. Farid Elsehrawy for all the simulation work you have done and your willingness to help me at any time. In addition, thank you for your friendship. It has been a privilege to get to know you.

I express my gratitude to Prof. Tapio Niemi for the ideas and simulation work concerning the optical structures. I acknowledge Prof. Markku Kuittinen, Dr. Ismo Vartiainen, and Khairul Alam from University of Eastern Finland. Their work manufacturing the nanoimprint lithography master for the pyramid grating was essential for the success of this thesis. In addition, I thank all the co-authors that made the publications possible.

I am grateful for the financial support provided by the European Union (TFQD and AMETIST projects) and the European Space Agency. I acknowledge Ulla Tuominen Foundation and Jenny and Antti Wihuri Foundation for their financial support. In addition, I want to acknowledge the doctoral training network in condensed matter and material physics (CMMP) and the doctoral training network in electronics, telecommunications, and automation (DELTA) for their support and funding the conference fees.

I want to express my greatest gratitude to my family: Outi, Ronja, Jonna, and Lotta. Without your continuous support and flexibility, this work would not be finished. I love you.

Tampere, July 2020

Timo Aho

# ABSTRACT

III–V semiconductor solar cells have proven their exceptional performance in terms of conversion efficiency, setting the record to date by exploiting multijunction solar cell architectures. Further advances require deployment of even newer designs, combining emerging materials with optical management of the solar radiation. In addition to the demand to increase the efficiency, beneficial functionalities, for example in space applications, are required such as flexibility, high power-to-weight ratio, or ability to reuse the III–V substrate for decreasing the manufacturing costs. To this end, this thesis concentrates on the development of thin-film III–V solar cell architectures, utilizing back reflectors for increasing the effective absorption length. The methods employed in this study include fabrication and characterization of the back reflectors and the solar cells using standard and in-house developed procedures. In terms of advanced III–V materials enabling more efficient spectral harvesting, this thesis is focused on dilute nitride materials, i.e., GaInNAs and InAs/GaAs quantum dot solar cells. Both approaches aim to increase the absorption beyond the 1 eV spectral range and benefit from the deployment of the back reflectors.

The key enabling result is the development of a planar Ag/Cu back reflector with high reflectance and suitability to be used as a back contact. As an extension of this, a reflector with a polymeric pyramid grating was demonstrated, providing enhanced diffraction of light and resilience to electron irradiation. In terms of demonstrating advanced solar cell architectures, dilute nitride solar cells with back reflector, having bandgap energies of 1 eV and 0.8 eV were fabricated. As a key result, short-circuit current densities enabling current matching in solar cells with three or more junctions were demonstrated. Furthermore, for thin-film InAs/GaAs quantum dot solar cells, the use of a planar back reflector led to two times higher current generation when compared to a standard wafer-based configuration. Although this is an expected result in terms of current generation, the key observation is that the solar cell exhibited an open circuit voltage of 0.884 V, which is one of the highest values reported for quantum dot solar cells grown by molecular beam epitaxy. Finally, a parametrization model enabling simulation of the effect of the reflectors with the pyramid grating was validated on the InAs/GaAs quantum dot solar cell, revealing 12 times higher photocurrent generation in the quantum dot layers.

# TIIVISTELMÄ

III–V-puolijohdeaurinkokennot ovat osoittaneet ylivertaisuutensa aurinkokennoteknologioiden keskuudessa, sillä tämänhetkinen hyötysuhteen maailmanennätys on saavutettu III–V-moniliitosaurinkokennoilla. Hyötysuhteen kasvattaminen vaatii uudenlaisia lähestymistapoja, kuten valon optisen hallinnan hyödyntämistä. Korkeamman hyötysuhteen lisäksi, etenkin avaruussovelluksiin, tavoitteena on uudet ominaisuudet, kuten taipuisuus, korkea tehopainosuhde ja puolijohteen kasvatusalustan uudelleen käyttäminen, jotta valmistuskustannuksia saadaan alennettua. Tämä väitöskirjatyö keskittyy kehittämään ohuiden III–V-puolijohdeaurinkokennojen valonohjausrakenteita, joiden avulla pystytään kasvattamaan absorptiopituutta aurinkokennon sisällä. Tutkimusmenetelmä käsittää takapeilien ja aurinkokennojen valmistamisen ja karakterisoinnin käyttäen olemassa olevia ja työn aikana kehitettyjä menettelytapoja. Tässä työssä tutkitut edistykselliset aurinkokennorakenteet mahdollistavat valon spektrin tehokkaamman hyödyntämisen käyttämällä laimeita typpiyhdisteitä tai kvanttipisteitä, jotka molemmat hyötyvät takapeilien aikaansaamasta absorptiopituuden kasvusta.

Tämän työn päätulokset sisältävät kehitetyn tasomainen korkean heijastuksen omaavan Ag/Cu-takapeilin, joka soveltuu myös virrankeräimeksi. Tämän jatkona kehitettiin polymeeriin valmistettu pyramidirakenteinen takapeili, joka hyödyntää valon diffraktiota ollen lisäksi vastustuskykyinen elektronisäteilytykselle. Jotta pystytiin havainnollistamaan tasomaisen takapeilin toiminta, peili valmistettiin laimeisiin typpiyhdisteaurinkokennoihin, joiden energia-aukot olivat 1 eV ja 0.8 eV. Oikosulkuvirrantiheydet, jotka saavutettiin aurinkokennoille vastaavat virtasovitetun moniliitosaurinkokennon vaatimaa virrantuottoa, joka koostuu kolmesta tai useammasta liitoksesta. Näiden lisäksi, tasomaisen takapeili valmistettiin InAs/GaAs-kvanttipisteaurinkokennoon, josta paksu kasvualusta oli poistettu. Virrantuotto oli kaksi kertaa suurempi kuin ilman takapeiliä, kuten oli oletettu ja aurinkokenno saavutti 0.844 V avoimen piirin jännitteen, joka on yksi korkeimmista raportoiduista arvoista. Lopuksi johdettiin laskentamalli, jota käytettiin arvioitaessa pyramidirakenteiden vaikutusta kvanttipisteaurinkokennon suorituskykyyn. Tulosten perusteella havaittiin merkittävä 12-kertainen kasvu kvanttipisteiden virrantuotossa.

# CONTENTS

# ABBREVIATIONS AND SYMBOLS

| | |
|---|---|
| III–V | Element groups III and V |
| AFM | Atomic force microscopy |
| AM1.5D | Air mass 1.5 diffuse |
| AM1.5G | Air mass 1.5 global |
| ARC | Antireflection coating |
| BSF | Back surface field |
| C | Concentration factor |
| CPV | Concentrated photovoltaics |
| $E_c$ | Energy of the conduction band |
| $E_g$ | Bandgap energy |
| $E_v$ | Energy of the valence band |
| ELO | Epitaxial lift-off |
| EQE | External quantum efficiency |
| FF | Fill factor |
| $\eta$ | Diode ideality factor |
| h | Planck's constant |
| *IV* | Current-voltage |
| $J_{sc}$ | Shot-circuit current density |
| k | Extinction coefficient |
| m | Diffraction order |
| MBE | Molecular beam epitaxy |
| MJSC | Multijunction solar cell |
| MOCVD | Metal-organic chemical vapor deposition |
| $\nu$ | Photon's frequency |
| [N] | The concentration of nitrogen |
| NIL | Nanoimprint lithography |
| PDMS | Polydimethylsiloxane |
| PL | Photoluminescence |
| *pn*-junction | Junction of *p*- and *n*-type semiconductors |
| QD | Quantum dot |

| | |
|---|---|
| QDSC | Quantum dot solar cell |
| SI | Semi-insulating |
| SEM | Scanning electron microscopy |
| SPR | Surface plasmon resonance |
| TLM | Transmission line method |
| $V_{oc}$ | Open-circuit voltage |
| $V_T$ | Thermal voltage |

# ORIGINAL PUBLICATIONS

| | |
|---|---|
| Publication I | T. Aho, A. Aho, A. Tukiainen, V. Polojärvi, T. Salminen, M. Raappana, and M. Guina, “Enhancement of photocurrent in GaInNAs solar cells using Ag/Cu double-layer back reflector”, *Applied Physics Letters*, vol. 109, pp. 251104, 2016. |
| Publication II | T. Aho, M. Guina, F. Elsehrawy, F. Cappelluti, M. Raappana, A. Tukiainen, A. B. M. Khairul Alam, I. Vartiainen, M. Kuittinen, and T. Niemi, “Comparison of metal/polymer back reflectors with half-sphere, blazed, and pyramid gratings for light trapping in III–V solar cells”, *Optics Express*, vol. 26(6), pp. A331–A340, 2018. |
| Publication III | T. Aho, A. Tukiainen, F. Elsehrawy, S. Ranta, M. Raappana, A. Aho, R. Isoaho, F. Cappelluti, and M. Guina, “Back reflector with diffractive gratings for light-trapping in thin-film III–V solar cells”, in Proceedings of *IEEE European Space Power Conference (ESPC)*, Juan-les-Pins, France, pp. 1–4, 2019. |
| Publication IV | T. Aho, F. Elsehrawy, A. Tukiainen, S. Ranta, M. Raappana, R. Isoaho, A. Aho, A. Hietalahti, F. Cappelluti, and M. Guina, “Thin-film InAs/GaAs quantum dot solar cell with planar and pyramidal back reflectors”, *Applied Optics*, vol. 59(21), pp. 6304–6308, 2020. |
| Publication V | R. Isoaho, T. Aho, A. Aho, J. Reuna, M. Raappana, A. Tukiainen, and M. Guina, “High performance low-bandgap (0.8 eV) single junction GaInNAsSb solar cells incorporating Au-based back surface reflectors”, submitted to *Solar Energy Materials and Solar Cells*, 9th of July, 2020. |

# AUTHOR'S CONTRIBUTION

This thesis includes four peer-reviewed journal articles and one peer-reviewed conference proceeding (JUFO 1). The detailed contribution of the author together with all the other authors is described below.

| | |
|---|---|
| Publication I | The author planned the experiments together with Antti Tukiainen. The solar cell structures were grown by Arto Aho. The processing of all the samples was conducted by the author. Ville Polojärvi and Marianna Raappana gave technical support to the processing. SEM images, contact resistance, reflectance, and adhesion measurements were planned and performed by the author. The EQE was measured by the author together with Antti Tukiainen. FIB-EDS measurements were planned and executed by the author and Turkka Salminen. The author analyzed the data together with co-authors. The author was responsible for writing the manuscript. Mircea Guina coordinated the experiments and the manuscript writing process. |
| Publication II | The author planned and designed the diffraction grating structures with Antti Tukiainen and Tapio Niemi. The author fabricated all the samples and measured the reflectance spectra. Marianna Raappana gave technical support to the processing. The diffraction orders were measured by Tapio Niemi. The nanoimprint lithography master was provided by Markku Kuittinen, Ismo Vartiainen, and A. B. M. Khairul Alam. All the simulations were performed by Federica Cappelluti and Farid Elsehrawy. The analysis of the results was conducted by the author and Federica Cappelluti. The author has written the manuscript. Mircea Guina contributed to the manuscript writing process. |
| Publication III | The author planned the experiments and processed all the samples. The processing was supported by Marianna Raappana. The solar cell structures were grown by Arto Aho, Riku Isoaho, and Sanna Ranta. The author has guided the simulations work, which was carried out by Federica Cappelluti and Farid Elsehrawy. The electron irradiation experiments were designed by the author together with Antti Tukiainen. The author performed the current-voltage and |

reflectance measurements and Riku Isoaho measured the external quantum efficiency. The author was responsible for writing the manuscript together with Mircea Guina's assistance.

Publication IV The author designed and processed the samples. Marianna Raappana supported the processing. The semiconductor samples were grown by Arto Aho, Riku Isoaho, and Sanna Ranta. Federica Cappelluti and Farid Elsehrawy performed the simulations. The author measured the one sun current-voltage characteristics while the concentrated measurements were performed by Arttu Hietalahti and external quantum efficiency measurements by Riku Isoaho. The analysis of the results was performed by the author together with Antti Tukiainen and Federica Cappelluti. The author was responsible for writing the manuscript. Mircea Guina coordinated the experiments and the manuscript writing.

Publication V The author designed the processing steps of the samples. The solar cell structures were grown by Riku Isoaho and Arto Aho. The samples were processed by the author, Marianna Raappana, and Jarno Reuna. The measurements were conducted by the author, Riku Isoaho and Jarno Reuna. The author was partly involved in analyzing the data and gave input to the manuscript while Riku Isoaho was responsible for the manuscript writing process. Mircea Guina and Antti Tukiainen coordinated the experiments and finalized the manuscript writing process.

# 1 INTRODUCTION

The need for energy production using renewable sources has increased in recent years pushed by political, economic, and social factors. As a part of this trend, an increasing amount of the energy needed will be produced by various photovoltaic technologies exploiting the abundance of solar energy. Harvesting solar energy with solar cells has shown potential in terrestrial energy production and is the main source of energy for space applications. For decades, the production of solar energy has been dominated by silicon solar cells owing to the availability of the raw material, appropriate properties, and relatively low fabrication costs [1]. On the other hand, solar cells based on more advanced III–V compound semiconductor materials have substantially higher conversion efficiency compared to silicon solar cells albeit they are more complex and have higher fabrication costs. So far, the highest conversion efficiency for a silicon solar cell is 27.6% [2], whereas a III–V semiconductor solar cell exploiting a multijunction solar cell (MJSC) approach [3] has set the world record efficiency of 47.1% [4].

In addition to III–V solar cells, there are other notable solar cell technologies that are developing rapidly. For example, perovskite solar cells have steeply increased their record efficiency during the past few years as shown in Figure 1. When the overall performance including availability and cost are considered, each solar cell technology has their different target applications. Thus, silicon solar cells are optimal solution for terrestrial operation (Figure 2(a)) due to their continuously decreasing cost, being currently at the level of 500 €/kW of peak power [5]. On the other hand, space applications, e.g., GPS satellites or space stations (Figure 2(b)), require solar cells with high efficiency and high power-to-weight ratio, indicating MJSCs to be the optimal choice [6]. Moreover, since in space the solar cells are in a harsh environment, the III–V materials are more suitable owing to their good radiation tolerance compared to silicon solar cells [7, 8]. MJSCs can meet the good cost level for terrestrial energy production by concentrated photovoltaics (CPV) systems in which the sun light is guided from a larger area to solar cells with the help of lenses or mirrors [9], reducing the material costs of the solar cells. On the other hand, CPV operation requires a sun tracking system, imposing the economic viability.

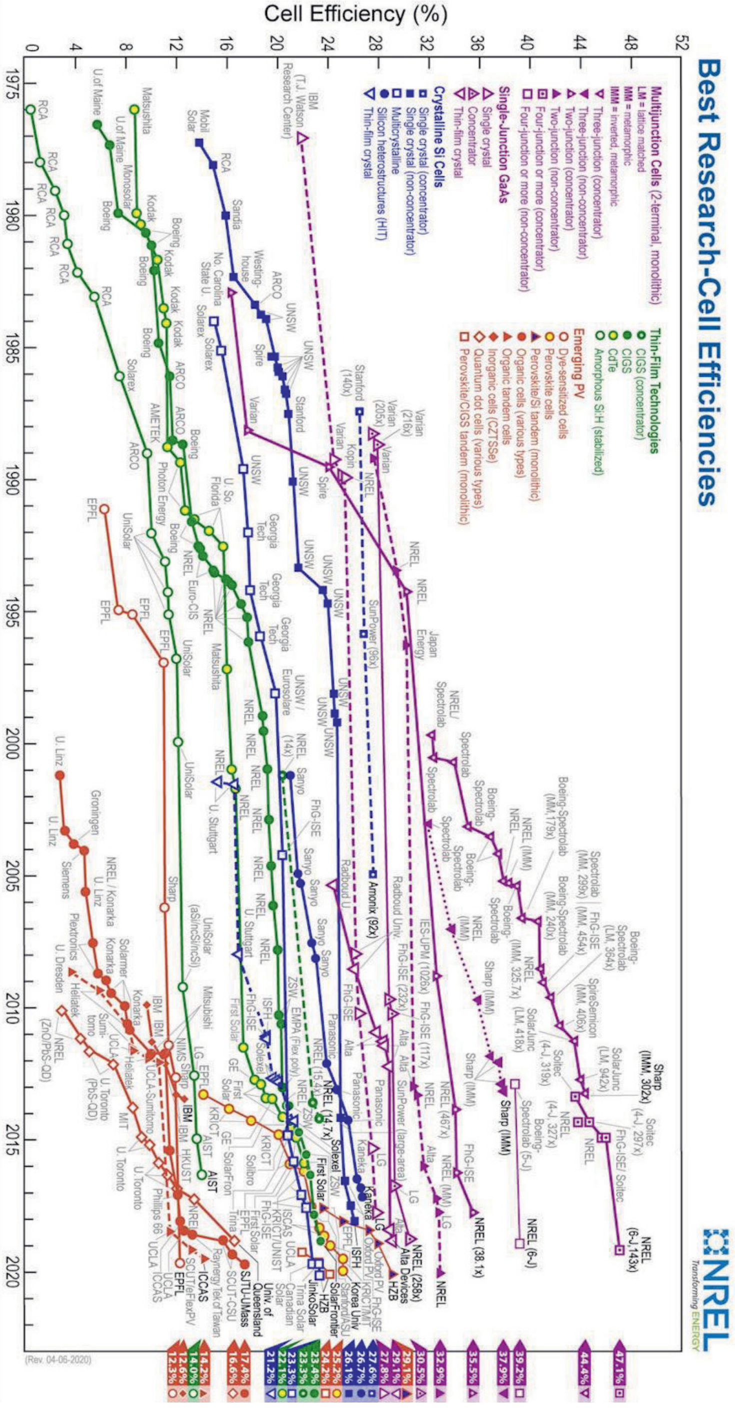

**Figure 1.** Progress of record efficiencies for various solar cells technologies [10]. This plot is courtesy of the National Renewable Energy Laboratory, Golden, CO.

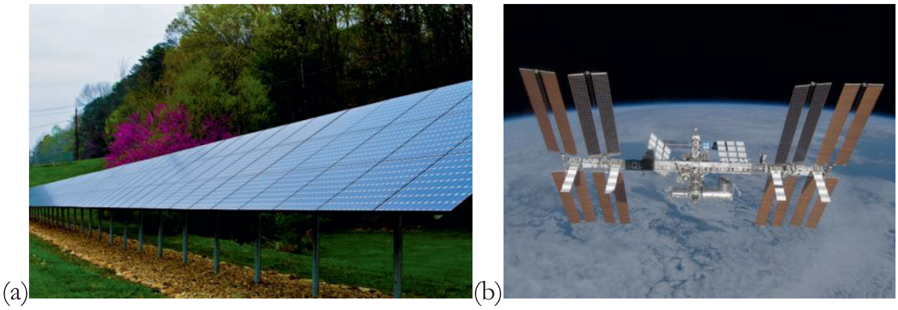

**Figure 2.** (a) Terrestrial solar panels [11], and (b) solar panels in ISS space station [12].

The continuous development of III–V MJSC technology has reached a high level of maturity in industrial scale using designs with three junctions, i.e., GaInP/GaAs/GaInAs or GaInP/GaAs/Ge, which reach efficiencies of over 30% for space [13] and over 40% for CPV [14]. However, these achievements are still far from the theoretical potential which can be fulfilled by more advanced spectral harvesting, e.g., using higher number of junctions [15].

The generic strategy for increasing the conversion efficiency of the MJSCs requires decreasing the transmission and thermalization losses. This can be achieved by exploiting materials that are optimized in terms of bandgap energy for the photon energy of different spectral bands. To this end, this thesis pursues two approaches. The first approach concentrates on dilute nitride materials, i.e., GaInNAs(Sb) for which the bandgap energy can be tuned while the lattice constant stays matched to GaAs or Ge substrate materials [16]. This brings further benefits in terms of lower detrimental dislocations compared to the established MJSC approaches, e.g., metamorphic design [16-18]. However, due to the limitations of the low bandgap dilute nitride materials (section 2.1.2), the photocurrent generation needs to be enhanced to meet the current matching conditions [19]. This enhancement in photocurrent can be achieved by introducing a reflector on the backside of the solar cell in order to guide the light that has passed the absorbing layers back to the active area. A generic drawing of the solar cell with back reflector is presented in Figure 3.

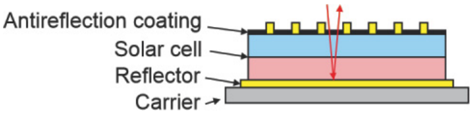

**Figure 3.** A generic drawing of the thin-film solar cell with back reflector.

A second approach exploits single junction architectures, i.e., GaAs-based quantum dot solar cells (QDSCs) which would also benefit from the light-trapping concept to increase the absorption efficiency. In particular, InAs quantum dots (QDs) render possible to enhance the infrared spectral response of single junction GaAs solar cells, thus increasing their short-circuit current densities ($J_{sc}$) [20-22]. They also bring more options for tuning the bandgap in MJSCs to realize the current matching conditions [23, 24]. However, for attaining the theoretical efficiency, several challenges related to the relatively modest absorption provided by the QDs have been recognized [25]. In order to enhance the absorption, a high number of QD layers is required [26], yet the fabrication of such structures with high crystalline quality is challenging, causing a decrease in the open-circuit voltage ($V_{oc}$) [21, 25, 27]. By using only few QD layers (~10 layers), the degradation of $V_{oc}$ could be prevented but consequently the current enhancement remains modest [28, 29]. This could be alleviated by employing a reflector on the backside of the QDSC in order to increase the absorption length and the photocurrent. The properties of the back reflector can be modified by texturing the reflector [30, 31], which will produce multiple passes through the absorbing layer enhancing the photocurrent, thus trapping the light inside the solar cell. QDSCs have been demonstrated with both planar [32, 33] and textured back reflectors [34].

Finally, light management using integrated back reflectors requires a thin-film architecture employing substrate removal, which brings additional benefits for applications where flexibility and high power-to-weight ratio are needed, such as high-altitude unmanned aerial vehicles [35, 36]. Furthermore, to better exploit light-trapping, in addition to the textured back reflector, a nanostructured antireflection coating (ARC) should be considered [37-39]. Basically, the light-tapping structures could be used in any type of solar cells. Since the structures are designed for specific wavelength range, the dimensions of the gratings need to be optimized for each solar cell type individually [40].

## 1.1 Research objectives

The aim of this thesis is to study, develop, fabricate, and characterize light-trapping structures for advanced III–V solar cells. These structures and fabrication methods could provide the needed advancement in order to reach the MJSC efficiency of over 50%. The specific objectives can be divided into three main thematic areas, which include: i) back reflector technology including studying their feasibility for space operation, ii) the implementation of the reflectors to dilute nitride solar cells, and iii) the implementation of the reflectors to QDSCs.

In general, the design and the implementation of back reflector is motivated by the aim to enhance the photon absorption owing to an increased optical path inside the absorbing layer of the solar cell. This comprises the determination of the suitable planar back reflector and the study of the optimal gratings in order to induce light diffraction inside the solar cell. The key research questions are related to:

i) How are the optical and electrical properties of the back reflectors linked with the structural differences of the reflectors?

ii) Is the developed back reflector technology feasible in terms of the fabrication process steps involved in manufacturing of advanced solar cells based on dilute nitrides and QDs?

iii) How can the parametrization of intrinsic photovoltaic properties, emerging from the results of the QDSCs with back reflector, be exploited in the development of the simulation tool for QDSCs with back reflector?

## 1.2 Approach and structure of the thesis

The thesis introduces advanced III–V semiconductor solar cells, i.e., dilute nitride junction of the MJSCs and QDSCs. In addition to the properties of the planar and textured back reflectors, the utilization of the back reflectors to the advanced solar cells is illustrated. In Figure 4, the approach of the thesis along with the publications is presented as a step-scheme illustration.

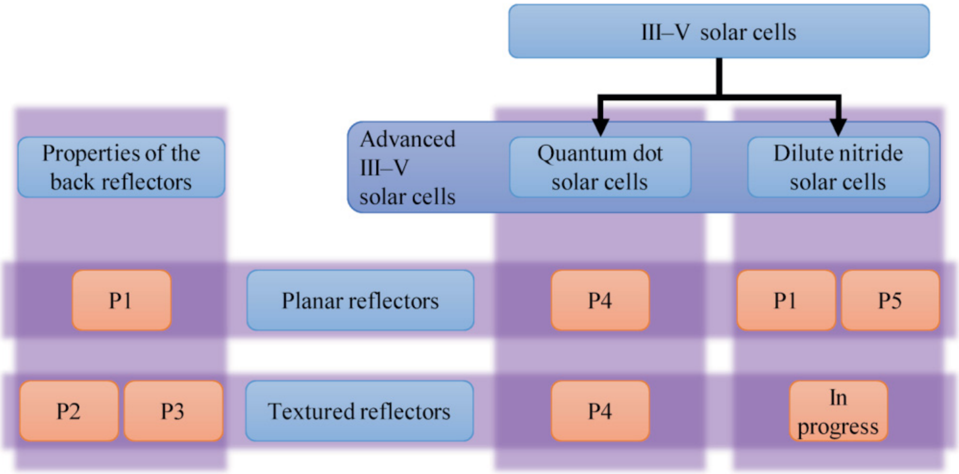

**Figure 4.** Approach of the research presented as a step-scheme illustration. P1–P5 are referring to the publications I–V.

The thesis is divided into following sections:

**Chapter 2** explains the principals of the III–V semiconductor solar cells and the motivation for the necessity of the photon management in these solar cells. Here, the emphasis is in dilute nitride junction of the MJSC and the InAs/GaAs QDSCs.

**Chapter 3** provides a detailed description of the experimental work executed with the planar and textured back surface reflectors. The development of the structures and the characterization results are discussed to define the optimal structure to be utilized in solar cells. In addition, the technical aspect of the fabrication process is described, e.g., the substrate removal by epitaxial lift-off or by etching the substrate. This chapter includes also the irradiation results for the back gratings.

**Chapter 4** covers the implementation of the back reflectors to the dilute nitride solar cells and into the QDSCs.

**Chapter 5** is the conclusion which collects the key results of the thesis. Also, possible future research is discussed.

**Original publications** are collected in the end of the thesis. There are five publications in total. Publication **I**, denoted later as [P1], covers the planar metal reflector study to determinate the properties of the metal reflectors. In Publication **II**, denoted later as [P2], the grating structures for the diffractive back reflectors were fabricated and characterized. The electron irradiation results for diffractive gratings are presented in Publication **III**, denoted later as [P3]. In Publications **IV** and **V**, denoted later as [P4] and [P5], respectively, the planar and diffractive reflectors are utilized in InAs/GaAs QDSCs and narrow bandgap dilute nitride solar cells.

# 2 BACKGROUND CONCEPTS FOR III–V SEMICONDUCTOR SOLAR CELLS

III–V semiconductor solar cells are typically based on absorbing materials placed within a *pn*-junction composed of elements in groups III and V of the periodic table [41]. The photons with an energy higher than the bandgap energy ($E_g$) of the absorbing materials generate electron-hole pairs, which are then separated by the electric field of the *pn*-junction. The electrons move to the surface of the solar cell and are collected by a metal contact on the frontside of the solar cell from which the electrons travel though an external circuit creating an electric current. However, the electrons may also fall back from the conduction band having energy $E_c$, to an empty state in the valence band having energy $E_v$, through an electron-hole recombination, which becomes more probable the longer the path is between the formation site of the electron-hole pair and the depletion region [41]. The generic absorption processes of photons are schematically presented in Figure 5 for the case of GaAs, the most common III–V semiconductor materials, which has a direct bandgap with the $E_g$ of 1.42 eV [42]. For clarity, it should be noted that all the photons with energy lower than $E_g$ are not participating to the current generation. This issue is alleviated by exploring bandgap tailoring offered by GaAs-based III–V compounds, which have enabled the advance of MJSC architectures.

III–V semiconductors used in MJSCs include a wide range of compositions such as GaAs, GaInP, GaInAs, and AlGaAs. Other compounds are presented in Figure 8. These materials are fabricated by metal-organic chemical vapor deposition (MOCVD) or by molecular beam epitaxy (MBE) [43, 44]. Both methods have their benefits yet MOCVD has been adopted in production of MJSCs largely owing to the higher growth rate. On the other hand, MBE has been used in research environment and recently has gained popularity for ability to deposit dilute nitride materials, which offer improved wavelength coverage to design MJSCs [45]. The epitaxial layers are commonly grown on top of GaAs, Ge, or InP substrates whose crystal structure the epitaxy is adapting.

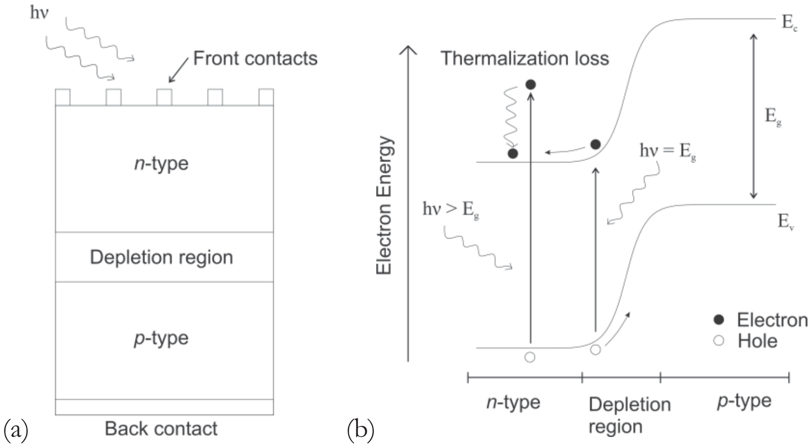

**Figure 5.** (a) A simplified presentation of the GaAs *pn*-junction with the depletion region in between. (b) A schematic band diagram of the GaAs *pn*-junction showing the formation of an electron-hole pair when absorbing a photon, where h is the Planck's constant and ν is the photon's frequency.

Following the epitaxial growth, the fabrication of the III–V semiconductor solar cells includes deposition of metal contacts. The front contact needs to be patterned in order to enable the light to enter the solar cell. In addition, the solar cell perimeter is etched to create an electrical isolation between the front and the backside, forming the so-called mesa structure. Moreover, an ARC is typically deposited on the front surface in order to minimize the reflection of the incident light. Final step includes mounting the solar cell to a submount by soldering, and the front contact is wire bonded to the external connectors of the submount (see Figure 6). [46]

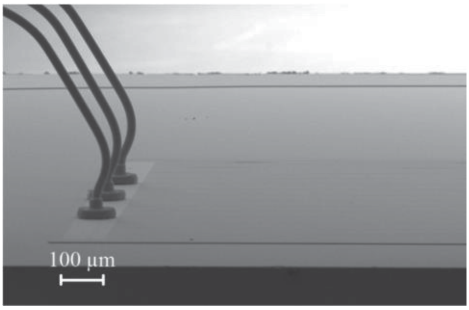

**Figure 6.** A solar cell with wires bonded to the front contact. The mesa of the solar cell can be seen as a thin layer, while all the other area around the mesa is substrate [47].

## 2.1 Multijunction solar cells

Single junction solar cells are not able to harvest the whole solar spectrum due to the use of single bandgap material. This causes either significant transmission losses for photons with energy lower than $E_g$ or thermalization losses for the photons with significantly higher energy than $E_g$. Thus, the theoretical maximum conversion efficiency, defined by the Shockley-Queisser limit [48], reaches a value of ~32% for Si solar cells while for GaAs single junction solar cell the corresponding value is ~33.5% at the air mass 1.5 global (AM1.5G) solar spectrum [49, 50]. Although this value is somewhat far from the current demonstration, i.e., 29.1% for GaAs solar cell [2], the III–V materials render possible development of multijunction concept, in which the solar spectrum is divided between multiple solar cells with different $E_g$ values combined within a single device. The solar spectrum can be divided either externally using dispersive optics or internally within the solar cell [43]. In the internal partitioning configuration, the junctions of the solar cell are stacked one on top of the other, as schematically presented in Figure 7. It should be noted, that while each sub-cell requires a *pn*-junction configuration, the different parts can be stacked together via the use of tunnel junctions [43].

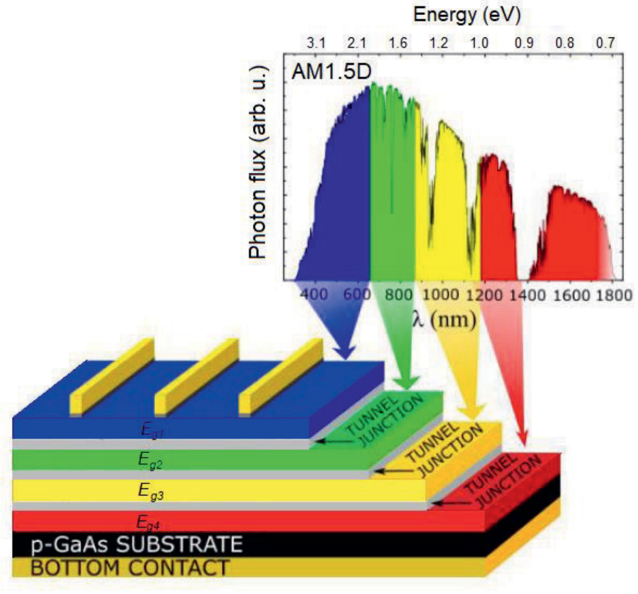

**Figure 7.** MJSC with four junctions that are absorbing different part of the solar spectrum. The air mass 1.5 diffuse (AM1.5D) solar spectrum is presented according to ASTM G173-03 [51].

The stacking imposes strict requirements in terms of current matching conditions meaning that the current of the solar cell will be the limited by the least generating junction, and in terms of ensuring that all the materials can be grown on the same substrate [52]. This limits the selection of the semiconductor materials available. To alleviate this limitation, two approaches have been widely adopted: i) so-called metamorphic solar cell, in which buffer layers are used to accommodate the lattice mismatch between different parts of the solar cell, and ii) lattice matched approach, in which all the layers in the solar cell are preserving the lattice of the substrate.

The lattice matched structure has been largely adopted for early phase architectures with two junctions, i.e., GaInP/GaAs solar cell, and represents also the most mature commercial technology used in fabrication of triple-junction solar cells, i.e., GaInP/GaAs/GaInAs solar cells, used in space and CPV applications [3, 53]. In this concept, the lattice constant of the monolithically grown crystal is equivalent to the lattice constant of the substrate. Consequently, there is no formation or minimal level of strain in the crystal lattice, making them of highest quality [3, 43]. On the other hand, metamorphic approach represents emerging commercial technology for solar cell with three junctions and improved spectral coverage [3, 43]. A lattice matched option would be generally preferred, giving the potential for simpler epitaxy and reduced defect density, yet the choice of the materials enabling a broad enough absorption has been an issue until the recent demonstration of dilute nitride solar cells [54-57]. One key advantage in the favor of lattice matched approach is the possibility to use only one type of a tunnel junction, while the metamorphic design needs different tunnel junctions for material with different lattice constant [43, 46].

In addition to these two approaches, a hybrid approach should be noted which is based on mechanically stacking different lattice matched solar cells, grown on different substrates, which are then bonded together. Contrary to the lattice matched and metamorphic configurations, the current produced by the junctions does not need to meet the current matching conditions when a four terminal design is used [43]. MJSCs based on wafer bonding configuration have achieved high efficiencies [58], but the challenge has been the reliable bonding of the two wafers together without any voids and in general the relatively higher fabrication costs. Although much effort has been made in improving the yield of the wafer bonding, this technology has not been yet adopted in volume commercial applications [59].

## 2.2 Lattice matched dilute nitride solar cells

The bandgap energy dependence versus lattice constant of some typical compound semiconductors are presented in Figure 8. The connecting lines give a guideline for tuning possibilities of the bandgap energy or the lattice constant.

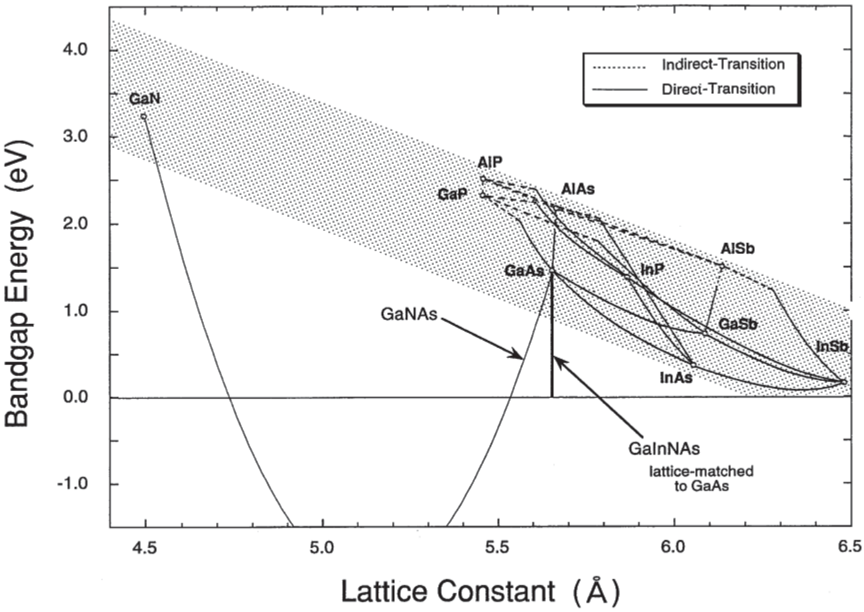

**Figure 8.** Bandgap energies of III–V semiconductors as a function of the lattice constant. The dilute nitrides have the GaAs lattice constant while the bandgap is tuned [60].

For lattice matched MJSCs with four or more junctions, GaInNAs(Sb) compounds have emerged as the solution of the choice for the narrow bandgap junction (bottom junction), while having the lattice constant of GaAs and Ge [16, 19]. It should be noted that this is valid when MBE technology is deployed [54, 56, 57, 61], however the fabrication of dilute nitride solar cells by MOCVD has been impaired by the presence of a high background doping related to impurities of C [62, 63].

As presented in Figure 8, the lattice constant of the dilute nitride materials stays unchanged while the bandgap energy can be optimized from approximately 0.8 to 1.42 eV to meet the current matching conditions [16, 61, 64, 65]. The tuning of the $E_g$ is achieved by changing the concentration of N ([N]), i.e., higher [N] corresponds to lower $E_g$ values, and [N] as high as 8% have been demonstrated, corresponding the $E_g$ of 0.73 eV [55]. The external quantum efficiency (EQE), which describes the amount of generated current when irradiated by photons of specific wavelength, of state-of-the-art GaInNAsSb solar cells grown on GaAs substrate is presented in Figure 9. Despite the relatively high EQE values compared to narrow bandgap dilute nitride solar cells reported earlier [66], it is clear that for solar cell with the lowest $E_g$ value of 0.73 eV, the defects associated with N incorporation significantly affect the EQE ultimately leading to limitations in the overall thickness that can be deployed in the MJSC.

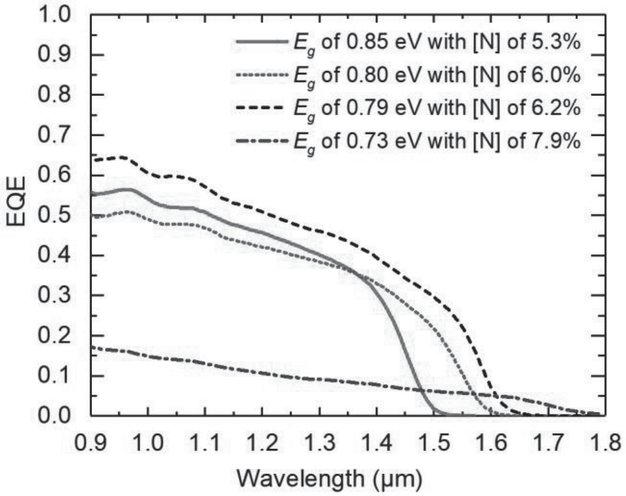

**Figure 9.** EQE of state-of-the-art dilute nitride solar cells with different [N]. The $E_g$ values are estimated from the derivatives of the EQE curves. The data is adopted from [55].

When using dilute nitride materials, a *p-i-n* structure is preferred instead of a *pn*-junction due to the short diffusion lengths of the minority carriers [61, 67]. The *p-i-n* structure has an intrinsic material deposited in between the *pn*-junction in order to increase the thickness of the depletion region (see Figure 5). Therefore, more photons are absorbed and extracted by the electric field in the *i*-region [41]. Dilute nitrides with higher than 4% of [N] induce relatively low charge carrier lifetimes (below 1 ns), which leads to short minority carrier diffusion lengths of under ~1 μm [68-70]. In addition, the high [N] results in high *p*-type background doping level of $10^{16}$ $cm^{-3}$ or higher, narrowing the depletion region. These effects limit the thickness of the absorption layer, resulting in lower quantum efficiencies [69-72]. On the other hand, this issue can also be mitigated by adding a reflector on the backside of the solar cell, allowing the use of a thinner absorber but still generating the required photocurrent to meet the current matching conditions in MJSCs [73]. **Development**

**and deployment of such back reflectors to dilute nitride solar cells represents a major goal of this thesis.**

## 2.3 Quantum dot solar cells

To enhance the spectral coverage of single junction GaAs solar cells, InAs QDs can be employed in the solar cell structure [28]. Such nanostructures are very attractive for band-engineering enabling a translation of the absorption edge to longer wavelengths, thereby exploiting so-called sub-bandgap transitions to absorb the low energy photons improving $J_{sc}$ [20]. In addition, with careful design, QDSCs can be exploited to realize the intermediate band operation [22]. Similarly to dilute nitride solar cells, the QDs are embedded into an intrinsic region of the *p-i-n* GaAs solar cell structure as presented in Figure 10.

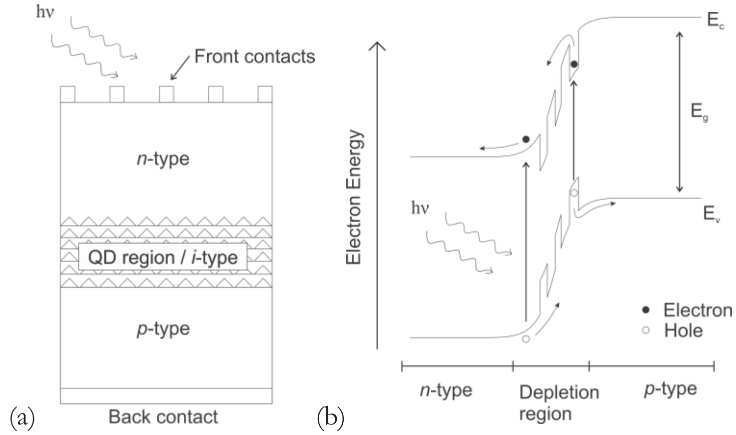

**Figure 10.** (a) A schematic structure of a solar cell with QDs embedded into the intrinsic region. (b) A simplified band diagram of a QDSC. The data is adopted from [20].

One QD layer has relatively low absorption of photons due to the small volume of the QDs [25]. For that reason, a high number of QD layers is needed for achieving a noticeable increase in $J_{sc}$. In Figure 11, exemplary photoluminescence (PL) signal and the EQE of QDSCs are presented as a function of the number of the QD layers. The increase in the PL signal intensity is significant when 5 QD layers are compared to 20 QD layers. This reveals that a sufficient number of QD layers is needed when QDSCs are designed. However, when the number of the QD layers in the QDSC is increased, strain in the solar cell structure accumulates [74], causing detrimental dislocation defects. Figure 12 presents microscopy images of InAs/GaAs QDSCs with 10 and 20 QD layers showing that the solar cell with 10 QD layers has only a few surface defects, and no dislocation lines are present. However, the solar cell with 20 QD layers has several dislocation lines apparent. This indicates that for 20 QD layers the accumulated compressive strain exceeds the threshold for dislocation formation. The strain can be reduced by growing fewer QD layers, which would limit the current generation, or by deploying strain management that will complicate the fabrication [74-76].

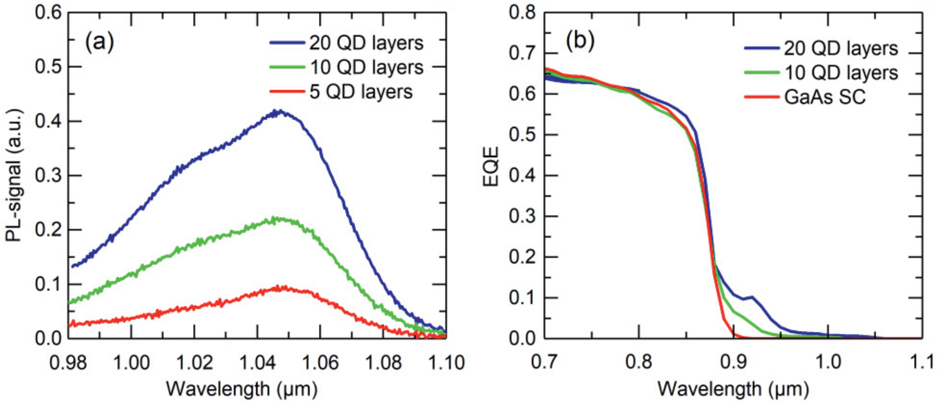

**Figure 11.** (a) PL signal of an InAs/GaAs QDSC with different number of QD layers. (b) The EQE of a GaAs solar cell, a QDSC with 10 QD layers, and a QDSC with 20 QD layers. The data is adopted from [75].

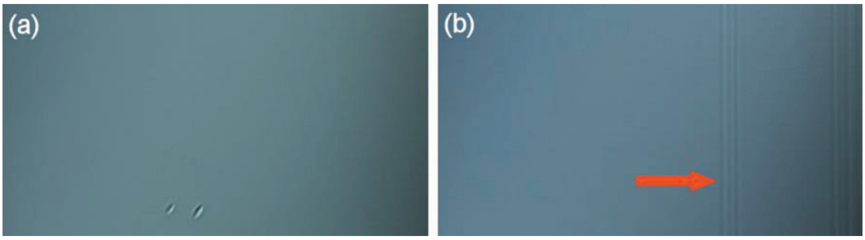

**Figure 12.** Optical microscope images of QDSCs with (a) 10 QD layers, and (b) 20 QD layers in 50× magnifications. The red arrow points out the dislocation lines. The data is adopted from [75].

With a high number of QD layers (>20 layers), $V_{oc}$ tends to decrease due to the defects caused by the strain, and the decrease is also inherently related to the narrower bandgap of the QDs [21, 25, 27]. Indeed, when using only a few QD layers, the $V_{oc}$ degradation stays marginal [28, 29], but then the current generation ability is severely affected. This limitation can be alleviated again by implementing a back reflector to enhance effective absorption in the QD layers [77]. **Development of planar [32, 33] and textured back reflectors [34] and their assessment in terms of effectiveness in improving the current generation of QDSCs has been a second major goal of this thesis.**

## 2.4 Thin-film III–V solar cells

The standard III–V solar cells are commonly referred as a “wafer-based” technology since the junction materials are grown on a relatively thick GaAs or Ge substrate. The substrate thickness is in the range of 100–500 μm while an only few μm layer forms the absorbing region of the solar cell. However, utilization of a back reflector to increase the effective absorption requires a thin-film design which involves removing the substrate and deposition of the reflector in the proximity of the absorbing region. Basically, there are two technologies to execute the substrate removal: i) the substrate is thinned by mechanical lapping followed by wet etching of the rest of the substrate, or ii) by using a sacrificial layer to release the solar cell structure from the substrate, the so-called epitaxial lift-off (ELO) technique [78].

When using mechanical lapping, the substrate is lost without a possibility to reuse it. Lapping is performed with commercial equipment which nowadays have high accuracy, at the micrometer scale [79]. Lapping rate is controlled by rotation speed, the size of the abrasive particles, and pressure, which is sample size dependent. If the rate is too fast, dislocation lines or cracks may form. For a GaAs substrate, the acceptable rate is approximately 10 μm/min, but the rate differs for Ge, GaSb, and InP substrates. The GaAs substrate can be thinned down to the thickness of approximately 100 μm to avoid forming the cracks that the robust mechanical method may produce. The rest of the substrate is wet etched with suitable solutions. For GaAs substrate, the etchant can be, e.g., $H_2SO_4$:$H_2O_2$:$H_2O$ with the volume ratios of 1:5:1 using strong acids, having an approximate etch rate of 10 μm/min. However, there are also many other options for etching GaAs [80]. This type of substrate removal requires an etch stop layer in the solar cell structure to be able to terminate the etching leaving the solar cell otherwise untouched. Furthermore, the substrate can be removed by using wet etching alone which may be challenging due to the nonuniform etching originating from the diffusion controlled nature of the etching [81]. It should be noted, that before the etching step the solar cell is bonded to a carrier to be able to handle the thin-film structure.

The ELO process is based on the separation of the III–V structures from their original substrate and transferring them to a low cost carrier, e.g., glass or plastic [78, 82, 83]. The advantage is the possibility to reuse the substrate, potentially lowering the fabrication costs of the III–V solar cells [84]. Different ELO processes have been developed by several research groups [85-92]. An exemplary simplified ELO process flow for an inverted III–V solar cell is presented in Figure 13. In the inverted configuration, the epitaxial layers of the solar cell are fabricated in reverse order, i.e., upside down, to be able to process the backside of the solar cell before the ELO step.

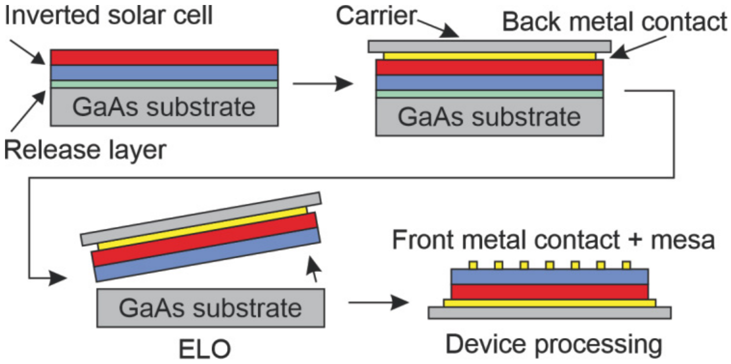

**Figure 13.** Schematic ELO process flow of an inverted solar cell on GaAs substrate. The release layer is selectively etched in the ELO step.

The ELO process requires the growth of the release layer before the absorbing layers of the solar cell. During the selective wet etching of the release layer, the rest of the solar cell structure stays untouched enabling further processing to complete the device. One typically used release layer material is AlAs, being selectively etched with HF solution [93]. Another option for the material is AlInP, using an HCl solution for selective etching [90]. One challenge in ELO has been the etch rate of the release layer which must be in a decent level to be able to separate larger areas. However, ELO has been demonstrated to release solar cells from the substrate with the diameter of even 6 inches [94]. Figure 14 presents examples of the 2-inch and 4-inch ELO layers and processed flexible thin-film solar cells.

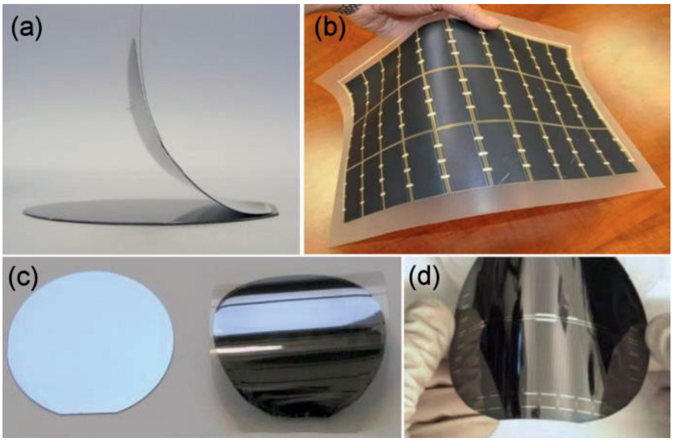

**Figure 14.** (a) A 4 inch thin-film structure on a flexible carrier after ELO [75]. (b) A thin-film GaAs solar cell array in a flexible sheet [95]. (c) A 2 inch substrate and the released III–V solar cell structure after ELO [75]. (d) ELO-processed flexible GaAs solar cells (diameter 4 inch) [95].

Thin-film configuration enables the implementation of various light-trapping strategies, aiming at bouncing of the light back and forth inside the active area of the solar cell. Figure 15 presents a schematic drawing of generic light-trapping approaches, in which different types of reflectors and ARCs are used [96, 97]. With a planar reflector and a planar ARC, the absorption length is doubled whereas with a textured back reflector and textured ARC, the absorption length can be much higher owing to the scattering mechanisms.

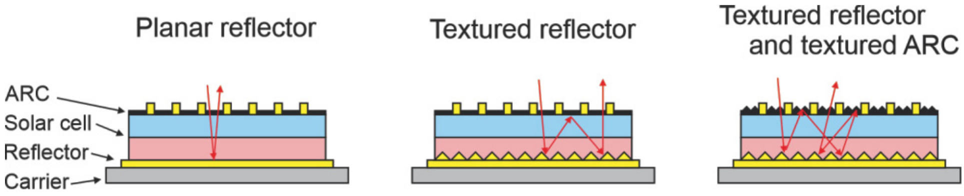

**Figure 15.** A schematic drawing of the light-trapping cases with planar and textured reflectors and the light-trapping with textured reflector and textured ARC.

While the development of various back reflector technologies has been the subject of this thesis work and will be discussed in the subsequent section, it has to be noted that the design of the ARC plays an important role for achieving efficient light-trapping [98]. Conventional ARCs with single- or double-layer dielectric coatings include $SiN_x$, $ZnS/MgF_2$, and $TiO_x/SiO_x$ [98]. Currently, even up to 5-layer dielectric AR coatings are demonstrated [99]. The challenge with purely planar AR coatings is that the reflectance has relatively high angular sensitivity [100]. The angular sensitivity can be reduced and a low broadband reflectance can be achieved by a textured ARC, and the surface reflectance of average 3% in the wavelength range of 400–1400 nm has been demonstrated with textured ARC [37]. In most cases, the fabrication process of the nanostructured ARC requires precision and expensive equipment. However, a simple and an inexpensive nanostructuring process, which is suitable also to be applied to large areas, has been demonstrated [38].

To define the background framework for developing the advanced thin-film solar cells, one of the leading results includes a thin-film GaAs solar cell without substrate which have exhibited the world record efficiency of 29.1% among the single junction solar cells at AM1.5G spectrum [2]. In addition, several thin-film MJSC designs with three junctions have been demonstrated [101, 102] and the conversion efficiency as high as 37.8% at AM1.5G has been achieved [103]. Recently, an effort has been made to fabricate thin-film four junction solar cells [103, 104] reaching the efficiency of 34.3% at AM1.5G spectrum. Moreover, thin-film lattice matched MJSCs with dilute nitride junctions and thin-film MJSCs with QDs have been demonstrated [105, 106].

# 3 DEVELOPMENT OF BACK REFLECTORS

This chapter describes the design, fabrication, and characterization of planar and structured back reflectors developed during the thesis work. The first section introduces planar back reflectors [P1] as the key building block targeting the achievement of high reflectivity and good ohmic contact. The second section focuses on the design and fabrication of the structured back reflectors developed for light diffraction [P2]. In addition, the properties of the diffraction gratings are discussed. In the third section, the electron irradiation results of the reflectors with back gratings are presented [P3].

## 3.1 Planar back reflectors

In thin-film III–V solar cells, the metal back contact acts also as a back reflector increasing the absorption length, enabling the use of a thin absorbing layer without sacrificing the current generation. In addition to the increased current generation enabled by the reflector, the $V_{oc}$ will theoretically increase as a consequence of higher effective light concentration in the junction [49]. This effect is presented in Figure 16 which reveals the $J_{sc}$, $V_{oc}$, and conversion efficiency increase in a GaAs solar cell as a function of reflectivity of the back reflector. As seen from the figure, the highest improvement is achieved in the region where the reflectivity is over 90% due to the steep increase of the $V_{oc}$. In order to achieve the desired improvement, a careful design of the reflector is essential. This is not a trivial task when aiming at achieving desired reflectivity, and good ohmic contact while avoiding undesired effects, such as diffusion of the metal into the semiconductor material. These aspects are discussed in the next section to follow.

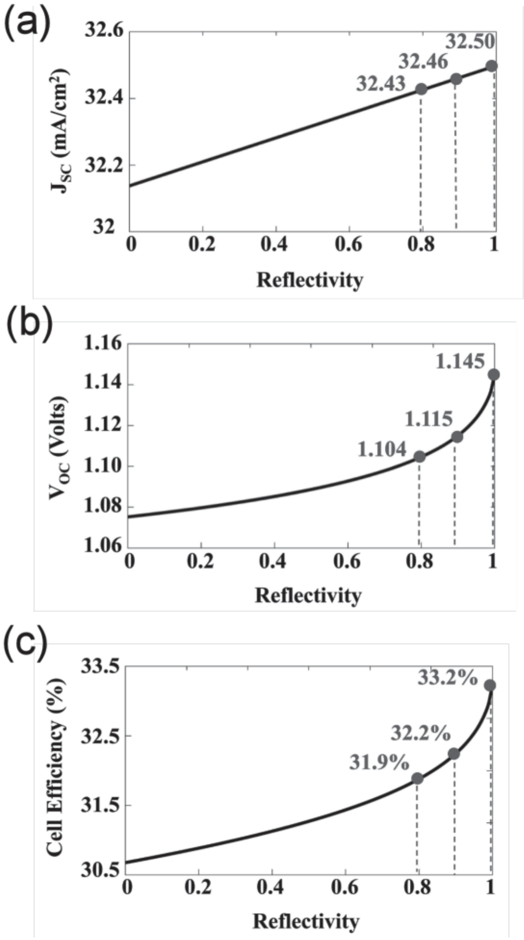

**Figure 16.** The performance of a 3 μm thick GaAs solar cell as a function of reflectivity of the back reflector [49]. (a) $J_{sc}$, (b) $V_{oc}$, and (c) conversion efficiency enhancements as the reflectivity of the back reflector is increased.

For use in connection with InAs/GaAs QDSC and dilute nitride MJSCs, back reflectors based on Ag, Au, and Cu, provide almost ideal reflectivity at the wavelengths longer than 800 nm [107]. By substituting highly reflective and inert Au, which is known to be rather expensive material, with other highly conductive metals would be an attractive alternative to lower the fabrication costs. Ag back reflectors have been demonstrated in GaAs solar cell and GaInP solar cells [85, 108], but Cu is known to diffuse into III–V semiconductors, thus reducing the $V_{oc}$ of the solar cell [81, 109, 110]. This could be avoided by using a double-layer Ag/Cu reflector. Thus, a first development step was fabrication and characterization of Ag/Cu reflectors with different thicknesses of Ag (10 nm, 30 nm, and 50 nm) using double-side polished semi-insulating (SI) GaAs samples [P1]. As a reference, samples with conventional contact metals Ti/Au (50 nm/100 nm) for *p*-GaAs, with Au reflector (100 nm), and with Cu reflector (100 nm) were fabricated. The purpose of Ag is to provide high reflectance and to act as a diffusion barrier for Cu. The Cu layer acts as a part of the reflector, as a current spreader, and as a conductor. In addition, Ni/Au layers (10 nm/50 nm) were fabricated on top of the reflector where Au acts as a protective layer and Ni is required between Au and Cu as an adhesion metal. As a verification of the proper adhesion of the reflector structures, a Scotch peel test was conducted, revealing no peeling of the metals occurred, conforming the applicability of these reflectors.

The optical properties of the fabricated reflectors were characterized using a PerkinElmer Lambda 1050 spectrophotometer. The specular reflectance at 8° angle of incident light was measured. The results are presented in Figure 17, which shows that the reflectance between the 10 nm, 30 nm, and 50 nm Ag/Cu reflectors is identical, meaning that the 10 nm layer of Ag is already enough to maintain the high reflectivity of over 90% average reflectance in the wavelength range of 0.9–1.4 μm. The decreasing reflectance near 0.9 μm, close to GaAs band edge, is caused by the absorption of SI-GaAs. In addition, the free carrier absorption can be seen at the longer wavelengths lowering the reflectance. In comparison, the conventional Ti/Au metal contact showed less than 40% average reflectance in the wavelength range of 0.9–1.4 μm. The implementation of these Ag/Cu reflectors in dilute nitride solar cells is described in section 4.1.1.

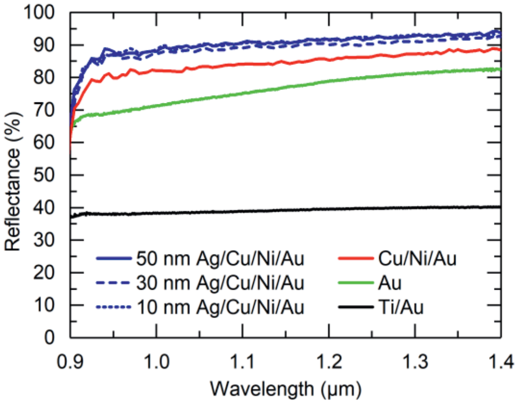

**Figure 17.** Reflectance results of the Ag/Cu back reflectors in SI-GaAs samples. In comparison, the reflectance of conventional Ti/Au metallization. The data is adopted from [P1].

To further enhance the effect of the planar back reflector in GaAs solar cells, a texturing of the contact GaAs has been proposed [111]. This way, the absorption of the contact GaAs is not decreasing the amount of the light travelling back to the active area of the GaAs solar cell after being reflected from the planar back reflector. However, in QDSCs or dilute nitride solar cells, which are harvesting a longer wavelength range, the absorption to contact GaAs in not diminishing the effect of the back reflector.

Since Cu is known to diffuse into III–V semiconductor, the diffusion of Ag/Cu reflectors into the semiconductor was characterized in [P1] by scanning the cross-section of the metal-semiconductor interface with a focused ion beam scanning electron microscope (Zeiss Crossbeam 540 FIB-SEM), equipped with an energy-dispersive x-ray spectroscopy detector (EDS) from Oxford Instruments. Samples with similar metals were studied as in section 3.1. In addition, the samples were annealed at 200 °C and 420 °C for 90 s to evaluate the effect of the fabrication conditions on the diffusion of the metal reflector into GaAs. SEM images and EDS data of the cross-section of the metal-semiconductor interface are presented in Figure 18 and Figure 19, respectively.

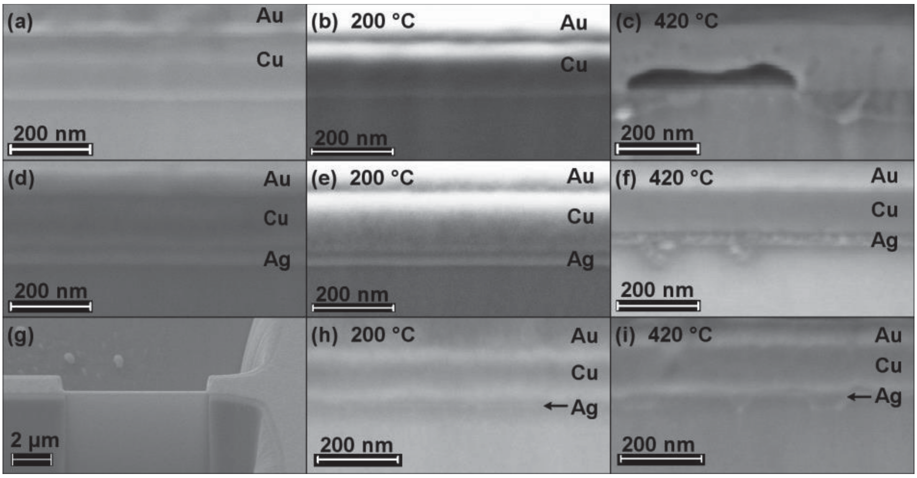

**Figure 18.** SEM images of the Ag/Cu reflectors. (a), (b), and (c) Cu reflector with different annealing temperatures, (d), (e), and (f) 50 nm Ag/Cu reflector with different annealing temperatures, (g) large scale SEM image of the FIB-processed sample slice to clarify the measurement configuration, (h) and (i) 10 nm Ag/Cu reflector with different annealing temperatures [P1].

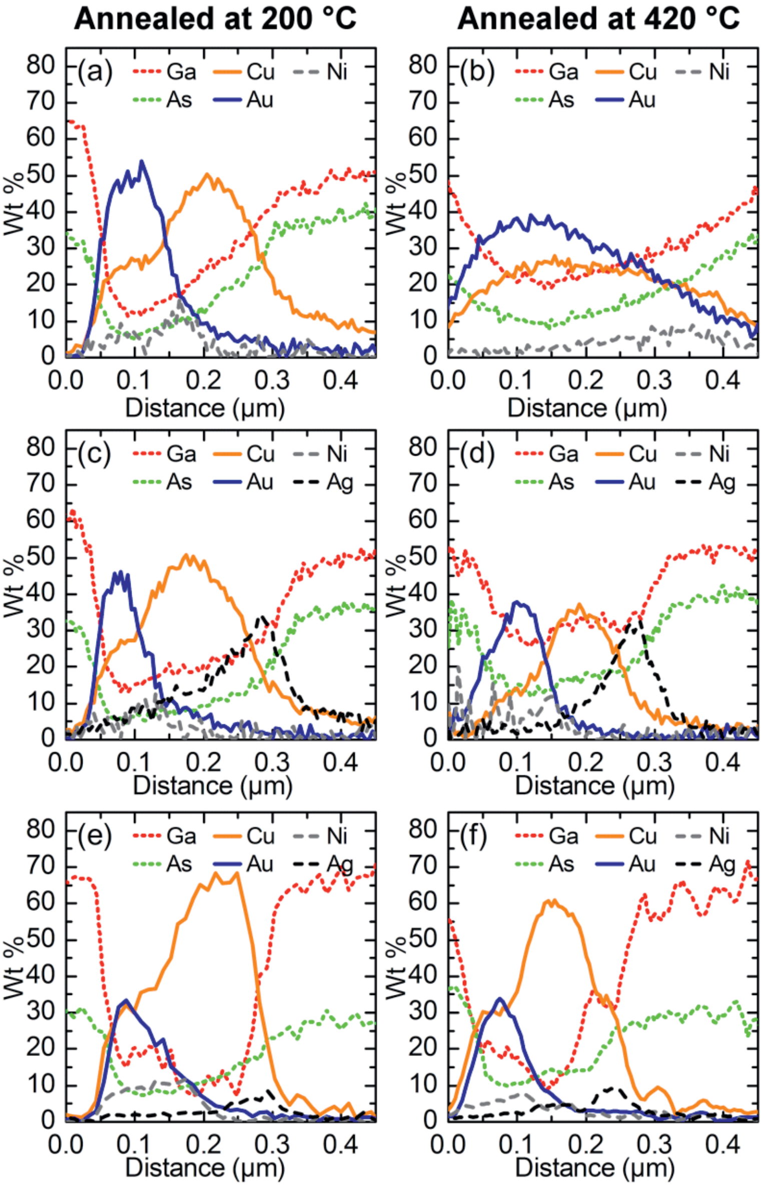

**Figure 19.** FIB-EDS results from the cross-section of back reflector metals: (a) and (b) Cu reflector, (c) and (d) 50 nm Ag/Cu reflector, (e) and (f) 10 nm Ag/Cu reflector. The x-axis starts from the surface of the sample. The artifact signals of Ga and As at the surface originates from the electrons hitting the GaAs behind the sample slice made by FIB scanning. The Ga signal is overemphasized due to Ga bombardment during FIB. During the measurement the samples were tilted, which causes some inaccuracy in regard to the distance [P1].

The SEM images and EDS data reveal that Cu, Ni, and Au layers remained separated in the unannealed Cu sample and in Cu sample with the 200 °C annealing temperature. However, the Cu-semiconductor interface is slightly blurred in the SEM image of the sample annealed at 200 °C, indicating that already gradual mixing occurs, which is also seen in the Cu reflector annealed at 420 °C. Moreover, the color of the surface of the Cu sample annealed at 420 °C changed, which is ascribed to an alloy formation between Au and Cu [112]. In addition, in the EDS data for Cu sample annealed at 420 °C, Au and Cu peaks are overlapping, and the signals finally attenuate in the GaAs layer revealing Cu diffusion into GaAs. Therefore, according to the results, Cu as such is not suitable for back reflectors.

In Figure 18, the SEM images of the Ag/Cu samples and the samples annealed at 200 °C showed that the metal layers remained separated and no diffusion occurred even after being annealed at 200 °C, which was also observed in the EDS data. Even though the Ag/Cu samples annealed at 420 °C did not show any mixing of Ag and GaAs in the EDS data, the SEM images reveal that after annealing at 420 °C, the metal layers are still separated but triangular spikes of Ag have formed into GaAs. The same effect was observed for both the 10 nm and 50 nm Ag/Cu samples. Consequently, 10 nm of Ag acts sufficiently as a diffusion barrier for Cu, although the fabrication temperatures should not exceed 200 °C.

Besides the need for ensuring high reflectivity, the primary function of the back reflector is to ensure a good ohmic contact. The back contacts are conventionally fabricated by alloying the metals using thermal annealing, resulting in low resistivity, while the high reflectance of the metal is reduced due to the reduction of the interface sharpness when compared to non-alloyed metals [113]. Although non-alloyed contacts usually possess higher contact resistivity than the alloyed ones [114], by using highly doped *p*-GaAs as a contact layer, lower contact resistivity can be achieved [81].

The contact resistivity of the Ag/Cu reflectors was measured in [P1] using the Transmission Line Method (TLM) [115]. The fabrication of the contact pads for TLM samples included photolithographic processing onto MBE grown *p*-GaAs layers having a doping level of ~$10^{20}$ $cm^{-3}$. Identical metals as for the reflectance samples in section 3.1 were deposited with an electron beam metal evaporator and the mesa structures were etched by inductively coupled plasma using photolithographic patterning. Figure 20 presents a SEM image of the fabricated TLM sample with the contact pad dimensions of 300 µm × 100 µm with the pad distances of 10 µm, 20 µm, 40 µm, 80 µm, and 120 µm.

**Figure 20.** SEM image of the TLM sample where the lighter contact pads with different distances are in the center and darker are in the mesa.

The contact resistivity results, presented in Table 1, showed low resistivity in the order of $10^{-6}$ Ω·cm$^2$ for all reflectors. These are lower than typical contact resistivities which are in the order of $10^{-5}$ Ω·cm$^2$ for non-alloyed contacts [116]. However, some contact resistivities for *p*-GaAs with alloyed metals are in the order of $10^{-7}$ Ω·cm$^2$ [114, 116]. These results point out that an ohmic contact can be formed without annealing owing to the high doping level of the *p*-GaAs contact layer while preserving the high reflectivity of the metal reflector, although as low-level resistivity as alloyed contacts exhibit was not reached.

**Table 1.** Contact resistivity results from TLM measurements for planar back reflectors. The data is adopted from [P1].

| Back reflector | Ti/Au | Au | Cu | 10 nm Ag/Cu | 30 nm Ag/Cu | 50 nm Ag/Cu |
|---|---|---|---|---|---|---|
| Contact resistivity (Ω·cm$^2$) | $3\times10^{-6}$ | $1\times10^{-6}$ | $4\times10^{-6}$ | $4\times10^{-6}$ | $4\times10^{-6}$ | $5\times10^{-6}$ |

## 3.2 Structured back reflectors

A structured back reflector reflects the light in multiple angles, which would further increase the absorption length in the active layers of the solar cell compared to planar back reflectors. The structuring involves formation of a grating for light diffraction using different approaches [96, 117-119]. As a remark, nanostructured back reflectors in use with a GaAs solar cell with a only 204 nm thick absorber layer exhibited major improvement in $J_{sc}$ when compared to the similar cell without a reflector [120].

Diffractive gratings fabricated directly into the semiconductor, i.e., into the back surface field (BSF) of the solar cell, may increase parasitic losses due to the large structured interface between the semiconductor and the metal, introducing a surface plasmon effect [96]. However, these parasitic losses can be alleviated by employing an interlayer between the semiconductor and the metal [121]. Thus, a design where the diffractive gratings were fabricated into a polymer was devised [P2]. The applied polymers are inert and commonly used in electronic industry. Photolithography and nanoimprint lithography (NIL) were employed as fabrication methods for the polymer structures.

Back grating structures were simulated in order to find optimum dimensions of the gratings for absorption near the GaAs absorption edge [118, 122]. In particular, the gratings are designed for enhancing interband transitions of typical InAs/GaAs QDSCs in the wavelength range of 0.9–1.2 µm [21, 123]. In addition, a MJSC with a dilute nitride junction, which operates at the same wavelength range as the QDSC, would benefit from identical diffraction gratings [124]. According to numerical simulations, presented in Figure 21, the maximum photocurrent is achieved when the aspect ratio, i.e., the ratio of height/period of the gratings, is within the range of 0.32–0.38.

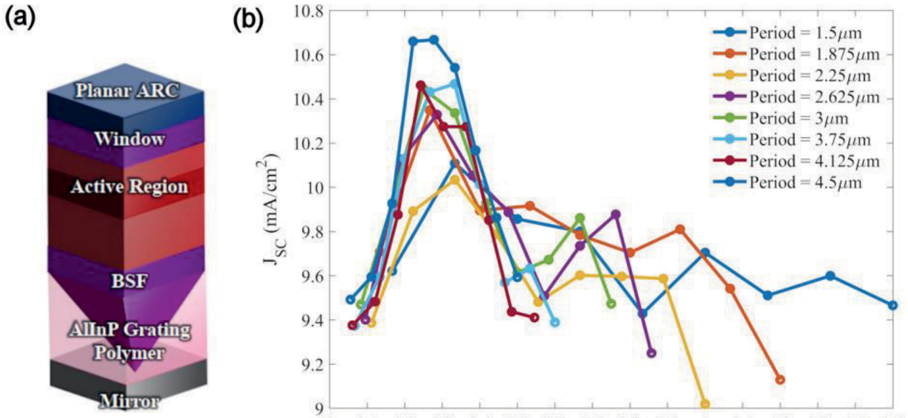

**Figure 21.** (a) A schematic drawing of the back grating configuration in a QDSC. (b) The simulated $J_{sc}$ of the QDSC at the wavelength range of 0.75–1.2 µm as a function of the aspect ratio (height/period) [75, 118].

Three diffraction grating structures were fabricated together with a planar reference sample for assessing diffraction efficiencies and their dependence on the design features. To study the diffraction properties of the gratings, double-side polished SI-GaAs was used as a substrate having a thickness of 350 µm since it is almost transparent for wavelengths of over 900 nm. Thus, the comparison of the gratings using reflectance measurements is possible. Single-layer $SiN_x$ ARCs were deposited on the both sides of the substrate by plasma enhanced chemical vapor deposition (PECVD). The ARCs were optimized to minimize the reflectance both at the air/GaAs interface and the GaAs/polymer interface on the front and on the backside of the solar cell, respectively. The properties of the $SiN_x$ layers were tuned by varying the process parameters such as deposition time and $NH_3$ and $SiH_4$ gas flows. The characteristics of the ARCs are presented in Figure 22, where n is the refractive index. In addition, Figure 22 introduces the three back gratings, which are described in more detail in the following sections.

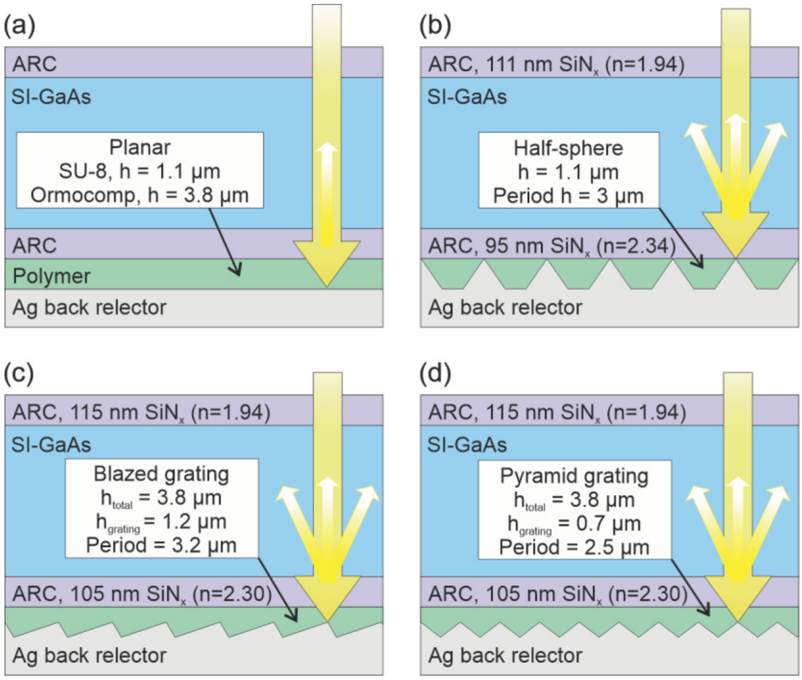

**Figure 22.** A schematic drawing of the back reflector structures. (a) Planar reflector, (b) half-sphere grating, (c) blazed grating, and (d) pyramid grating. Adopted from [P1].

### 3.2.1 Reflector with half-sphere grating

Half-sphere gratings were fabricated into a commercial epoxy based negative photoresist SU-8 (MicroChem Corp.) which is chemically and mechanically stable and has low absorbance in the wavelength range of 0.4–1.6 μm [125]. Prior to the photolithography process, a photolithography mask with square openings of size 2 μm × 2 μm and with the period of 3 μm was fabricated with a Heidelberg μPG 501 direct-writing system. In the photolithography process, the shape of the pattern can be tuned by changing the process parameters. For example, the cylinder grating was achieved as presented in Figure 23, with the process parameters used in the beginning of the development process.

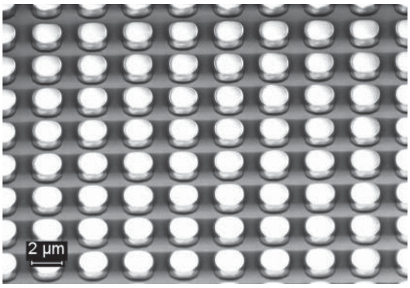

**Figure 23.** SEM image of the cylinder grating fabricated into SU-8 polymer.

To obtain the desired half-sphere structure, the exposure time was increased from 8 s (exposure dose of 72 mJ/cm$^2$) to 11 s (exposure dose of 99 mJ/cm$^2$) with EVG 620 mask aligner and the post exposure bake temperature was increased from 95 °C to 105 °C. The obtained half-spheres have the height of 1.1 μm and the period of 3 μm. Figure 24 shows SEM and optical profilometer images of the half-sphere grating, in which the top of the half-sphere appears slightly flattened and the half-spheres are connected by a bridge to each other. To finalize the reflectors, 200 nm Ag was deposited on top of the polymer layer using an electron beam evaporator.

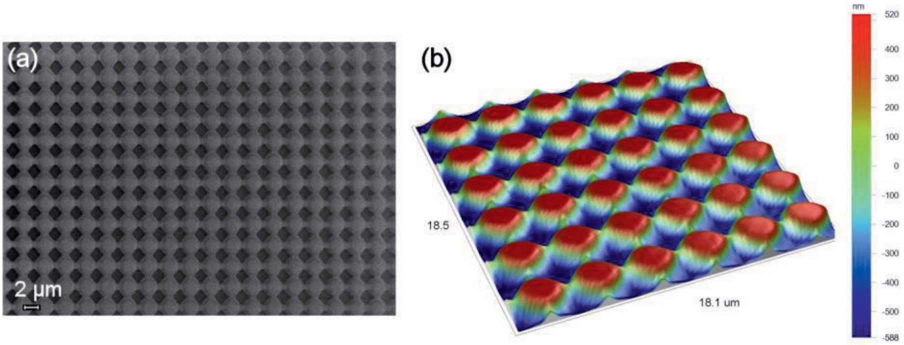

**Figure 24.** (a) SEM and (b) optical profilometer images of the half-sphere grating. The half-spheres are connected by a bridge.

The reflectance results of the half-sphere and cylinder gratings are presented in Figure 25, where the difference between the total and the specular reflectance represents the diffuse reflectance. The absorption of SI-GaAs is observed in the wavelengths below 900 nm, as expected.

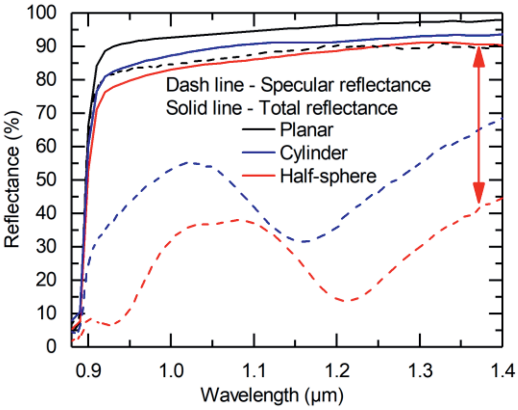

**Figure 25.** Measured reflectance of the half-sphere grating and cylinder grating reflectors. The red double-headed arrow represents the quantity of the diffuse light. The data is adopted from [P2].

In Figure 25, the half-sphere grating exhibits higher diffuse reflectance when compared to the cylinder grating. Here, the diffuse reflectance is a desired effect for diffraction gratings since it will increase the length, which the light is travelling inside the absorbing layers of the solar cell. However, in both gratings a local maximum in the specular reflectance is observed at the target wavelength range of 0.9–1.2 µm, decreasing the diffuse reflectance. As a reference, the planar reflector showed high total reflectance and ~10 percentage points lower specular reflectance, presumably due to the diffuse reflectance, which may occur also at planar surfaces due to optical scattering [126].

To quantify the amount of diffracted light, diffraction efficiency was measured with an in-house built variable angle measurement system and 2D-simulated for the reflector with the half-sphere grating as described in [P2]. The diffraction orders of m = 0, m = ±1, and m = ±2 were measured. As a result, a good correlation between the measurements and the simulations were observed as presented in Figure 26. The diffraction orders are symmetric along the xz-plane, which was observed at the m=±1 and m=±2 diffraction orders [P2]. Considerable power coupling to the first two diffraction orders is discovered. Moreover, the measured diffraction efficiency of the zero order is in line with the specular reflectance results for half-sphere grating presented in Figure 25, which proves the reliability of the results.

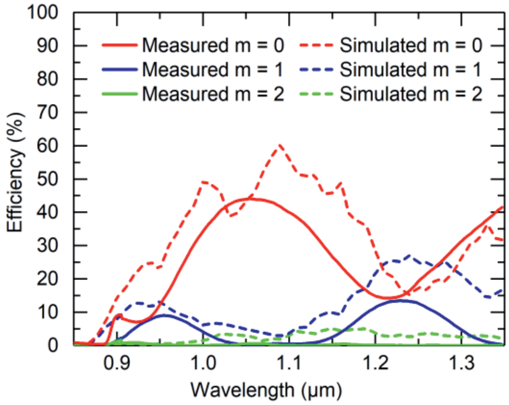

**Figure 26.** Measured and simulated diffraction efficiency results of the reflector with the half-sphere grating. The data is adopted from [P2].

### 3.2.2 Reflector with blazed grating

To enhance the quantity of the diffuse light, i.e., to diminish the local maximum observed in the specular reflectance spectra of the half-sphere grating (Figure 25), a reflector with a blazed grating was devised. The sample design is presented in Figure 22. In the fabrication process, a NIL master with blazed grating (Thorlabs) was transferred into a polydimethylsiloxane (PDMS) stamp. The blazed grating of the stamp was imprinted to a commercial OrmoComp NIL photoresist (Micro Resist Technology GmbH) [127] by a NIL process using EVG mask aligner. In addition, on top of the polymer layer, 200 nm Ag layer was deposited using electron beam evaporator to complete the reflector. The fabricated blazed grating structure has the height of 1.2 μm and the period of 3.2 μm. A microscopy image and a cross-sectional SEM image of the blazed grating are presented in Figure 27.

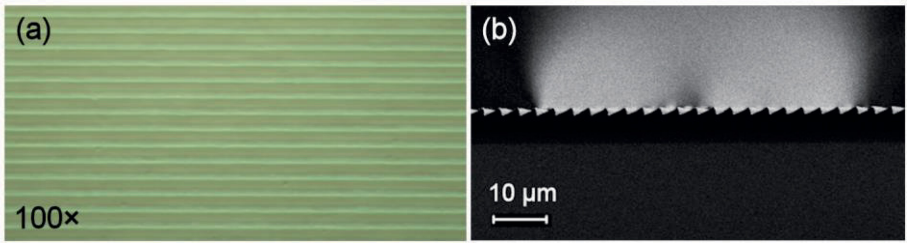

**Figure 27.** (a) Microscopy image with 100× magnification from the top of the blazed grating and (b) the cross-sectional SEM image of the blazed grating.

The reflectance spectra of the reflector with blazed grating and the reference sample with planar reflector are presented in Figure 28, which also presents the simulation results. According to the results, the local maximum seen in the half-sphere grating results is no longer present, increasing the portion of the diffuse light in the wavelength range of 0.9–1.2 μm. In addition, the blazed grating showed higher diffuse reflectance when compared to the half-sphere structure. However, the total reflectance of the blazed grating was lower compared to the half-sphere grating, revealing some extra losses in the structure, presumably originating from surface plasmon resonance (SPR) appearing in the metal reflector [128]. This behavior was also seen in the simulated total reflectance, which was 10 percentage points lower than the measured reflectance, since the simulations are most probably overestimating the losses in the reflector. Moreover, the lower losses in the fabricated structure could be attributed to the reduction of SPR effect due to the flattening of the grating pattern when compared to the simulated grating. A more detailed analysis can be found in [P2].

To assign the limits of the diffuse light, the front surface reflectance of the samples was simulated and is presented in Figure 28. The single-layer $SiN_x$ ARC was designed to have the lowest reflectance at the wavelength of 0.9 μm, meaning that part of the light is reflected from the surface of the sample without reaching the back reflector, thus increasing the specular reflectance.

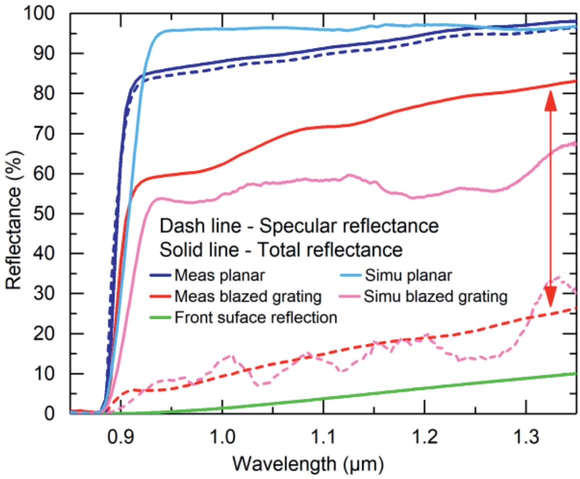

**Figure 28.** Measured and simulated reflectance of the reflector with blazed grating. In addition, the front surface reflectance was simulated. The red double-headed arrow represents the diffuse reflectance. The simulated total and specular reflectance of the planar reflector are identical. The data is adopted from [P2].

As an observation, the simulated total reflectance is almost horizontal for the planar reflector, whereas the measured reflectance is increasing towards higher wavelengths as seen in Figure 28. This difference could be mostly due to the residual absorption of light into SI-GaAs. The transmittance measurements across the SI-GaAs wafer revealed an extinction coefficient $k \sim 6\times10^{-6}$, whereas the adopted GaAs optical model [129] used in the simulations had $k = 1\times10^{-6}$ in the wavelengths above 890 nm.

The diffraction efficiency results of the reflector with blazed grating are presented in Figure 29. The diffraction orders of $m = 0$, $+1$, and $+2$ in the 2D-simulations are supporting the measurements, even though they are not perfectly matching. In the simulations, low frequency oscillations were predicted for the $m = 0$ spectrum, which were not observed in the measured spectrum. Such oscillations could be attributed to the onset of a Fabry-Perot cavity effect in the polymer layer [130]. However, such interference effects are not apparent in the experimental results due to the non-uniformity of the fabricated gratings. In addition, at $m = 0$, the corresponding specular reflectance shown in Figure 28 is compatible with the diffraction efficiency measurement. Since the blazed grating is asymmetric, the diffraction orders are not symmetric along the xz-plane which is observed at $m = \pm1$ and $m = \pm2$ diffraction orders [P2].

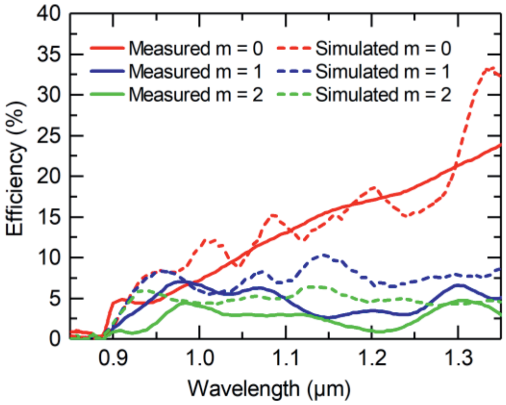

**Figure 29.** Measured and simulated diffraction efficiency results of the reflector with blazed grating. The data is adopted from [P2].

### 3.2.3 Reflector with pyramid grating

The reflector with pyramid grating was designed to further increase the diffraction. In the experimental process, an in-house fabricated NIL master with the pyramid grating was used. The master was patterned by electron beam lithography and the pyramid grating was created by etching Si by anisotropic wet etching. To obtain the required dimensions of the pyramids, i.e., the height and the aspect ratio (Figure 21), the pyramid grating was transferred into a PDMS stamp, which was then imprinted onto NIL photoresist. Subsequent to the NIL, the pattern was dry etched with a desired selectivity by reactive ion etching into another Si wafer, realizing the final NIL master with pyramid grating, which is presented in Figure 30. As seen from the SEM image, the peak of the pyramid is slightly flatted.

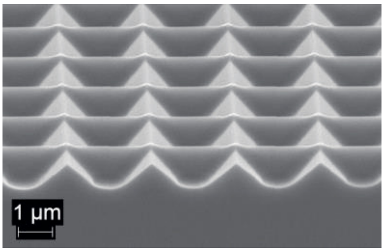

**Figure 30.** SEM image of the fabricated NIL master with pyramid grating. The material of the master is Si.

The NIL processes for fabricating the reflector with pyramid grating (sample design is presented in Figure 22) included transferring the pyramid gratings from the masters into PDMS stamps, which were used for imprinting the gratings into the OrmoComp NIL photoresist. The fabricated pyramid grating has the height of 700 nm and the period of 2.5 µm. To finalize the reflector, a 200 nm Ag layer was deposited on top of the polymer grating using electron beam evaporator. Figure 31 shows an optical microscopy image, an atomic force microscopy (AFM) image, and a SEM image of the pyramid grating. In addition, a photograph of the sample surface is presented in Figure 31 to illustrate the diffraction behavior when the light is reflected from the sample. The fabricated pyramids show flattened peaks, which was already observed in the Si master, meaning the transfer of the pattern was successful and the flattening is originating from the Si master.

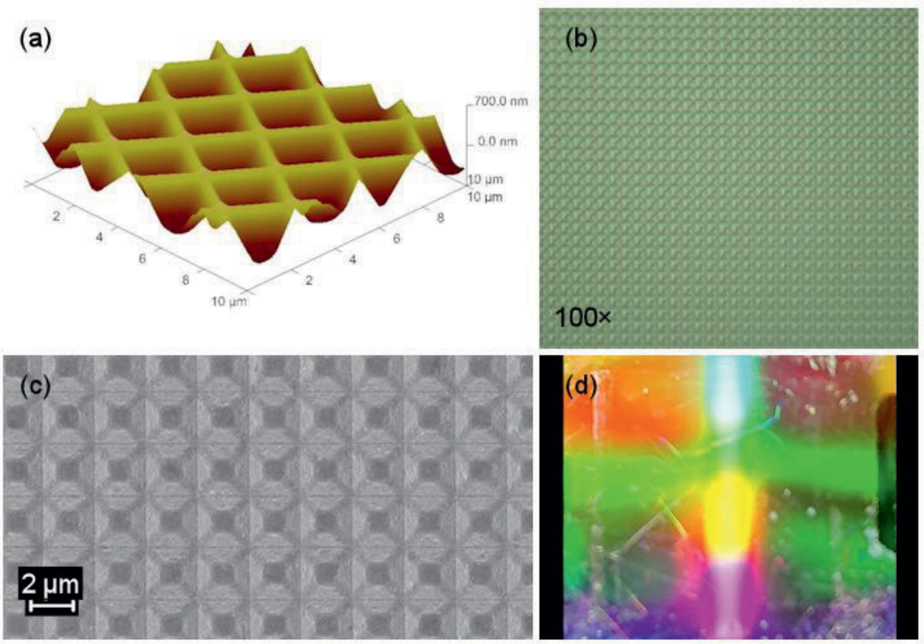

**Figure 31.** (a) AFM image (b) optical microscopy image, (c) SEM image, and (d) photograph of the pyramid grating sample with the sample size of being 15 mm × 15 mm.

The reflectance results of the pyramid grating are presented in Figure 32, which also shows blazed grating results as a comparison. In addition, the simulated reflectance spectrum of the pyramid grating is presented.

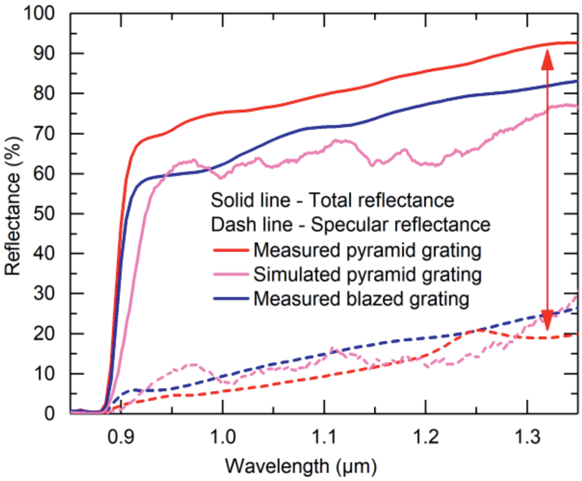

**Figure 32.** Measured and simulated reflectance of the reflector with pyramid grating. The red double-headed arrow represents the fragment of the diffuse light. The data is adopted from [P2].

According to these results, the pyramid grating shows the highest diffuse reflectance when compared to the blazed grating and the half-sphere structure. The total reflectance of the pyramid grating was higher when compared to the blazed grating, indicating lower losses in the reflector. As noticed also in the blazed grating results, the simulated total reflectance for the pyramid grating is approximately 10 percentage points lower than the measured total reflectance. This occurs possibly due to fact that the simulations are overestimating the losses in the structured reflector while the measurements have lower losses due to flattening of the pyramid structures reducing the SPR effect. Despite this, an overall good agreement between the measured and the simulated trends is achieved, supporting the conclusions of the diffractive properties of the pyramid grating.

The diffraction efficiency results of the pyramid grating are presented in Figure 33, revealing power coupling to the first diffraction order. The second diffraction order was not observed in the results, since the measurement setup was performing measurements up to 48° angle, where $m = 2$ is not yet detectable. However, according to the simulations, there is power coupling also to the second diffraction order. The diffraction orders $m = \pm1$ were observed to be identical since the pyramid grating is symmetrical. Furthermore, the $m=0$ diffraction order is well in line with the specular reflectance results, presented in Figure 32.

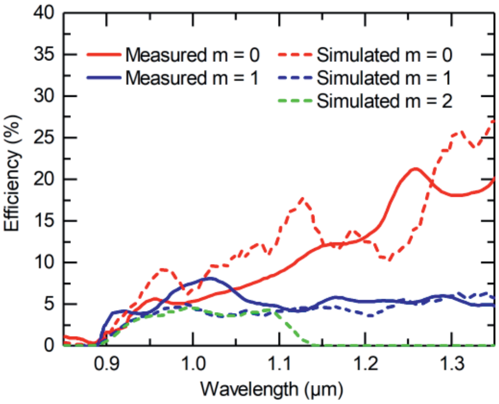

**Figure 33.** Measured and simulated diffraction efficiency results of the reflector with the pyramid grating. The data is adopted from [P2].

## 3.3 Electron irradiation of the pyramid grating structures

Terrestrial III–V solar cells have traditionally exhibited long lifetimes which are in the range of 20 to 30 years and even longer [131]. However, solar cells that are used in space confront harsh environments and are exposed to high-energy particle bombardment, which affects their lifetime. The irradiation dose that solar cells face during their lifetime in space depends on the type of the mission. For example, geostationary orbit missions usually continue for 15 years and the damage created by the electron irradiation equals a dose of $1\times10^{15}$ 1-MeV electrons/cm$^2$, whereas for low earth orbit missions lasting for ~10 years, the equivalent doses are 5 to 10 times lower [132]. Thus, since flexible thin-film solar cells are potentially of high interest for space applications, a study was performed to assess the functionality of the back grating structures fabricated into a polymer after subjecting them to electron irradiation.

The electron irradiation was performed on the samples with the OrmoComp polymer at an energy of 1-MeV and an electron flux of $5\times10^{11}$ e$^-$/cm$^2$/s using a Van der Graaf accelerator at the Reactor Institute Delft of the Delft University of Technology. The desired irradiance of the samples was achieved by changing the exposure time, leading to three different total electron doses of $1\times10^{14}$ e$^-$/cm$^2$, $3\times10^{14}$ e$^-$/cm$^2$, and $1\times10^{15}$ e$^-$/cm$^2$, with the highest being considered as the end of life conditions.

The total and specular reflectance spectra were measured after the electron irradiation for the reflectors with pyramid grating having identical structure to those presented in Figure 22. The reflectance results are presented in Figure 34 together with the results of the reflector without the electron irradiation dose used as a reference [P3]. The total reflectance spectra of the irradiated samples were identical up to the highest dose when compared to the sample without irradiation. In addition, the specular reflectance spectra of the irradiated samples are similar to the reference, except for the sample with the dose of $1\times10^{14}$ $e^{-}/cm^{2}$ which has slightly lower specular reflectance. This is incoherent since it has the lowest irradiation dose. The lower specular reflectance could originate from the inaccuracy in the reflectance measurement or variations in the fabrication but most likely is not caused by the electron irradiation.

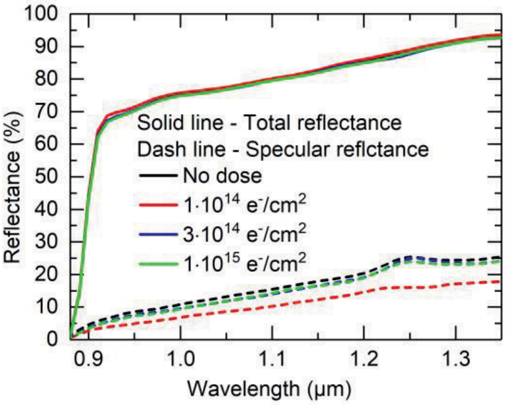

**Figure 34.** Total and specular reflectance results of the reflectors with pyramid grating after the electron irradiation. The data is adopted from [P3].

To characterize the transmittance of the polymer, a set of fused silica glass samples with planar polymer layer deposited on top of the glass was fabricated. The transmittance results are presented in Figure 35, where the black line represents the glass substrate, which has an average transmittance of approximately 93%, being the baseline for the polymer samples.

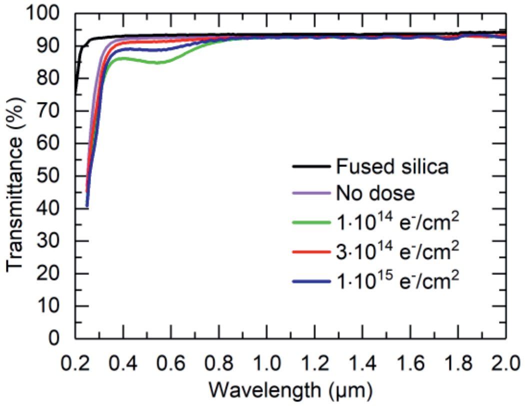

**Figure 35.** Transmittance results of the electron irradiated samples. The data is adopted from [P3].

The transmittance results are identical for all the samples in the wavelength range of 0.9–2.0 μm. However, in the wavelength range of 0.3–0.9 μm, the effect of the electron irradiation is visible. For example, the sample with the lowest dose of $1\times10^{14}$ $e^{-}/cm^{2}$ exhibits the lowest transmittance. Since a clear trend is not apparent in the results, it is challenging to make any solid conclusion. Nevertheless, the transmittance of the polymer is not affected by the electron irradiation in the QD and dilute nitride solar cells wavelength range of 0.9–1.2 μm.

In the mechanical study, the adhesion of the polymer was defined by the Scotch peel test. The sample structures were identical to the reflectors with planar polymer in Figure 22. No notable pealing was observed in any of the samples. However, since the sample with the highest irradiation dose was destroyed during the detachment of the sample from the temporary carrier, the adhesion of the highest dose remains undefined. Despite this, OrmoComp polymer could most probably be used as a part of a back reflector in space solar cells.

To study the swelling of the polymer during electron irradiation, samples with a textured polymer layer on $SiN_x$-coated GaAs substrate were fabricated. The dimensions of the features were measured by optical microscopy before and after the electron irradiation, and remained unchanged, indicating that the polymer was not affected by electron irradiation.

In conclusion, based on the characterization results of the electron irradiation, the reflectors with pyramid grating fabricated into OrmoComp polymer are suitable for space environment when applied for QDSCs or dilute nitride solar cells. Furthermore, the tolerance against electron radiation has been demonstrated to be higher with InAs/GaAs QDSCs than with single junction GaAs solar cell [133].

Also, the dilute nitride solar cell showed enhanced electron irradiation tolerance when compared to a GaAs solar cell [134], which gives a good background to fabricate these type of advanced solar cells using back reflectors with pyramid gratings for space applications.

# 4 III–V SOLAR CELLS WITH BACK REFLECTOR

This chapter describes the fabrication processes and analyses the results of the planar and the structured back reflectors applied to the dilute nitride solar cells and to the InAs/GaAs QDSCs. The first section concentrates on two generations of dilute nitride solar cells with the $E_g$ of 1 eV [P1] and 0.8 eV [P5]. In these experiments, the *n*-GaAs substrate is thinned and polished and the measurements are conducted through an n-GaAs absorber. Nevertheless, the analysis of the EQE and current-voltage (*IV*) characteristics of the solar cells is valid due to the different wavelength range dilute nitrides are absorbing when compared to GaAs. The second section focuses on the InAs/GaAs QDSCs with planar back reflector, in which the solar cells are in thin-film configuration where the substrate is removed, and the thin-film is bonded to the carrier. The total thickness of the solar cells is only a few micrometers. In the final section the use of back reflectors with pyramid grating applied to QDSCs is assessed by simulations, in which the analysis is conducted with realistic experimental parametrization.

## 4.1 Thin-film dilute nitride solar cells with planar back reflector

The use of back reflectors in MJSCs with dilute nitride bottom junction would enable achievement of current matching conditions in those cases that the thickness of the dilute nitride absorbing layer is limited by the defects associated with N incorporation. To this end, the effect of the back reflectors to dilute nitride solar cells fabricated by MBE was assessed. The dilute nitride solar cells have bandgaps similar to those used in recent demonstration of four junction solar cells [54]. The first type of dilute nitride single junction solar cell had $E_g$ of ~1 eV and was used to assess the effect of different planar back reflectors [P1]. The goal was to reveal the optimal reflector approach. In the second phase of the study, three single junction dilute nitride solar cells with different thicknesses (350 nm, and 700 nm) and $E_g$ values (0.8 eV, and 0.78 eV) were fabricated [P5]. In these solar cells, an optimized planar Au back reflector was used and the main goal was to assess the limits of using narrow bandgap dilute nitride material in MJSCs.

### 4.1.1 Performance of 1 eV solar cells with back reflector

Single junction GaInNAs solar cells were grown inverted on highly doped *n*-GaAs substrate. The growth process of the semiconductor layers is reported in [69]. The final devices were fabricated with the same planar back reflectors which are presented in section 3.1. The metal reflectors were deposited using an electron beam evaporator. In addition, indium contacts were deposited on top of the polished substrate, which is the front side of the solar cell. Finally, the front surface of the solar cell was coated with a double-layer $TiO_2/SiO_2$ ARC by electron beam evaporator. A generic sample structure is presented in Figure 36.

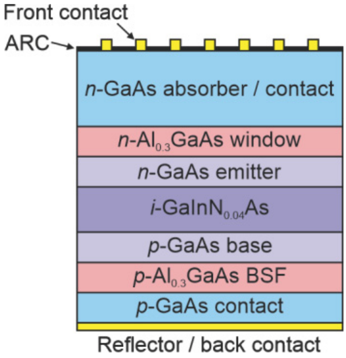

**Figure 36.** A Schematic drawing of the 1 eV dilute nitride solar cells with planar back reflector.

EQE measurements were performed with a setup equipped with a 250 W quartz tungsten halogen lamp and a Digikrom DK240 monochromator equipped with an 800 nm long-pass filter. The signal were measured using an SRS SR830 lock-in amplifier and chopped light. A NIST-calibrated Ge reference detector was used as a reference. Figure 37 presents the EQE results of the 1 eV dilute nitride solar cells with the planar back reflectors.

The EQE results show drastic improvement for solar cells with the Ag/Cu and Cu back reflectors when compared to the benchmark Ti/Au metallization. This is a consequence of higher reflectance of the back reflector as seen in Figure 17, which correlates well with the EQE results. The highest enhancement in EQE is observed close to the band edge of GaInNAs, where the absorption coefficient decreases, while the transmission increases. As in the reflectance results, the difference between the 10 nm, 30 nm, and 50 nm Ag/Cu reflectors is small also in the EQE results, revealing that already 10 nm layer of Ag is working well as a reflector. In addition, after the 10 nm Ag/Cu sample was thermally annealed at 200 °C for 90 s, the high

EQE was maintained, revealing a successful behavior of Ag as a diffusion barrier for Cu. This confirms permitting the processing conditions of 200 °C without affecting the performance of the solar cell with back reflector as concluded in section 3.1.

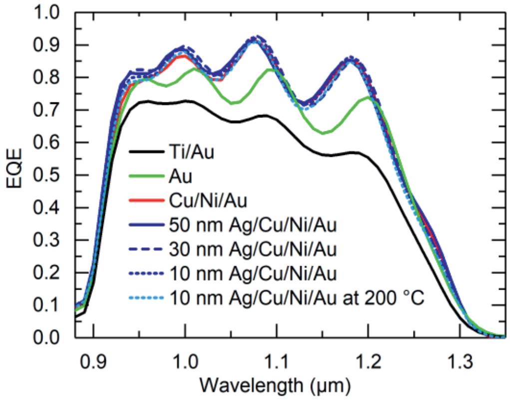

**Figure 37.** EQE results of the 1 eV single junction dilute nitride solar cells with planar back reflector. The data is adopted from [P1].

The $J_{sc}$ values were estimated by integrating the EQE results over the AM1.5D (1000 W/m$^2$) spectrum [51], while assuming a thick GaAs absorber on top of the solar cells. The calculated $J_{sc}$ results are collected in Table 2. The $J_{sc}$ of the solar cells with the Ag/Cu reflectors was about 14 mA/cm$^2$, being 31% higher when compared to the reference solar cell with Ti/Au reflector. The obtained $J_{sc}$ value meets the current matching condition of GaInP/GaAs top junctions used in triple-junction MJSCs [19].

**Table 2.** Calculated $J_{sc}$ values from the EQE results at AM1.5D (1000 W/m2) spectral conditions for the dilute nitride solar cells with planar back reflectors.

| Back reflector | Ti/Au | Au | Cu | 10 nm Ag/Cu | 10 nm Ag/Cu at 200 °C | 30 nm Ag/Cu | 50 nm Ag/Cu |
|---|---|---|---|---|---|---|---|
| $J_{sc}$ integrated from EQE (mA/cm$^2$) | 10.7 | 12.4 | 13.4 | 13.6 | 13.4 | 13.7 | 13.7 |

By using the Ag/Cu reflector with an optimized GaInP/GaAs/GaInNAs triple-junction solar cell, a conversion efficiency of 45% could be achieved at AM1.5D spectrum under 1000× concentration. This is 10 percentage points higher when compared to the identical triple-junction solar cell with conventional Ti/Au back metallization, which would reach the conversion efficiency of only 35% [P1].

### 4.1.2 Performance of 0.8 eV solar cells with back reflector

A detailed description of the MBE growth and characterization of the narrow bandgap dilute nitride materials is presented in [55]. For the study with back reflector, an inverted architecture of the solar cells was used when grown on *n*-GaAs substrates, consisting of a 350 nm or 700 nm layer of undoped GaInNAsSb embedded between *p*-GaAs and *n*-GaAs layers. The nitrogen concentration was ~6% corresponding to $E_g$ of ~0.8 eV.

To process the devices, the *n*-GaAs substrates were thinned and polished to the thickness of ~220 µm using a Logitech PM5 precision lapping machine. The remaining substrate operates as a GaAs absorber, i.e., as a filter, replicating a realistic MJSC operating conditions. The front contact metals, Ni/Au/Ge/Au (10 nm/5 nm/30 nm/200 nm), were deposited with an electron beam evaporator. To ensure the ohmic contact, annealing at 420 °C for 90 s was performed. Next, the back reflectors, which also act as back contacts, were evaporated using the Au/Pt/Au (50 nm/50 nm/100 nm) design. After the metallization, and to finalize the solar cells, a four-layer $TiO_2/SiO_2/TiO_2/SiO_2$ (43 nm/20 nm/14 nm/82 nm) ARC was deposited on the front side using ion beam sputtering. A schematic drawing of the fabricated device is presented in Figure 38.

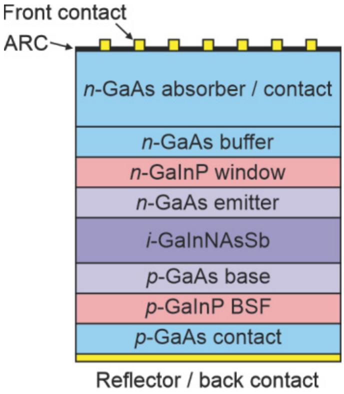

**Figure 38.** A schematic drawing of the fabricated dilute nitride samples with planar back reflector. The n-GaAs absorber has a thickness of ~220 µm.

The highest EQE was measured for the solar cell with the 700 nm thick absorber layer and the lowest bandgap energy of 0.78 eV as presented in Figure 39. The sample with the same thickness but with an $E_g$ of 0.80 eV exhibited slightly lower EQE. In addition, the thinnest sample has the same peak value as the thicker sample with the identical $E_g$ but the carrier collection efficiency is decreased at the longer wavelengths. This difference in EQE performance indicates that the absorption in the 350 µm thick GaInNAsSb layer is insufficient even with the back reflector.

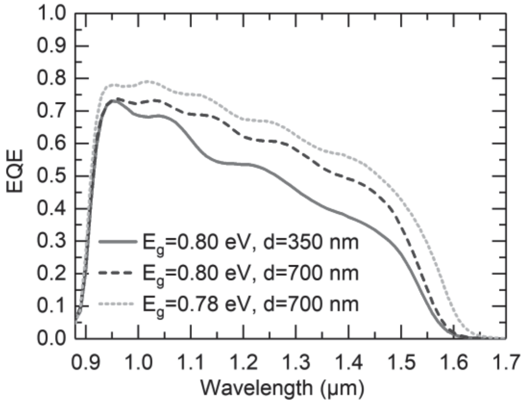

**Figure 39.** The EQE results of the dilute nitride solar cells with Au back reflector. The data is adopted from [P5].

It should be noted that the thick *n*-GaAs absorber on top of the solar cells caused unwanted free-carrier absorption of the incident light. This is the dominant absorption loss mechanism in semiconductors for photons having the energy below the $E_g$ [135]. By using a thinner and a more realistic GaAs filter on top of the dilute nitride solar cell, higher EQE values could be expected.

The *IV* characterization was performed with an OAI TriSol solar simulator at AM1.5D (1000 W/m2) spectral conditions at 25 °C and the measured *IV* curves are presented in Figure 40. The figures of merit from the *IV* measurements and the estimated $J_{sc}$ calculated from the EQE results over the AM1.5D (1000 W/m$^2$) spectrum are presented in Table 3.

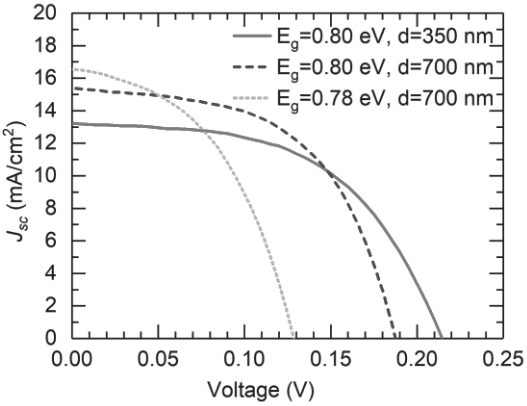

**Figure 40.** *IV* results of the dilute nitride solar cell measured at AM1.5D (1000 W/m$^2$) spectral conditions. The data is adopted from [P5].

**Table 3.** The integrated $J_{sc}$ values from the EQE and the *IV* results for dilute nitride solar cells with planar back reflector at AM1.5D (1000 W/m2) spectrum.

| Sample | $J_{sc}$ integrated from EQE (mA/cm$^2$) | $J_{sc}$ (mA/cm$^2$) | $V_{oc}$ (V) | FF (%) |
|---|---|---|---|---|
| $E_g$=0.80 eV, d=350 nm | 12.4 | 13.2 | 0.22 | 54 |
| $E_g$=0.80 eV, d=700 nm | 14.0 | 15.4 | 0.19 | 66 |
| $E_g$=0.78 eV, d=700 nm | 15.4 | 16.5 | 0.13 | 47 |

The $J_{sc}$ values retrieved from *IV* data are 5–10% higher when compared to values estimated using the EQE results. This is due to the spectral mismatch in the infrared wavelength range of the spectrum delivered by the solar simulator. The highest $V_{oc}$ was observed in the solar cell with the 350 nm thick absorber, which was ~30 mV higher when compared to the sample with the thicker absorber and the same $E_g$. The narrowest bandgap sample exhibited a $V_{oc}$ of over 60 mV lower compared to the other samples, indicating deteriorated material quality. However, the relatively low measured $V_{oc}$ values are comparable to diffused Ge junctions [136]. A more detailed analysis can be found in [P5]. In conclusion, despite the modest $V_{oc}$ of the dilute nitride solar cells, the demonstrated current generation showed great potential, enabling the narrow bandgap dilute nitride solar cells to be used as a bottom junction in MJSCs.

## 4.2 Thin-film QD solar cells with planar back reflector

To characterize the increase in the photocurrent generation of InAs/GaAs QDSCs with back reflector, the QDSC structures were grown inverted by MBE. A so-called shallow junction design was employed with an *n*-GaAs emitter and a *p*-GaAs base [137]. The structure included 10 QD layers with a QD density of approximately $6\times10^{10}$ 1/cm$^2$, separated by ~30 nm thick *i*-GaAs layers. The total thickness of the absorbing layers was 0.75 µm. This is too thin for being optimal for terrestrial operation, yet it was selected in view of optimizing the solar cell performance after electron irradiation exposure to estimate the suitability of the thin-film QDSCs for space applications [138]. Moreover, the thin-film design included a 600 nm thick AlInP window layer to enable the fabrication of a nanostructured ARC [37, 139]. As a reference, a wafer-based QDSC with similar QD layer structures was used. The electrical contacts for the wafer-based QDSC were fabricated using Ni/Au metals on the front side and Ti/Au metals on the backside deposited by electron beam evaporation. After the contact GaAs removal by selective wet etching using an $NH_3$:$H_2O_2$:$H_2O$ etchant, a double-layer ARC of $TiO_2$/$SiO_2$ was deposited by electron beam evaporation.

In the thin-film QDSC process, a planar Au reflector was deposited by electron beam evaporation on top of the *p*-GaAs contact layer. In addition, Pt/Au metals were deposited on top of the reflector with Pt acting as a diffusion barrier and Au as a bonding contact layer. The QDSC was indium bonded to a carrier and the substrate was thinned and polished to the thickness of ~100 µm with a Logitech PM5 precision lapping machine. The residual substrate was wet etched with a sulfuric acid -based solution until the etch stop layer, which was removed by HCl, revealing the *n*-GaAs contact layer. Next, the front contacts (Ni/Au) were deposited by electron beam evaporation using a photolithographic lift-off process. To define the perimeter of the QDSC, electrical isolation, i.e., mesa etching, was performed with a photoresist mask using both sulfuric acid -based and HCl-based solutions. Finally, the *n*-GaAs contact layer was removed by wet etching and a double-layer ARC ($TiO_2$/$SiO_2$) was deposited by electron beam evaporation using a photolithographic lift-off process. A schematic drawing of the thin-film QDSC with back reflector and a picture of the final device are presented in Figure 41. The EQE and the *IV* characteristics of the QDSC were measured with the setup introduced in section 4.1.1.

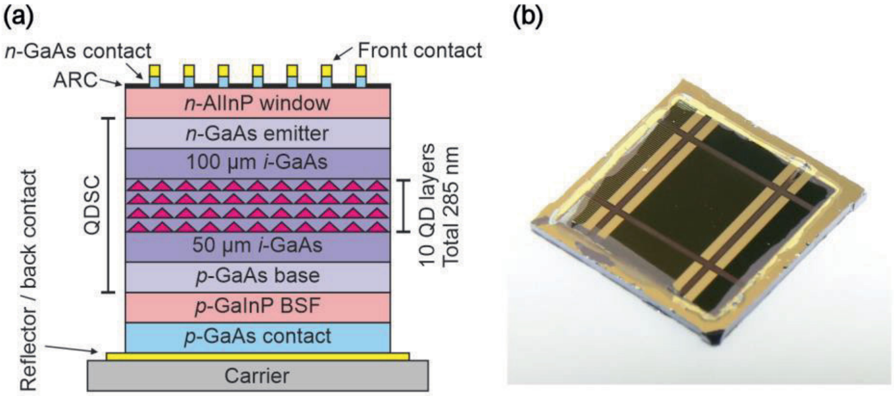

**Figure 41.** (a) A schematic drawing of the thin-film QDSC with back reflector. (b) A photograph of the final device.

In addition to the experimental measurements of the thin-film QDSC with back reflector, the performance of the QDSCs was simulated using an in-house developed numerical tool for QDSCs [140], validated against several experimental case studies [21, 141, 142]. A detailed description of the electrical and optical models can be found in [P4].

The measured and simulated EQE results are presented in Figure 42, showing the QD response in the wavelength range of 0.9–1.1 µm. The thin-film QDSC with back reflector produced increased EQE when compared to the wafer-based QDSC. The simulated data is well in line with the experimental results, showing only some deviation near 900 nm. This could be due to the fact that the simulations assume a sharp cut-off at 870 nm in the GaAs absorption profile whereas the fabrication process of the QDs produces an absorption band tail in the range between the GaAs band-edge and the QD wetting layer states [143]. The EQE data was used for calculating the $J_{sc}$ corresponding to the QDs by integrating over the AM1.5D (1000 W/m$^2$) solar spectrum in the wavelength range of 0.9–1.1 µm. The calculated results are presented in Table 4, which reveals that the thin-film QDSC with planar back reflector have approximately twice the current generation by the QDs when compared to the wafer-based QDSC.

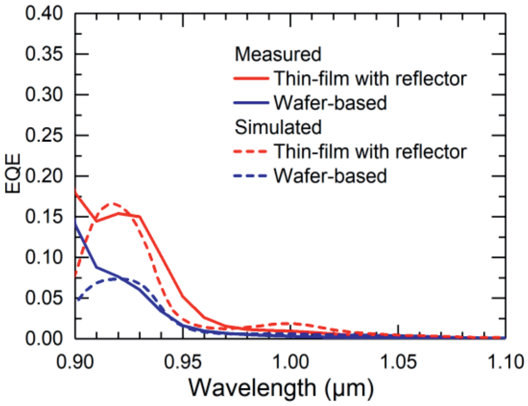

**Figure 42.** Measured and simulated EQE results for the thin-film QDSC with planar back reflector and for the wafer-based QDSC. The data is adopted from [P4].

The results from the *IV* measurements and from the simulations are presented in Figure 43, and the corresponding figures of merit are collected in Table 4. The simulations provide target values since they disregard any extrinsic recombination mechanism. Moreover, the simulated and measured $J_{sc}$ values are comparable with the note that the wafer-based QDSC has a thicker *p*-GaAs base, increasing the $J_{sc}$ when compared to the thin-film QDSC with back reflector. The measured FF of the thin-film QDSC is decreased compared to simulated value and is also lower than for the wafer-based QDSC. Most likely the difference is caused by the lack of an ohmic contact between the Au back reflector and the *p*-GaAs contact layer in the thin-film QDSC. Based on [P1] results, the ohmic contact should be formed by the Au reflector if the doping level is sufficiently high, which seems not to be the case in the thin-film QDSC, while for the wafer-based QDSC, the ohmic contact is formed between the highly doped *p*-GaAs substrate and the back metal.

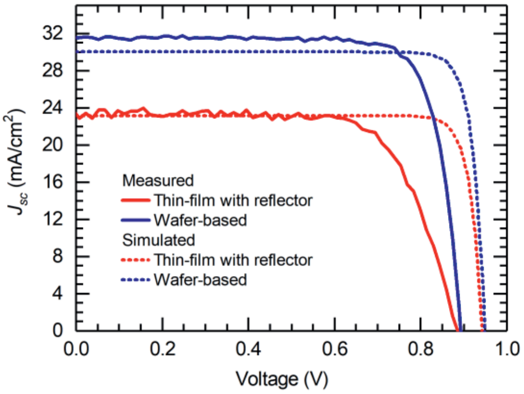

**Figure 43.** The measured and simulated *IV* results at AM1.5D (1000 W/m2). The data is adopted from [P4].

**Table 4.** The photocurrent generation of the QDs integrated from the EQE results together with the *IV* characteristics of the thin-film and wafer-based QDSC.

| Sample | $J_{sc}$ of QDs integrated from EQE (mA/cm$^2$) | $J_{sc}$ (mA/cm$^2$) | $V_{oc}$ (V) | FF (%) | Efficiency (%) |
|---|---|---|---|---|---|
| Thin-film with reflector | 0.35 | 23.4 | 0.884 | 71 | 14.7 |
| Thin-film with relfector simulated | 0.33 | 23.2 | 0.942 | 87 | 19.1 |
| Wafer-based | 0.17 | 31.5 | 0.892 | 80 | 22.4 |
| Wafer-based simulated | 0.16 | 30.0 | 0.948 | 87 | 24.9 |

The thin-film QDSC with back reflector exhibited a $V_{oc}$ of 0.884 V, which is high when compared to the reported values for other QDSCs [21, 32, 144]. However, it is ~60 mV lower than the simulated value. To understand the origin of the difference, *IV* measurements were performed with different concentrations for both the wafer-based and thin-film QDSCs. As presented in Figure 44, the $J_{sc}$ scales almost linearly with the concentration factor (C), confirming that both QDSCs are operating as a conventional single junction solar cell, whereas in the intermediate band operation the $J_{sc}$ scales super-linearly with C [32]. By expressing the $J_{sc}$ as

$$J_{sc}(\mathrm{C}) = \mathrm{C}J_{sc}^{1\,sun}, \tag{1}$$

and using the diode equation [145], the dependence of $V_{oc}$ on concentration can be written as

$$V_{oc}(\mathrm{C}) = V_{oc}^{1\,sun} + \eta V_T \ln(\mathrm{C}), \tag{2}$$

where $\eta$ is the diode ideality factor and $V_T$ the thermal voltage. The measured $V_{oc}$ is presented as a function of ln(C) in Figure 44, and by a linear fit, the extracted $\eta$ values are ~1.4 for the both QDSCs. This implies that the dark current has an extrinsic component, originating from nonradiative recombination in the intrinsic layers. This causes the 60 mV difference between the measured and simulated QDSC. Similar reduction of $V_{oc}$ occurs for both the wafer-based and the thin-film QDSC, proving that the $V_{oc}$ is otherwise preserved during the thin-film processing, while there is still room for improvement in terms of epitaxial growth.

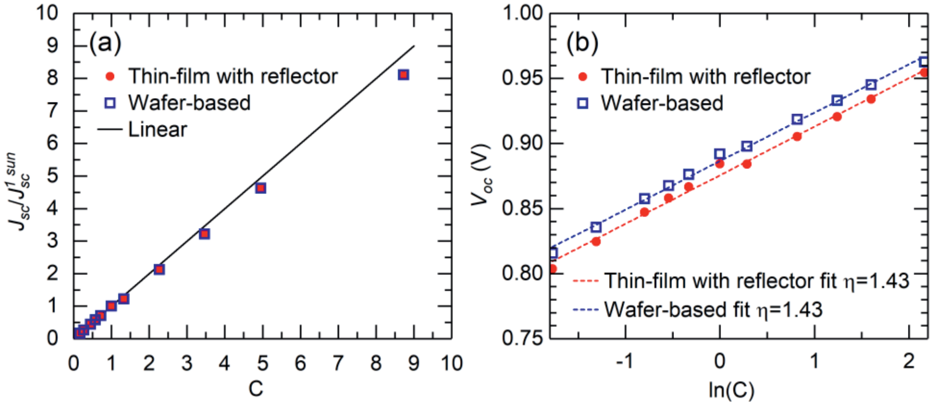

**Figure 44.** (a) $J_{sc}$ normalized by $J_{sc}$ at one sun as a function of C. (b) $V_{oc}$ as a function of ln(C). The data is adopted from [P4].

## 4.3 Thin-film QD solar cells with pyramid grating

The pyramid grating introduced in section 3.2.3 was implemented to the thin-film QDSC structures in two different configurations presented in Figure 45, and the photocurrent generation of the QDs was simulated. In the first approach shown in Figure 45(a) and introduced in [P2], the back reflector with pyramid gratings was fabricated into polymer and a Ag reflector was deposited below the grating. The second approach, shown in Figure 45(b) and introduced in [P5], included a pyramid grating formulated into a *p*-GaInP BSF layer with the addition of separate polymer planarization layer before deposition of the planar Ag reflector. This way the large surface area at the interface of the textured semiconductor and Ag could be avoided, decreasing the parasitic losses in the reflector [96].

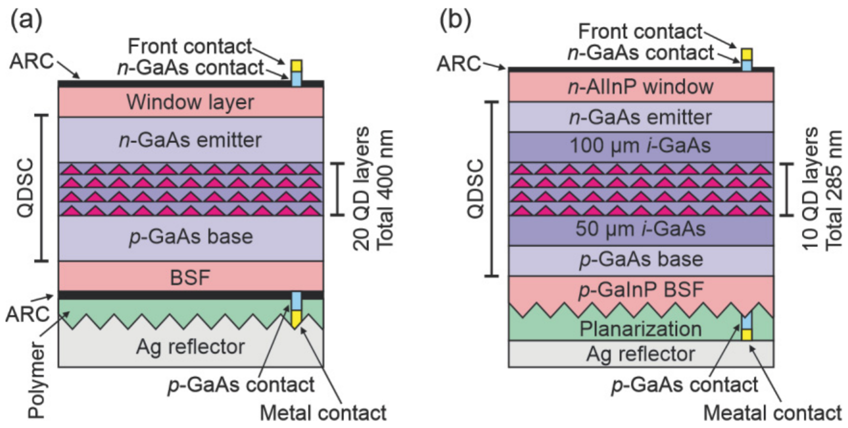

**Figure 45.** A schematic drawing of the thin-film QDSC with pyramid gratings. (a) The pyramid gratings are fabricated into the polymer [P2] and (b) into the BSF layer [P4].

In the first approach, the thin-film QDSC comprised a 2.6 µm thick GaAs active region embedding a stack of 20 InAs/GaAs QD layers with the overall thickness of about 400 nm [118, 122]. The ACRs on the top and on the bottom included single-layer $SiN_x$ having similar parameters as the ARCs presented in Figure 22. Further details on the QDSC structure can be found in [118]. The diffractive back reflector, introduced in section 3.2.3, included a pyramid grating in low refractive index polymer and a Ag layer. In the simulations, the optical model of the QDs was extracted from the EQE results presented in [21]. The absorbance spectrum was calculated by integrating the absorbed photon density only in the active region of the QDSC, thus disregarding the optical losses in the contact GaAs and metal layers.

The achieved absorbance spectrum is presented in Figure 46 for the thin-film QDSC with the reflector with pyramid grating. In addition, the absorbance spectra of the wafer-based QDSC and the thin-film QDSC with planar back reflector containing identical QDSC structures are included as references. The QDSC with pyramid grating shows significant increase in absorbance in the QD wavelength region with respect to the reference structures. The corresponding $J_{sc}$ values produced by the QD layers are calculated by integrating the absorbance over the AM1.5D (1000 $W/m^2$) spectrum in the wavelength range of 0.9–1.1 µm. The calculated results are summarized in Table 5, revealing a fourfold increase in the $J_{sc}$ of the QD layers when pyramid grating is applied. Already this is a remarkable result when considering the technological effort of the epitaxial growth required to achieve the same $J_{sc}$ of the QDs by increasing the number of QD layers. Further optimization of the applied diffractive grating design, e.g., employing higher index material for the pyramid grating could generate even higher current enhancements [21, 122]; this path was followed in the second approach.

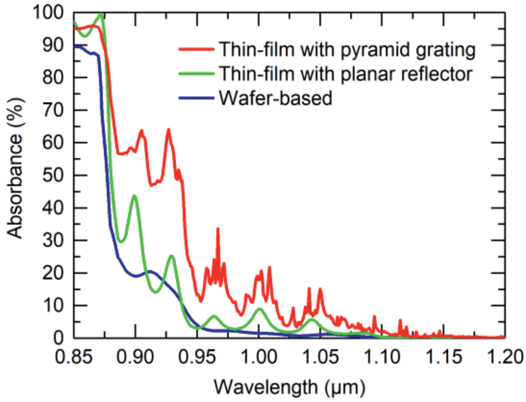

**Figure 46.** The simulated absorbance spectrum for the thin-film QDSC with pyramid gratings in polymer. In addition, the absorbance of the wafer-based QDSC and the thin-film QDSC with planar reflector are presented as a reference. The data is adopted from [P2].

As presented in Figure 45, the second approach included a pyramid grating fabricated into an GaInP BSF layer. The InAs/GaAs QDSC included 10 QD layers with an in-plane QD density of approximately $6\times10^{10}$ 1/cm², separated by ~30 nm thick *i*-GaAs layers. The total thickness of the absorbing layers was 0.75 μm. In addition, a double-layer ARC of $TiO_2/SiO_2$ was applied on top of the window layer.

The simulations of the QDSC were performed as described in [P4], and they utilize the 3D rigorous coupled wave analysis for the pyramid gratings [146]. The physical model was first validated and revised based on the experimental results of the QDSC with the planar reflector (see section 4.2). The calculated EQE spectrum for the thin-film QDSC with pyramid grating in BSF is shown in Figure 47, which also presents the reference EQE spectra of the wafer-based QDSC and the thin-film QDSC. The increase in the EQE of the QDSC with pyramid grating is remarkable owing to light being diffracted efficiently, resulting in multiple passes through the QD layers. The $J_{sc}$ produced by the QDs was again calculated by integrating the EQE results over the AM1.5D (1000 W/m²) spectrum in the wavelength range of 0.9–1.1 μm. The calculated $J_{sc}$ values are listed in Table 5, revealing a photocurrent generation of 0.189 mA/cm² per one QD layer for the QDSC with pyramid grating.

The $J_{sc}$ is approximately 12 times higher than the $J_{sc}$ of the wafer-based QDs. This improvement is instrumental in order to achieve high-efficiency QDSCs, since the absorption of the QDSC is enhanced without increasing the thermalization losses.

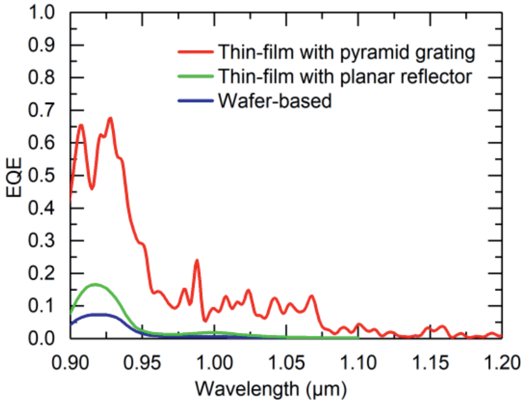

**Figure 47.** The simulated EQE spectrum for the thin-film QDSC with pyramid gratings in BSF. In addition, the EQE of the wafer-based QDSC and the thin-film QDSC with planar reflector are presented as a reference. The data is adopted from [P4].

**Table 5.** Calculated photocurrent generation over one QD layer at AM1.5D (1000 W/$m^2$) spectrum for approaches with the pyramid grating in polymer and the pyramid grating in BSF.

| Sample | Pyramid grating in polymer $J_{sc}$ over one QD layer (mA/$cm^2$) | Pyramid grating in BSF $J_{sc}$ over one QD layer (mA/$cm^2$) |
|---|---|---|
| Wafer-based | 0.022 | 0.016 |
| Thin-film with planar relfector | 0.034 | 0.033 |
| Thin film with pyramid grating | 0.090 | 0.189 |
| Improvement factor (pyramid/wafer) | 4.1 | 11.8 |

# 5 CONCLUSIONS AND FUTURE WORK

The III–V semiconductor solar cells exploring dilute nitride materials in MJSC architectures or InAs QDs in GaAs solar cells represent the active topics of research for emerging photovoltaic technology. Although both approaches enable improved spectral coverage, possibly leading to new levels of conversion efficiency, their operation suffers from reduced absorption in active area of the solar cells that falls below their theoretical potential. This is valid for dilute nitride solar cells with narrow bandgap and high N content or for QDSCs where the number of QD layers is limited in order to preserve good material quality. In this thesis, it was shown that these limitations can be alleviated by implementing a thin-film architecture employing back reflector for more efficient absorption, providing additional advantages in terms of functionality, i.e., flexibility, high power-to-weight ratio, and potentially lower costs related to the reuse of the substrate. Several demonstrations advancing the state-of-the-art technology have been made. The most notable results are:

i) Development of Ag/Cu planar back reflectors exhibiting high reflectance in the wavelength range of 0.9–1.4 µm. A thin 10 nm layer of Ag ensures a high reflectance and acts as a diffusion barrier to Cu. The studies revealed proper adhesion between the semiconductor and Ag/Cu reflectors and an ohmic contact functionality to the highly doped *p*-GaAs contact layer. The Ag/Cu reflector was found to withstand the processing temperatures of at least 200 °C.

ii) Back reflectors with diffractive grating were developed to increase the absorption length inside the active area of the solar cells. The best performance was obtained for a reflector with pyramid grating. The polymer used for pyramid grating fabrication was investigated in terms of radiation hardness, indicating suitability for space applications.

iii) Demonstration of state-of-the-art EQE for 1 eV dilute nitride solar cells with Ag/Cu planar back reflectors when compared to the other planar reflectors. A solar cell with Ag/Cu reflector exhibited an estimated $J_{sc}$ of ~14 mA/cm$^2$ at AM1.5D (1000 W/m$^2$) under a GaAs filter, fulfilling the needs for current matching in MJSCs with more than three junctions.

iv) First demonstration of ~0.8 eV GaInNAsSb solar cells with planar Au back reflector. The highest EQE corresponded to $J_{sc}$ of 15.4 mA/cm$^2$ under AM1.5D (1000 W/m$^2$) spectral conditions, sufficient for current matching in MJSCs. Although the experimental results exhibited relatively low $V_{oc}$ values, they were comparable to the values of diffused Ge solar cells.

v) Demonstration of thin-film InAs/GaAs QD solar cells with planar back reflector showing a two-fold increase in the current generation of the QD absorber compared to a reference wafer-based solar cell. The $V_{oc}$ remained at the same level as for the wafer-based QDSC, indicating that the thin-film processing does not degrade the electrical performance. The demonstrated $V_{oc}$ of 0.884 V is one of the highest reported for MBE-grown QDSCs.

vi) Performing a realistic simulation study for QDSCs utilizing reflector with pyramid grating using a parametrized model based on the experimental results. When compared to the wafer-based QDSC, a four times higher current generation in the QD layers was achieved when the pyramid gratings are fabricated into the polymer. On the other hand, the current enhancement corresponding to the QD absorbers was 12 times higher when fabricating the pyramid grating into BSF layer with the planarization polymer. This is a significant result considering the technological effort required to fabricate 12 times more QD layers to achieve similar current generation ability.

The experimental implementation of the developed pyramid gratings in connection with InAs/GaAs QDSC is an important part of the work continuation path. Moreover, in terms of achieving state-of-the-art efficiencies, the most important future development is to fabricate MJSC with dilute nitride junction (four of more junctions) with pyramid grating. Ultimately, this should enable reaching the conversion efficiency of over 50% while exploiting a mechanically stable lattice matched solar cell architecture.

# 6 REFERENCES

[1] J. Liu, Y. Yao, S. Xiao, and X. Gu, "Review of status developments of high-efficiency crystalline silicon solar cells", *Journal of Physics D: Applied Physics,* vol. 51(12), pp. 123001, 2018.

[2] M. A. Green, E. D. Dunlop, D. H. Levi, J. Hohl-Ebinger, M. Yoshita, and A. W. Ho-Baillie, "Solar cell efficiency tables (version 54)", *Progress in Photovoltaics: Research and Applications,* vol. 27(7), pp. 565-575, 2019.

[3] S. P. Philipps, F. Dimroth, and A. W. Bett, "High-efficiency III-V multijunction solar cells", in: S.A. Kalogirou (ed.), *McEvoy's Handbook of Photovoltaics,* 3rd ed., Elsevier, pp. 439-472, 2018.

[4] J. F. Geisz, R. M. France, K. L. Schulte, M. A. Steiner, A. G. Norman, H. L. Guthrey, M. R. Young, T. Song, and T. Moriarty, "Six-junction III-V solar cells with 47.1% conversion efficiency under 143 Suns concentration", *Nature Energy,* vol. 5(4), pp. 326-335, 2020.

[5] E. Vartiainen, G. Masson, C. Breyer, D. Moser, and E. Román Medina, "Impact of weighted average cost of capital, capital expenditure, and other parameters on future utility-scale PV levelised cost of electricity", *Progress in Photovoltaics: Research and Applications,* vol. 28(6), pp. 439-453, 2020.

[6] R. R. King, C. M. Fetzer, D. C. Law, K. M. Edmondson, H. Yoon, G. S. Kinsey, D. D. Krut, J. H. Ermer, P. Hebert, and B. T. Cavicchi, "Advanced III-V multijunction cells for space", in Proceedings of *IEEE 4th World Conference on Photovoltaic Energy Conference,* Waikoloa, HI, USA, pp. 1757-1762, 2006.

[7] B. Danilchenko, A. Budnyk, L. Shpinar, D. Poplavskyy, S. E. Zelensky, K. Barnham, and N. J. Ekins-Daukes, "1 MeV electron irradiation influence on GaAs solar cell performance", *Solar Energy Materials and Solar Cells,* vol. 92(11), pp. 1336-1340, 2008.

[8] C. Pellegrino, A. Gagliardi, and C. G. Zimmermann, "Impact of Proton and Electron Irradiation-Induced Defects on the Dark Current of GaAs Solar Cells", *IEEE Journal of Photovoltaics,* vol. 9(6), pp. 1661-1667, 2019.

[9] A. L. Luque and V. M. Andreev, *Concentrator photovoltaics,* Springer, 2007.

[10] NREL Best Research-Cell Efficiency Chart, available: https://www.nrel.gov/pv/cell-efficiency.html, cited 9.6.2020.

[11] Solar Array, available: https://commons.wikimedia.org/wiki/File:Solar_array_(49720105191).jpg, cited 9.6.2020.

[12] ISS March 2009, available: https://commons.wikimedia.org/wiki/File:ISS_March_2009.jpg, cited 9.6.2020.

[13] S. Bailey, J. McNatt, R. Raffaelle, S. Hubbard, D. Forbes, L. Fritzenmeier, and W. Maurer, "The future of space photovoltaics", in Proceedings of *IEEE 34th Photovoltaic Specialists Conference (PVSC),* Philadelphia, PA, USA, pp. 1909, 2009.

[14] M. A. Green, K. Emery, Y. Hishikawa, W. Warta, and E. D. Dunlop, "Solar cell efficiency tables (version 48)", *Progress in Photovoltaics: Research and Applications,* vol. 24(7), pp. 905-913, 2016.

[15] A. Luque, "Will we exceed 50% efficiency in photovoltaics?", *Journal of Applied Physics,* vol. 110(3), pp. 031301, 2011.

[16] D. J. Friedman, J. F. Geisz, S. R. Kurtz, and J. M. Olson, "1-eV GaInNAs solar cells for ultrahigh-efficiency multijunction devices", in Proceedings of *2nd World Conference and Exhibition on Photovoltaic Solar Energy Conversion,* Vienna, Austria, pp. 6-10, 1998.

[17] W. Guter, J. Schöne, S. P. Philipps, M. Steiner, G. Siefer, A. Wekkeli, E. Welser, E. Oliva, A. W. Bett, and F. Dimroth, "Current-matched triple-junction solar cell reaching 41.1% conversion efficiency under concentrated sunlight", *Applied Physics Letters,* vol. 94(22), pp. 223504, 2009.

[18] J. S. Harris, R. Kudrawiec, H. B. Yuen, S. R. Bank, H. P. Bae, M. A. Wistey, D. Jackrel, E. R. Pickett, T. Sarmiento, and L. L. Goddard, "Development of GaInNAsSb alloys: growth, band structure, optical properties and applications", *physica status solidi (b),* vol. 244(8), pp. 2707-2729, 2007.

[19] A. Aho, A. Tukiainen, V. Polojärvi, and M. Guina, "Performance assessment of multijunction solar cells incorporating GaInNAsSb", *Nanoscale research letters,* vol. 9(1), pp. 1-7, 2014.

[20] V. Aroutiounian, S. Petrosyan, A. Khachatryan, and K. Touryan, "Quantum dot solar cells", *Journal of Applied Physics,* vol. 89(4), pp. 2268-2271, 2001.

[21] F. Cappelluti, M. van Eerden, A. P. Cédola, T. Aho, G. Bissels, F. Elsehrawy, J. Wu, H. Liu, P. Mulder, G. J. Bauhuis, J. J. Schermer, T. Niemi, and M. Guina, "Light-trapping enhanced thin-film III-V quantum dot solar cells fabricated by epitaxial lift-off", *Solar Energy Materials and Solar Cells,* vol. 181, pp. 83-92, 2018.

[22] A. Luque and A. Martí, "Increasing the efficiency of ideal solar cells by photon induced transitions at intermediate levels", *Physical Review Letters,* vol. 78(26), pp. 5014, 1997.

[23] W. Ho, Y. Lee, G. Yang, and C. Chang, "Optical and electrical characteristics of high-efficiency InGaP/InGaAs/Ge triple-junction solar cell incorporated with InGaAs/GaAs QD layers in the middle cell", *Progress in Photovoltaics: Research and Applications,* vol. 24(4), pp. 551-559, 2016.

[24] C. Kerestes, S. Polly, D. Forbes, C. Bailey, A. Podell, J. Spann, P. Patel, B. Richards, P. Sharps, and S. Hubbard, "Fabrication and analysis of multijunction solar cells with a quantum dot (In)GaAs junction", *Progress in Photovoltaics: Research and Applications,* vol. 22(11), pp. 1172-1179, 2014.

[25] A. Mellor, A. Luque, I. Tobías, and A. Martí, "The feasibility of high-efficiency InAs/GaAs quantum dot intermediate band solar cells", *Solar Energy Materials and Solar Cells,* vol. 130, pp. 225-233, 2014.

[26] K. Sakamoto, Y. Kondo, K. Uchida, and K. Yamaguchi, "Quantum-dot density dependence of power conversion efficiency of intermediate-band solar cells", *Journal of Applied Physics,* vol. 112(12), pp. 124515, 2012.

[27] T. Sugaya, O. Numakami, R. Oshima, S. Furue, H. Komaki, T. Amano, K. Matsubara, Y. Okano, and S. Niki, "Ultra-high stacks of InGaAs/GaAs quantum dots for high efficiency solar cells", *Energy & Environmental Science,* vol. 5(3), pp. 6233-6237, 2012.

[28] D. Guimard, R. Morihara, D. Bordel, K. Tanabe, Y. Wakayama, M. Nishioka, and Y. Arakawa, "Fabrication of InAs/GaAs quantum dot solar cells with enhanced photocurrent and without degradation of open circuit voltage", *Applied Physics Letters,* vol. 96(20), pp. 203507, 2010.

[29] C. G. Bailey, D. V. Forbes, S. J. Polly, Z. S. Bittner, Y. Dai, C. Mackos, R. P. Raffaelle, and S. M. Hubbard, "Open-circuit voltage improvement of InAs/GaAs

quantum-dot solar cells using reduced InAs coverage", *IEEE Journal of Photovoltaics,* vol. 2(3), pp. 269-275, 2012.

[30] P. Campbell and M. A. Green, "Light trapping properties of pyramidally textured surfaces", *Journal of Applied Physics,* vol. 62(1), pp. 243-249, 1987.

[31] G. Lush and M. Lundstrom, "Thin film approaches for high-efficiency III-V cells", *Solar Cells,* vol. 30(1-4), pp. 337-344, 1991.

[32] T. Sogabe, Y. Shoji, P. Mulder, J. Schermer, E. Tamayo, and Y. Okada, "Enhancement of current collection in epitaxial lift-off InAs/GaAs quantum dot thin film solar cell and concentrated photovoltaic study", *Applied Physics Letters,* vol. 105(11), pp. 113904, 2014.

[33] M. F. Bennett, Z. S. Bittner, D. V. Forbes, S. Rao Tatavarti, S. Phillip Ahrenkiel, A. Wibowo, N. Pan, K. Chern, and S. M. Hubbard, "Epitaxial lift-off of quantum dot enhanced GaAs single junction solar cells", *Applied Physics Letters,* vol. 103(21), pp. 213902, 2013.

[34] B. L. Smith, M. A. Slocum, Z. S. Bittner, Y. Dai, G. T. Nelson, S. D. Hellstroem, R. Tatavarti, and S. M. Hubbard, "Inverted growth evaluation for epitaxial lift off (ELO) quantum dot solar cell and enhanced absorption by back surface texturing", in Proceedings of *IEEE 43rd Photovoltaic Specialists Conference (PVSC),* Portland, OR, USA, pp. 1276-1281, 2016.

[35] F. Cappelluti, G. Ghione, M. Gioannini, G. Bauhuis, P. Mulder, J. Schermer, M. Cimino, G. Gervasio, G. Bissels, and E. Katsia, "Novel concepts for high-efficiency lightweight space solar cells", in Proceedings of *11th European Space Power Conference,* Thessaloniki, Greece, pp. 03007, 2017.

[36] N. Baldock and M. R. Mokhtarzadeh-Dehghan, "A study of solar-powered, high-altitude unmanned aerial vehicles", *Aircraft Engineering and Aerospace Technology,* vol. 78(3), pp. 187-193, 2006.

[37] J. Tommila, V. Polojärvi, A. Aho, A. Tukiainen, J. Viheriälä, J. Salmi, A. Schramm, J. M. Kontio, A. Turtiainen, and T. Niemi, "Nanostructured broadband antireflection coatings on AlInP fabricated by nanoimprint lithography", *Solar Energy Materials and Solar Cells,* vol. 94(10), pp. 1845-1848, 2010.

[38] K. Tsui, Q. Lin, H. Chou, Q. Zhang, H. Fu, P. Qi, and Z. Fan, "Low-Cost, Flexible, and Self-Cleaning 3D Nanocone Anti-Reflection Films for High-Efficiency Photovoltaics", *Advanced Materials,* vol. 26(18), pp. 2805-2811, 2014.

[39] S. Chhajed, M. F. Schubert, J. K. Kim, and E. F. Schubert, "Nanostructured multilayer graded-index antireflection coating for Si solar cells with broadband and omnidirectional characteristics", *Applied Physics Letters,* vol. 93(25), pp. 251108, 2008.

[40] S. A. Boden and D. M. Bagnall, "Tunable reflection minima of nanostructured antireflective surfaces", *Applied Physics Letters,* vol. 93(13), pp. 133108, 2008.

[41] J. L. Gray, "The physics of the solar cell", in: A. Luque and S. Hegedus (ed.), *Handbook of photovoltaic science and engineering,* 2nd ed., Wiley Online Library, pp. 82-128, 2011.

[42] A. McEvoy, T. Markvart, and L. Castañer, *Solar cells: materials, manufacture and operation,* 2nd ed., Academic Press, 2012.

[43] N. J. Ekins-Daukes, "III-V solar cells", in: A. Willoughby (ed.), *Solar cell materials: Developing technologies,* Wiley Online Library, pp. 113-143, 2014.

[44] N. Dharmarasu and H. Hillmer, "Compound Semiconductors", in: Y.B. Gianchandani, O. Tabata, and H. Zappe (ed.), *Comprehensive Microsystems,* Elsevier, pp. 25-51, 2008.

[45] M. Guina and S. M. Wang, "MBE of dilute-nitride optoelectronic devices", in: M. Henini (ed.), *Molecular Beam Epitaxy: From Research to Mass Production,* Elsevier, pp. 171-187, 2013.

[46] J. N. Roy and D. N. Bose, *Photovoltaic Science and Technology,* Cambridge University Press, 2018.

[47] M. Raappana, "Wet etching of dilute nitride and antimonide semiconductors for solar cells", M.Sc. Thesis, Tampere University of Technology, 2015.

[48] W. Shockley and H. J. Queisser, "Detailed balance limit of efficiency of p-n junction solar cells", *Journal of Applied Physics,* vol. 32(3), pp. 510-519, 1961.

[49] O. D. Miller, E. Yablonovitch, and S. R. Kurtz, "Strong internal and external luminescence as solar cells approach the Shockley–Queisser limit", *IEEE Journal of Photovoltaics,* vol. 2(3), pp. 303-311, 2012.

[50] S. Rühle, "Tabulated values of the Shockley–Queisser limit for single junction solar cells", *Solar Energy,* vol. 130, pp. 139-147, 2016.

[51] "ASTM G173-03: Standard Tables for Reference Solar Spectral Irradiances: Direct Normal and Hemispherical on 37° Tilted Surface", ASTM International, West Conshohocken, PA, www.astm.org, 2003.

[52] M. S. Leite, R. L. Woo, J. N. Munday, W. D. Hong, S. Mesropian, D. C. Law, and H. A. Atwater, "Towards an optimized all lattice-matched InAlAs/InGaAsP/InGaAs multijunction solar cell with efficiency> 50%", *Applied Physics Letters,* vol. 102(3), pp. 033901, 2013.

[53] R. R. King, A. Boca, W. Hong, X. Q. Liu, D. Bhusari, D. Larrabee, K. M. Edmondson, D. C. Law, C. M. Fetzer, and S. Mesropian, "Band-gap-engineered architectures for high-efficiency multijunction concentrator solar cells", in Proceedings of *24th European Photovoltaic Solar Energy Conference and Exhibition,* Hamburg, Germany, pp. 55, 2009.

[54] A. Aho, R. Isoaho, L. Hytönen, T. Aho, M. Raappana, V. Polojärvi, A. Tukiainen, J. Reuna, S. Mäkelä, and M. Guina, "Lattice-matched four-junction tandem solar cell including two dilute nitride bottom junctions", *Progress in Photovoltaics: Research and Applications,* vol. 27(4), pp. 299-305, 2019.

[55] R. Isoaho, A. Aho, A. Tukiainen, T. Aho, M. Raappana, T. Salminen, J. Reuna, and M. Guina, "Photovoltaic properties of low-bandgap (0.7-0.9 eV) lattice-matched GaInNAsSb solar junctions grown by molecular beam epitaxy on GaAs", *Solar Energy Materials and Solar Cells,* vol. 195, pp. 198-203, 2019.

[56] M. A. Green, K. Emery, Y. Hishikawa, W. Warta, and E. D. Dunlop, "Solar cell efficiency tables (version 41)", *Progress in Photovoltaics: Research and Applications,* vol. 21(1), pp. 1-11, 2013.

[57] D. Derkacs, R. Jones-Albertus, F. Suarez, and O. Fidaner, "Lattice-matched multijunction solar cells employing a 1 eV GaInNAsSb bottom cell", *Journal of Photonics for Energy,* vol. 2(1), pp. 021805, 2012.

[58] F. Dimroth, M. Grave, P. Beutel, U. Fiedeler, C. Karcher, T. N. Tibbits, E. Oliva, G. Siefer, M. Schachtner, and A. Wekkeli, "Wafer bonded four-junction GaInP/GaAs//GaInAsP/GaInAs concentrator solar cells with 44.7% efficiency", *Progress in Photovoltaics: Research and Applications,* vol. 22(3), pp. 277-282, 2014.

[59] T. N. Tibbits, P. Beutel, M. Grave, C. Karcher, E. Oliva, G. Siefer, A. Wekkeli, M. Schachtner, F. Dimroth, and A. W. Bett, "New efficiency frontiers with wafer-bonded multi-junction solar cells", in Proceedings of *29th European PV Solar Energy Conference and Exhibition,* Amsterdam, Netherlands, pp. 1-4, 2014.

[60] M. Kondow, T. Kitatani, M. C. Larson, K. Nakahara, K. Uomi, and H. Inoue, "Gas-source MBE of GaInNAs for long-wavelength laser diodes", *Journal of Crystal Growth,* vol. 188(1-4), pp. 255-259, 1998.

[61] D. B. Jackrel, S. R. Bank, H. B. Yuen, M. A. Wistey, J. S. Harris Jr, A. J. Ptak, S. W. Johnston, D. J. Friedman, and S. R. Kurtz, "Dilute nitride GaInNAs and GaInNAsSb solar cells by molecular beam epitaxy", *Journal of Applied Physics,* vol. 101(11), pp. 114916, 2007.

[62] A. W. Bett, S. P. Philipps, S. Essig, S. Heckelmann, R. Kellenbenz, V. Klinger, M. Niemeyer, D. Lackner, and F. Dimroth, "Overview about technology perspectives for high efficiency solar cells for space and terrestrial applications", in Proceedings of *28th European Photovoltaic Solar Energy Conference and Exhibition,* Paris, France, pp. 1-6, 2013.

[63] A. J. Ptak, S. W. Johnston, S. Kurtz, D. J. Friedman, and W. K. Metzger, "A comparison of MBE-and MOCVD-grown GaInNAs", *Journal of Crystal Growth,* vol. 251(1-4), pp. 392-398, 2003.

[64] S. Tixier, S. E. Webster, E. C. Young, T. Tiedje, S. Francoeur, A. Mascarenhas, P. Wei, and F. Schiettekatte, "Band gaps of the dilute quaternary alloys $GaN_xAs_{1-x-y}Bi_y$ and $Ga_{1-y}In_yN_xAs_{1-x}$", *Applied Physics Letters,* vol. 86(11), pp. 112113, 2005.

[65] F. Langer, S. Perl, S. Höfling, and M. Kamp, "p-to n-type conductivity transition in 1.0 eV GaInNAs solar cells controlled by the V/III ratio", *Applied Physics Letters,* vol. 106(6), pp. 063905, 2015.

[66] S. L. Tan, W. M. Soong, M. J. Steer, S. Zhang, J. S. Ng, and J. P. David, "Dilute nitride GaInNAs and GaInNAsSb for solar cell applications", in Proceedings of *Physics, Simulation, and Photonic Engineering of Photovoltaic Devices,* San Francisco, CA, USA, pp. 82561E, 2012.

[67] A. J. Ptak, D. J. Friedman, and S. Kurtz, "Effects of temperature, nitrogen ions, and antimony on wide depletion width GaInNAs", *Journal of Vacuum Science & Technology B: Microelectronics and Nanometer Structures Processing, Measurement, and Phenomena,* vol. 25(3), pp. 955-959, 2007.

[68] A. J. Ptak, D. J. Friedman, S. R. Kurtz, and R. C. Reedy, "Low-acceptor-concentration GaInNAs grown by molecular-beam epitaxy for high-current pin solar cell applications", *Journal of Applied Physics,* vol. 98(9), pp. 094501, 2005.

[69] A. Aho, V. Polojärvi, V. Korpijärvi, J. Salmi, A. Tukiainen, P. Laukkanen, and M. Guina, "Composition dependent growth dynamics in molecular beam epitaxy of

GaInNAs solar cells", *Solar Energy Materials and Solar Cells,* vol. 124, pp. 150-158, 2014.

[70] A. Gubanov, V. Polojärvi, A. Aho, A. Tukiainen, N. V. Tkachenko, and M. Guina, "Dynamics of time-resolved photoluminescence in GaInNAs and GaNAsSb solar cells", *Nanoscale Research Letters,* vol. 9(1), pp. 1-4, 2014.

[71] V. Polojärvi, A. Aho, A. Tukiainen, A. Schramm, and M. Guina, "Comparative study of defect levels in GaInNAs, GaNAsSb, and GaInNAsSb for high-efficiency solar cells", *Applied Physics Letters,* vol. 108(12), pp. 122104, 2016.

[72] V. Polojärvi, A. Aho, A. Tukiainen, M. Raappana, T. Aho, A. Schramm, and M. Guina, "Influence of As/group-III flux ratio on defects formation and photovoltaic performance of GaInNAs solar cells", *Solar Energy Materials and Solar Cells,* vol. 149, pp. 213-220, 2016.

[73] D. Redfield, "Multiple-pass thin-film silicon solar cell", *Applied Physics Letters,* vol. 25(11), pp. 647-648, 1974.

[74] R. Oshima, A. Takata, and Y. Okada, "Strain-compensated InAs/GaNAs quantum dots for use in high-efficiency solar cells", *Applied Physics Letters,* vol. 93(8), pp. 083111, 2008.

[75] F. Cappelluti, A. Tukiainen, T. Aho, F. Elsehrawy, N. Gruginskie, M. van Eerden, G. Bissels, A. Tibaldi, G. J. Bauhuis, and P. Mulder, "Quantum Dot-Based Thin-Film III-V Solar Cells", in: P. Yu and Z.M. Wang (ed.), *Quantum Dot Optoelectronic Devices,* Springer, pp. 1-48, 2020.

[76] S. M. Hubbard, C. D. Cress, C. G. Bailey, R. P. Raffaelle, S. G. Bailey, and D. M. Wilt, "Effect of strain compensation on quantum dot enhanced GaAs solar cells", *Applied Physics Letters,* vol. 92(12), pp. 123512, 2008.

[77] F. Cappelluti, M. Gioannini, G. Ghione, and A. Khalili, "Numerical study of thin-film quantum-dot solar cells combining selective doping and light-trapping approaches", in Proceedings of *IEEE 43rd Photovoltaic Specialists Conference (PVSC),* Portland, OR, USA, pp. 1282-1286, 2016.

[78] E. Yablonovitch, T. Gmitter, J. P. Harbison, and R. Bhat, "Extreme selectivity in the lift-off of epitaxial GaAs films", *Applied Physics Letters,* vol. 51(26), pp. 2222-2224, 1987.

[79] Logitech PM6 precision lapping & polishing system, available: https://logitech.uk.com/product/pm6-precision-lapping-polishing-system, cited 9.7.2020.

[80] A. R. Clawson, "Guide to references on III–V semiconductor chemical etching", *Materials Science and Engineering: R: Reports,* vol. 31(1-6), pp. 1-438, 2001.

[81] A. G. Baca and C. I. H. Ashby, *Fabrication of GaAs devices,* IET, 2005.

[82] M. Konagai, M. Sugimoto, and K. Takahashi, "High efficiency GaAs thin film solar cells by peeled film technology", *Journal of Crystal Growth,* vol. 45, pp. 277-280, 1978.

[83] J. J. Schermer, P. Mulder, G. J. Bauhuis, M. Voncken, J. Van Deelen, E. Haverkamp, and P. K. Larsen, "Epitaxial Lift-Off for large area thin film III/V devices", *physica status solidi (a),* vol. 202(4), pp. 501-508, 2005.

[84] K. Lee, J. D. Zimmerman, T. W. Hughes, and S. R. Forrest, "Non-destructive wafer recycling for low-cost thin-film flexible optoelectronics", *Advanced Functional Materials,* vol. 24(27), pp. 4284-4291, 2014.

[85] N. Vandamme, C. Hung-Ling, A. Gaucher, B. Behaghel, A. Lemaitre, A. Cattoni, C. Dupuis, N. Bardou, J. Guillemoles, and S. Collin, "Ultrathin GaAs solar cells with a silver back mirror", *IEEE Journal of Photovoltaics,* vol. 5(2), pp. 565-570, 2015.

[86] G. J. Bauhuis, P. Mulder, E. J. Haverkamp, J. J. Schermer, E. Bongers, G. Oomen, W. Köstler, and G. Strobl, "Wafer reuse for repeated growth of III–V solar cells", *Progress in Photovoltaics: Research and Applications,* vol. 18(3), pp. 155-159, 2010.

[87] K. Xiong, H. Mi, T. Chang, M. Wu, S. Gong, W. Zhou, M. Arnold, H. Yuan, and Z. Ma, "AlGaAs/Si dual-junction tandem solar cells fabricated by epitaxial lift-off and print transfer-assisted bonding", in Proceedings of *IEEE 42nd Photovoltaic Specialist Conference (PVSC),* New Orlean, LA, USA, pp. 1-3, 2015.

[88] W. Choi, C. Z. Kim, C. S. Kim, W. Heo, T. Joo, S. Y. Ryu, H. Kim, H. Kim, H. K. Kang, and S. Jo, "A Repeatable Epitaxial Lift-Off Process from a Single GaAs Substrate for Low-Cost and High-Efficiency III-V Solar Cells", *Advanced Energy Materials,* vol. 4(16)2014.

[89] K. Lee, J. Lee, B. A. Mazor, and S. R. Forrest, "Epitaxial lift-off processed GaAs thin-film solar cells integrated with low-cost plastic mini-compound parabolic

concentrators", in Proceedings of *IEEE 40th Photovoltaic Specialist Conference (PVSC),* Denver, CO, USA, pp. 2127-2129, 2014.

[90] C. Cheng, K. Shiu, N. Li, S. Han, L. Shi, and D. K. Sadana, "Epitaxial lift-off process for gallium arsenide substrate reuse and flexible electronics", *Nature Communications,* vol. 4, pp. 1577, 2013.

[91] C. Youtsey, R. McCarthy, R. Reddy, K. Forghani, A. Xie, E. Beam, J. Wang, P. Fay, T. Ciarkowski, and E. Carlson, "Wafer-scale epitaxial lift-off of GaN using bandgap-selective photoenhanced wet etching", *physica status solidi (b),* vol. 254(8), pp. 1600774, 2017.

[92] R. Tatavarti, G. Hillier, A. Dzankovic, G. Martin, F. Tuminello, R. Navaratnarajah, G. Du, D. P. Vu, and N. Pan, "Lightweight, low cost GaAs solar cells on 4" epitaxial liftoff (ELO) wafers", in Proceedings of *IEEE 33rd Photovoltaic Specialists Conference (PVSC),* San Diego, CA, USA, pp. 1-4, 2008.

[93] A. T. van Niftrik, J. J. Schermer, G. J. Bauhuis, J. van Deelen, P. Mulder, and P. K. Larsen, "The influence of $In_xGa_{1-x}As$ and $GaAs_{1-y}P_y$ layers surrounding the AlAs release layer in the epitaxial lift-off process", *Crystal Growth and Design,* vol. 7(12), pp. 2472-2480, 2007.

[94] D. Cardwell and N. Pan, "Triple Junction GaAs High Efficiency Epitaxial Lift-Off Solar Cells", in Proceedings of *Optics for Solar Energy,* Singapore, Singapore, pp. OW5C.6, 2018.

[95] N. Pan, "Epitaxial lift-off of large-area GaAs multi-junction solar cells for high efficiency clean and portable energy power generation", in Proceedings of *IEEE International Conference on Semiconductor Electronics (ICSE),* Kuala Lumpur, Malaysia, pp. 347-349, 2014.

[96] S. Mokkapati and K. R. Catchpole, "Nanophotonic light trapping in solar cells", *Journal of Applied Physics,* vol. 112(10), pp. 101101, 2012.

[97] Z. C. Holman, M. Filipič, B. Lipovšek, S. De Wolf, F. Smole, M. Topič, and C. Ballif, "Parasitic absorption in the rear reflector of a silicon solar cell: Simulation and measurement of the sub-bandgap reflectance for common dielectric/metal reflectors", *Solar Energy Materials and Solar Cells,* vol. 120, pp. 426-430, 2014.

[98] M. Keshavarz Hedayati and M. Elbahri, "Antireflective coatings: Conventional stacking layers and ultrathin plasmonic metasurfaces, a mini-review", *Materials,* vol. 9(6), pp. 497, 2016.

[99] M. F. Schubert, F. W. Mont, S. Chhajed, D. J. Poxson, J. K. Kim, and E. F. Schubert, "Design of multilayer antireflection coatings made from co-sputtered and low-refractive-index materials by genetic algorithm", *Optics express,* vol. 16(8), pp. 5290-5298, 2008.

[100] M. Keshavarz Hedayati, M. Abdelaziz, C. Etrich, S. Homaeigohar, C. Rockstuhl, and M. Elbahri, "Broadband anti-reflective coating based on plasmonic nanocomposite", *Materials,* vol. 9(8), pp. 636, 2016.

[101] R. Tatavarti, A. Wibowo, G. Martin, F. Tuminello, C. Youtsey, G. Hillier, N. Pan, M. W. Wanlass, and M. Romero, "InGaP/GaAs/InGaAs inverted metamorphic (IMM) solar cells on 4" epitaxial lifted off (ELO) wafers", in Proceedings of *IEEE 35th Photovoltaic Specialists Conference (PVSC),* Honolulu, HI, USA, pp. 2125, 2010.

[102] J. Long, M. Xiao, X. Huang, Z. Xing, X. Li, P. Dai, M. Tan, Y. Wu, M. Song, and S. Lu, "High efficiency thin film GaInP/GaAs/InGaAs inverted metamorphic (IMM) solar cells based on electroplating process", *Journal of Crystal Growth,* vol. 513, pp. 38-42, 2019.

[103] A. P. Kirk, D. W. Cardwell, J. D. Wood, A. Wibowo, K. Forghani, D. Rowell, N. Pan, and M. Osowski, "Recent progress in epitaxial lift-off solar cells", in Proceedings of *IEEE 7th World Conference on Photovoltaic Energy Conversion (WCPEC),* Waikoloa, HI, USA, pp. 32, 2018.

[104] X. Huang, J. Long, D. Wu, S. Ye, X. Li, Q. Sun, Z. Xing, W. Yang, M. Song, and Y. Guo, "Flexible four-junction inverted metamorphic AlGaInP/AlGaAs/In0. 17Ga0. 83As/In0. 47Ga0. 53As solar cell", *Solar Energy Materials and Solar Cells,* vol. 208, pp. 110398, 2020.

[105] N. Miyashita, N. Ahsan, Y. Okada, R. Tatavarti, A. Wibowo, and N. Pan, "Epitaxial Lifted-Off Thin Film GaInP/GaAs/GaInNAsSb Lattice-Matched Triple Junction Solar Cells", in Proceedings of *IEEE 46th Photovoltaic Specialists Conference (PVSC),* Chicago, IL, USA, pp. 1502-1505, 2019.

[106] S. R. Tatavarti, Z. S. Bittner, A. Wibowo, M. A. Slocum, G. Nelson, H. Kum, S. P. Ahrenkiel, and S. M. Hubbard, "Epitaxial Lift-off (ELO) of InGaP/GaAs/InGaAs solar cells with quantum dots in GaAs middle sub-cell", *Solar Energy Materials and Solar Cells,* vol. 185, pp. 153-157, 2018.

[107] M. J. Weber, *Handbook of optical materials,* CRC press, 2002.

[108] C. Tsai, G. Liu, G. Fan, and Y. Lee, "Substrate-free large gap InGaN solar cells with bottom reflector", *Solid-State Electronics,* vol. 54(5), pp. 541-544, 2010.

[109] R. H. van Leest, G. J. Bauhuis, P. Mulder, R. van der Heijden, E. Bongers, E. Vlieg, and J. J. Schermer, "Effects of copper diffusion in gallium arsenide solar cells for space applications", *Solar Energy Materials and Solar Cells,* vol. 140, pp. 45-53, 2015.

[110] R. H. van Leest, K. de Kleijne, G. J. Bauhuis, P. Mulder, H. Cheun, H. Lee, W. Yoon, R. van der Heijden, E. Bongers, E. Vlieg, and J. J. Schermer, "Degradation mechanism(s) of GaAs solar cells with Cu contacts", *Physical Chemistry Chemical Physics,* vol. 18(15), pp. 10232-10240, 2016.

[111] N. Gruginskie, S. Van Laar, G. Bauhuis, P. Mulder, M. Van Eerden, E. Vlieg, and J. J. Schermer, "Increased performance of thin-film GaAs solar cells by rear contact/mirror patterning", *Thin Solid Films,* vol. 660, pp. 10-18, 2018.

[112] H. Okamoto, D. J. Chakrabarti, D. E. Laughlin, and T. B. Massalski, "The Au-Cu (gold-copper) system", *Journal of Phase Equilibria,* vol. 8(5), pp. 454, 1987.

[113] G. J. Bauhuis, P. Mulder, E. J. Haverkamp, Huijben, J. C. C. M., and J. J. Schermer, "26.1% thin-film GaAs solar cell using epitaxial lift-off", *Solar Energy Materials and Solar Cells,* vol. 93(9), pp. 1488-1491, 2009.

[114] G. Stareev, H. Künzel, and G. Dortmann, "A controllable mechanism of forming extremely low-resistance nonalloyed ohmic contacts to group III-V compound semiconductors", *Journal of Applied Physics,* vol. 74(12), pp. 7344-7356, 1993.

[115] D. K. Schroder, *Semiconductor material and device characterization,* John Wiley & Sons, 2006.

[116] I. G. Akdogan and M. A. Parker, "Au-Cu Ohmic Contacts for p+ GaAs", *Electrochemical and Solid-State Letters,* vol. 8(5), pp. G106-G108, 2005.

[117] E. Yablonovitch and O. Miller, "The influence of the $4n^2$ light trapping factor on ultimate solar cell efficiency", in Proceedings of *Optics for Solar Energy,* Tucson, Arizona, USA, pp. SWA1, 2010.

[118] F. Elsehrawy, F. Cappelluti, T. Aho, T. Niemi, V. Polojärvi, and M. Guina, "Back grating optimization for light trapping in thin-film quantum dot solar cells", in Proceedings of *19th Italian National Conference on Photonic Technologies,* Padua, Italy, pp. 34, 2017.

[119] C. Heine and R. H. Morf, "Submicrometer gratings for solar energy applications", *Applied Optics,* vol. 34(14), pp. 2476-2482, 1995.

[120] A. Cattoni, H. Chen, J. Goffard, R. De Lépinau, B. Behaghel, C. Dupuis, N. Bardou, and S. Collin, "Multiresonant light trapping in ultra-thin GaAs and CIGS solar cells", in Proceedings of *Optical Nanostructures and Advanced Materials for Photovoltaics,* Boulder, CO, USA, pp. PW3A2, 2017.

[121] U. Palanchoke, V. Jovanov, H. Kurz, P. Obermeyer, H. Stiebig, and D. Knipp, "Plasmonic effects in amorphous silicon thin film solar cells with metal back contacts", *Optics express,* vol. 20(6), pp. 6340-6347, 2012.

[122] A. Musu, F. Cappelluti, T. Aho, V. Polojärvi, T. Niemi, and M. Guina, "Nanostructures for light management in thin-film GaAs quantum dot solar cells", in Proceedings of *Light, Energy and the Environment Congress,* Leipzig, Germany, pp. JW4A-45, 2016.

[123] E. Antolín, A. Martí, C. D. Farmer, P. G. Linares, E. Hernández, A. M. Sánchez, T. Ben, S. I. Molina, C. R. Stanley, and A. Luque, "Reducing carrier escape in the InAs/GaAs quantum dot intermediate band solar cell", *Journal of Applied Physics,* vol. 108(6), pp. 064513, 2010.

[124] A. Tukiainen, A. Aho, T. Aho, V. Polojärvi, and M. Guina, "Design considerations on GaInNAs solar cells with back surface reflectors", in Proceedings of *IEEE 44th Photovoltaic Specialist Conference (PVSC),* Washington, DC, USA, pp. 297-300, 2017.

[125] SU-8 Photoresists,
available: https://kayakuam.com/products/su-8-photoresists, cited 23.6.2020.

[126] M. Rönnelid, M. Adsten, T. Lindström, P. Nostell, and E. Wäckelgård, "Optical scattering from rough-rolled aluminum surfaces", *Applied Optics,* vol. 40(13), pp. 2148-2158, 2001.

[127] Ormocomp,
available: https://www.microresist.de/en/produkt/ormocomp, cited 23.6.2020.

[128] F. Haug, T. Söderström, O. Cubero, V. Terrazzoni-Daudrix, and C. Ballif, "Plasmonic absorption in textured silver back reflectors of thin film solar cells", *Journal of Applied Physics,* vol. 104(6), pp. 064509, 2008.

[129] E. D. Palik, *Handbook of optical constants of solids,* Academic press, 1998.

[130] M. Vaughan, *The Fabry-Perot interferometer: history, theory, practice and applications,* CRC press, 1989.

[131] C. Algora, "Reliability of III-V concentrator solar cells", *Microelectronics Reliability,* vol. 50(9-11), pp. 1193-1198, 2010.

[132] M. Salzberger, M. Rutzinger, C. Nömayr, P. Lugli, and C. G. Zimmermann, "Voltage-dependent photocurrent in irradiated GaAs solar cells", *Progress in Photovoltaics: Research and Applications,* vol. 26(5), pp. 317-323, 2018.

[133] C. Kerestes, C. D. Cress, B. C. Richards, D. V. Forbes, Y. Lin, Z. Bittner, S. J. Polly, P. Sharps, and S. M. Hubbard, "Strain effects on radiation tolerance of triple-junction solar cells with InAs quantum dots in the GaAs junction", *IEEE journal of Photovoltaics,* vol. 4(1), pp. 224-232, 2013.

[134] R. Campesato, A. Tukiainen, A. Aho, G. Gori, R. Isoaho, E. Greco, and M. Guina, "31% European InGaP/GaAs/InGaAs Solar Cells for Space Application", *E3S web of conferences,* vol. 16, pp. 3003, 2017.

[135] W. G. Spitzer and J. M. Whelan, "Infrared absorption and electron effective mass in n-type gallium arsenide", *Physical Review,* vol. 114(1), pp. 59, 1959.

[136] D. J. Friedman and J. M. Olson, "Analysis of Ge junctions for GaInP/GaAs/Ge three-junction solar cells", *Progress in Photovoltaics: Research and Applications,* vol. 9(3), pp. 179-189, 2001.

[137] A. Tukiainen, J. Lyytikäinen, T. Aho, E. Halonen, M. Raappana, F. Cappelluti, and M. Guina, "Comparison of 'shallow'and 'deep'junction architectures for MBE-grown InAs/GaAs quantum dot solar cells", in Proceedings of *IEEE 7th World Conference on Photovoltaic Energy Conversion (WCPEC),* Waikoloa, HI, USA, pp. 2950-2952, 2018.

[138] L. C. Hirst, M. K. Yakes, J. H. Warner, M. F. Bennett, K. J. Schmieder, R. J. Walters, and P. P. Jenkins, "Intrinsic radiation tolerance of ultra-thin GaAs solar cells", *Applied Physics Letters,* vol. 109(3), pp. 033908, 2016.

[139] F. Elsehrawy, T. Aho, T. Niemi, M. Guina, and F. Cappelluti, "Improved Light Trapping in Quantum Dot Solar Cells Using Double-sided Nanostructuring", in Proceedings of *Optics and Photonics for Energy and the Environment,* Singapore, Singapore, pp. JM4A. 5, 2018.

[140] M. Gioannini, A. P. Cedola, N. Di Santo, F. Bertazzi, and F. Cappelluti, "Simulation of quantum dot solar cells including carrier intersubband dynamics and transport", *IEEE Journal of Photovoltaics,* vol. 3(4), pp. 1271-1278, 2013.

[141] A. P. Cédola, D. Kim, A. Tibaldi, M. Tang, A. Khalili, J. Wu, H. Liu, and F. Cappelluti, "Physics-based modeling and experimental study of si-doped inas/gaas quantum dot solar cells", *International Journal of Photoenergy,* vol. 2018, pp. 7215843, 2018.

[142] A. Khalili, A. Tibaldi, F. Elsehrawy, and F. Cappelluti, "Multiscale device simulation of quantum dot solar cells", in Proceedings of *Physics, Simulation, and Photonic Engineering of Photovoltaic Devices VIII,* San Francisco, CA, USA, pp. 109131N, 2019.

[143] T. Li and M. Dagenais, "Below-bandgap absorption in InAs/GaAs self-assembled quantum dot solar cells", *Progress in Photovoltaics: Research and Applications,* vol. 23(8), pp. 997-1002, 2015.

[144] Y. Shoji, K. Watanabe, and Y. Okada, "Photoabsorption improvement in multi-stacked InGaAs/GaAs quantum dot solar cell with a light scattering rear texture", *Solar Energy Materials and Solar Cells,* vol. 204, pp. 110216, 2020.

[145] C. A. Gross and T. A. Roppel, *Fundamentals of electrical engineering,* CRC Press, 2012.

[146] F. Elsehrawy, A. Tibaldi, and F. Cappelluti, "Efficient multiphysics modeling of thin-film solar cells with periodically textured surfaces", in Proceedings of *Physics, Simulation, and Photonic Engineering of Photovoltaic Devices VIII,* San Francisco, CA, USA, pp. 109130K, 2019.

# PUBLICATIONS

# PUBLICATION
# I

## Enhancement of photocurrent in GaInNAs solar cells using Ag/Cu double-layer back reflector

Timo Aho, Arto Aho, Antti Tukiainen, Ville Polojärvi, Turkka Salminen, Marianna Raappana, and Mircea Guina

Applied Physics Letters, 109, pp. 251104 (2016)
DOI: 10.1063/1.4972850

APPLIED PHYSICS LETTERS **109**, 251104 (2016)

# Enhancement of photocurrent in GaInNAs solar cells using Ag/Cu double-layer back reflector

Timo Aho, Arto Aho, Antti Tukiainen, Ville Polojärvi, Turkka Salminen, Marianna Raappana, and Mircea Guina
*Optoelectronics Research Centre, Tampere University of Technology, FI-33720 Tampere, Finland*

(Received 20 October 2016; accepted 9 December 2016; published online 22 December 2016)

The effect of a Ag/Cu-based double-layer back reflector on current generation in GaInNAs single-junction solar cell is reported. Compared to Ti/Au reflector, the use of Ag/Cu led to a 28% enhancement of short-circuit current density, attaining a value of ~14 mA/cm$^2$ at AM1.5D (1000 W/m$^2$) under a GaAs filter. The enhanced current generation is in line with requirements for current-matching in GaInP/GaAs/GaInNAs triple-junction solar cells. The Ag/Cu reflectors also had a low contact resistivity of the order of $10^{-6}$ Ω·cm$^2$ and none of the samples exhibited notable peeling of metals in the adhesion tests. Moreover, no discernible diffusion of the metals into the semiconductor was observed after thermal annealing at 200 °C. [http://dx.doi.org/10.1063/1.4972850]

III–V multijunction solar cells are the solution of choice for space and concentrator photovoltaic (CPV) systems, owing to their high power-to-mass ratio, radiation durability, and high efficiency. The continuous progress of multijunction solar cell technology has reached a high level of maturity using approaches involving, e.g., GaInP/GaAs/GaInAs or GaInP/GaAs/Ge designs, which have enabled the efficiencies of over 30% for space[1] and over 40% for CPV.[2] However, these achievements are still far from the theoretical potential, prompting for new approaches to increase the number of junctions for better matching to the solar spectrum.[3] Amongst the recent approaches to increase the efficiency of multi-junction solar cells, the use of lattice-matched $Ga_{1-x}In_xN_yAs_{1-y}$ layers grown by molecular beam epitaxy (MBE) has emerged as very promising design.[4,5] More recently, a combination of MBE and metalorganic chemical vapor deposition (MOCVD) epitaxy was developed as a practical approach to fabricate GaInNAs-based solar cells, exploiting the key features that are established in the production of commercial solar cells.[6] The main advantages offered by GaInNAs rest upon their ability to tailor the bandgap in a wide range from approximately 0.8 eV to 1.42 eV while remaining lattice-matched to GaAs and Ge.[4,7] Despite the recent achievement and good potential for future developments, at high N compositions ($y \geq 0.04$) required for bandgaps below 0.9 eV, the photovoltaic operation of GaInNAs solar cells is reduced due to relatively low charge carrier lifetimes (below 1 ns) leading to short minority carrier diffusion lengths of under ~1 $\mu$m, and high p-type background doping of the order of $10^{16}$ cm$^{-3}$ or higher.[8–10] High background doping level narrows the depletion region, which together with the short diffusion length limits the thickness of an optimized absorption layer, resulting in lower quantum efficiencies.[9–12] To obtain wider depletion regions and higher quantum efficiencies, the p-type background doping should be reduced down to the order of $10^{15}$ cm$^{-3}$ or below, which still remains a challenging task at high N compositions ($y \geq 0.04$). This issue can be mitigated by adding a reflector on the back side of the solar cell that would allow the use of a thinner absorber with enhanced photogeneration.[13] Highly reflective back surface reflectors effectively double the absorption length in the photogenerating layer. As a result, the charge collection efficiency is improved, which increases the short-circuit current density ($J_{sc}$).[14] Furthermore, the open circuit voltage ($V_{oc}$) will theoretically increase as a consequence of higher effective light concentration in the junction and the absorption in average occurs closer to the depletion region, which decreases the nonradiative recombination.[15]

In this paper, we report the operation of a GaInNAs solar cell with a Ag/Cu back surface reflector. Amongst the options for developing non-alloyed back surface reflectors, Ag, Au, and Cu provide almost ideal reflectivity at wavelengths longer than 800 nm.[16] Au as a reflector material[17] is known to be expensive, and therefore, to reduce the solar cell fabrication costs the use of other metals, such as Ag and Cu, would be an attractive alternative. The Ag back reflector has already been reported to work well in GaAs and GaInP solar cells,[18,19] but Ag has not been applied to GaInNAs solar cells. Furthermore, Cu has also been used as a part of the back side contact in GaAs solar cells, but Cu is also known to diffuse easily into III–V semiconductors and thus to reduce the $V_{oc}$.[20–22] In our approach, we have studied GaInNAs solar cells with double-layer Ag/Cu reflectors exhibiting high reflectance, good adhesion, and low contact resistance. Moreover, a thin Ag layer acts as a diffusion barrier, preventing Cu diffusion into the semiconductor structure even when the cell is subjected to thermal annealing.

Single-junction GaInNAs solar cells were grown by MBE following the process described in Ref. 9. A generic sample structure is presented in Fig. 1. In our benchmark process, as a back contact we used Ti/Au annealed at 420 °C for 90 s to ensure formation of an ohmic contact. Here, we have replaced Ti/Au contact layers with higher-reflectivity metals and fabricated the contact without annealing. Four different metal reflectors were deposited using an electron

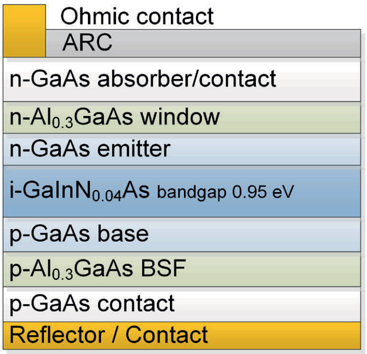

FIG. 1. Generic test structure of the back surface reflector cell. Light enters to the structure from the n-GaAs side.

beam evaporator: Ag/Cu/Ni/Au (denoted as Ag/Cu), Cu/Ni/Au (denoted as Cu), Au (100 nm), and Ti/Au (50 nm/100 nm). Thicknesses of individual layers for the Ag/Cu and Cu samples were: 100 nm for Cu layers, 10 nm for Ni, and 50 nm for Au. Moreover, for the Ag/Cu reflector, we studied three different Ag layers, with thicknesses of 10 nm, 30 nm, and 50 nm. The purpose of Ag is to act as a diffusion barrier for Cu and to provide high reflectance in combination with the Cu layer. The Cu layer acts as a current spreader and conductor. Ni is required between the Au and Cu layers as an adhesion layer and Au acts as a protective layer and bonding surface.

Indium contacts were deposited on the top of the solar cells and the surface was coated with a double-layer $TiO_2/SiO_2$ antireflection coating by an electron beam evaporator. External quantum efficiency (EQE) measurements were performed with a setup equipped with a 250 W quartz tungsten halogen lamp. The narrow excitation wavelength span for the probe beam was selected by using a Digikrom DK240 monochromator and an 800 nm long-pass filter placed before the monochromator. The signals from the solar cells and from the reference detectors were measured using an SRS SR830 lock-in amplifier and chopped light. A NIST-calibrated Ge reference detector was used for the whole wavelength range of 800–1500 nm.

Fig. 2 shows the EQE results of GaInNAs solar cells with the back reflectors. In addition, the reflectance results of double-side polished semi-insulating GaAs samples with back surface reflectors are shown in Fig. 2 for comparison of the optical properties of the reflectors. The reflectance was measured using a PerkinElmer Lambda 1050 spectrophotometer. For the Au, Ag/Cu, and Cu back reflector cells, EQE was drastically improved compared to reference Ti/Au. The greatest improvement in EQE is observed near the band edge of GaInNAs, where the absorption coefficient decreases and transmission increases; 52% improvement was achieved for the cell with 10 nm Ag/Cu compared to the cell with the Ti/Au reflector. The highest EQE was obtained for the samples with the Ag/Cu reflector, which is a consequence of higher reflectance of the back reflector. This means that the photons that are not absorbed in the first pass are effectively reflected back to the GaInNAs junction. The difference between the 10 nm, 30 nm, and 50 nm Ag/Cu reflectors is small, meaning that already a 10 nm layer of Ag is enough to preserve high reflectivity. After thermal annealing at 200 °C for 90 s, the 10 nm Ag/Cu sample maintained high EQE as shown in Fig. 2. This permits that the processing conditions at 200 °C do not adversely affect the functionality of the cell. The EQE of the solar cell with an Au reflector lies between the EQEs of cells with Ag/Cu and Ti/Au back side reflectors. Low EQE of the cell with the Ti/Au reflector can be explained by the fact that the light transmitted through the GaInNAs layer is largely absorbed in the metal layers.

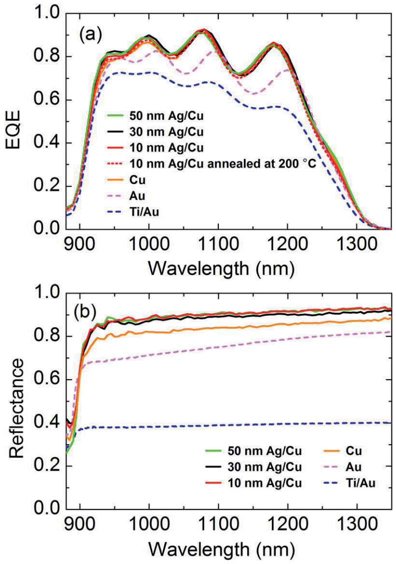

FIG. 2. (a) EQE of the GaInNAs solar cells with various back surface reflectors and (b) the reflectance of double-side polished semi-insulating GaAs samples with back surface reflectors and without ARC. The reflectance was measured through the GaAs from the top side. The correlation between EQE and the reflectance is apparent.

The $J_{sc}$ values at AM1.5G, AM1.5D, and AM0 spectral conditions[23] were deduced from the EQE measurements by integrating over the given spectrum and assuming a thick GaAs filter on top of GaInNAs cell. The results are shown in Table I. The solar cell with the 30 nm Ag/Cu reflector exhibited a $J_{sc}$ value of $\sim$14 mA/cm$^2$ at AM1.5D (1000 W/m$^2$), which is 28% higher compared to the reference solar cell with the Ti/Au reflector. These values are similar to the current that can be generated by GaInP/GaAs top cells, which is $\sim$14 mA/cm$^2$ at AM1.5D (1000 W/m$^2$).[24] The enhanced photocurrent of the GaInNAs solar cells with the back reflector is proven. This improvement is valid for the bottom junction of a multijunction solar cell. When comparing the conversion efficiency of an optimized GaInP/GaAs/GaInNAs triple-junction solar cell with the Ti/Au back reflector to the cell with the Au/Cu back reflector, 10 percentage points higher efficiency would be reached at $\sim$1000× AM1.5D resulting in an efficiency of 45% instead of 35%.

Back reflectors that are simultaneously used as ohmic contacts require a low contact resistivity. Conventional ohmic

TABLE I. Measured contact resistivity results and $J_{sc}$ values at AM1.5G (1000 W/m$^2$), AM1.5D (1000 W/m$^2$), and AM0 (1366 W/m$^2$) calculated from the EQE data.

| Back Surface Reflector | Contact Resistivity (Ω·cm$^2$) | $J_{SC}$ AM1.5G (mA/cm$^2$) | $J_{SC}$ AM1.5D (mA/cm$^2$) | $J_{SC}$ AM0 (mA/cm$^2$) |
|---|---|---|---|---|
| Ti/Au | $3 \times 10^{-6}$ | 10.1 | 10.7 | 12.7 |
| Au | $1 \times 10^{-6}$ | 11.8 | 12.4 | 14.8 |
| Cu | $4 \times 10^{-6}$ | 12.8 | 13.4 | 15.9 |
| 10 nm Ag/Cu | $4 \times 10^{-6}$ | 12.9 | 13.6 | 16.1 |
| 10 nm Ag/Cu[a] | | 12.7 | 13.3 | 15.8 |
| 30 nm Ag/Cu | $4 \times 10^{-6}$ | 13.0 | 13.7 | 16.2 |
| 50 nm Ag/Cu | $5 \times 10^{-6}$ | 13.0 | 13.7 | 16.2 |

[a] Annealed at 200 °C for 90 s

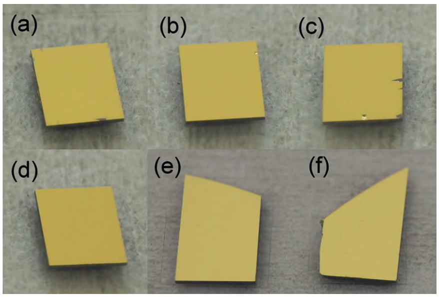

FIG. 3. The samples after the Scotch tape adhesion test. The back surface reflector materials were: (a) 50 nm Ag/Cu, (b) 30 nm Ag/Cu, (c) 10 nm Ag/Cu, (d) Cu, (e) Au, and (f) Ti/Au.

contacts are made of alloyed metals but annealing is shown to lower reflectivity due to the reduction of interface sharpness in comparison to non-alloyed contacts.[25] Although non-alloyed contacts usually suffer from higher contact resistivity,[26] high doping levels can be employed in GaAs to attain low contact resistivity.[20] Typical contact resistivities for p-GaAs are of the order of $10^{-5}$ Ω·cm$^2$ for non-alloyed metal contacts and $10^{-7}$ Ω·cm$^2$ for alloyed ones.[26,27] The contact resistivity of the Ag/Cu back contact reflectors was measured using the Transmission Line Method (TLM). The contact pads for TLM were fabricated by photolithography onto a separately grown p-type GaAs layer that had a doping level of $\sim 10^{20}$ cm$^{-3}$. The same metals as for the solar cells were deposited with the electron beam metal evaporator and the mesas were etched using inductively coupled plasma. As presented in Table I, all the reflectors showed low contact resistivity of the order of $10^{-6}$ Ω·cm$^2$, which are lower than reported contact resistivities of non-alloyed contacts.[27] These results show that an ohmic contact is formed even without annealing due to high doping in the GaAs layer and high reflectivity of the metal reflector is retained.

Adhesion of the metal reflectors was studied by the Scotch tape peel test.[28] None of the samples showed notable metal peeling, as revealed in Fig. 3. The Au reflector also passed the adhesion test even though Au has been reported to have weak adhesion to GaAs.[20] We observed a small piece of metal peeled off from the sample with 10 nm Ag/Cu as shown in Fig. 3(c). However, this was because of the small cracks on the edge of the sample caused by cleaving. The results indicate that an additional adhesion promoting metal layer, which could reduce the reflectivity, is not needed between the semiconductor and Ag.

The diffusion of Cu and Ag into the semiconductor was investigated by examining the cross-section of the metal-semiconductor interface with a focused ion beam scanning electron microscope (Zeiss Crossbeam 540 FIB-SEM) equipped with an energy-dispersive x-ray spectroscopy detector (EDS) from Oxford Instruments. Samples with similar metals to those for the solar cells were studied. Some of the samples were annealed at 200 °C and 420 °C for 90 s to test the effect of the processing conditions on the atomic diffusion.

The cross-section SEM images and EDS data of the metal-semiconductor interface are presented in Figs. 4 and 5.

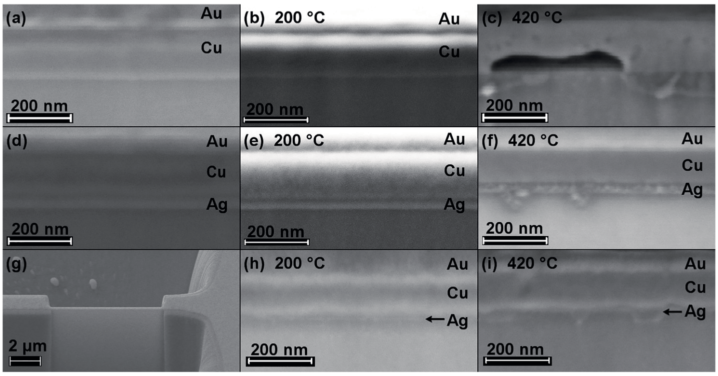

FIG. 4. SEM images of the cross-sections of metals on top of p-GaAs: (a) Cu, (b) Cu annealed at 200 °C, (c) Cu annealed at 420 °C, (d) 50 nm Ag/Cu, (e) 50 nm Ag/Cu annealed at 200 °C, (f) 50 nm Ag/Cu annealed at 420 °C, (g) large scale SEM image of the FIB-processed sample slice to clarify the measurement configuration (10 nm Ag/Cu annealed at 420 °C), (h) 10 nm Ag/Cu annealed at 200 °C, and (i) 10 nm Ag/Cu annealed at 420 °C.

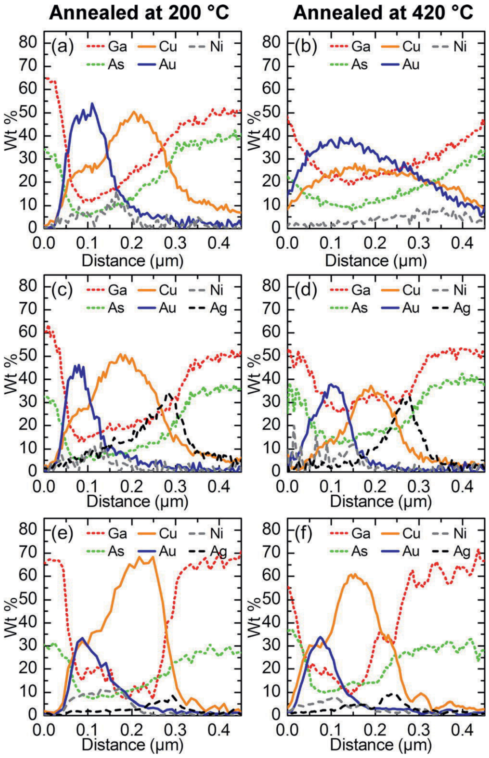

FIG. 5. FIB-EDS results from the cross-section back reflector metals: (a) Cu annealed at 200 °C, (b) Cu annealed at 420 °C, (c) 50 nm Ag/Cu annealed at 200 °C, (d) 50 nm Ag/Cu annealed at 420 °C, (e) 10 nm Ag/Cu annealed at 200 °C, and (f) 10 nm Ag/Cu annealed at 420 °C. The measurement starts from the surface of the sample and the distance on the x-axis represents the depth from the surface. The artefact signals of Ga and As at the surface originate from the electrons hitting the GaAs behind the sample slice made by FIB. The Ga signal is overemphasized due to Ga bombardment during the FIB. Samples were tilted during the measurement, which causes some inaccuracy to the distance.

Cu, Ni, and Au layers remained separated in the non-annealed Cu sample and in Cu sample annealed at 200 °C (Figs. 4(a) and 4(b)). This is also seen in the EDS data (Fig. 5(a)). However, in the SEM image for the sample annealed at 200 °C, the Cu-semiconductor interface is slightly blurred indicating that gradual mixing occurs. In the sample annealed at 420 °C (Fig. 4(c)), a clear mixing of metals and semiconductor was apparent in the SEM image and voids had been formed at the metal-semiconductor interface. Moreover, a color change of the sample surface was observed upon annealing at 420 °C, which is ascribed to alloy formation between Au and Cu.[29] In addition, the mixing of Au and Cu at 420 °C was also seen in EDS data presented in Fig. 5(b), in which Au and Cu peaks are clearly overlapping and the signals finally attenuate in the GaAs layer revealing Cu diffusion to GaAs. Consequently, according to the results, Cu as such is not suitable for the back surface reflector.

The SEM image of the non-annealed 50 nm Ag/Cu sample (Fig. 4(d)) showed that the Ag, Cu, Ni, and Au layers remained well separated and no diffusion occurred even after annealing at 200 °C (Fig. 4(e)). After annealing the 50 nm Ag/Cu sample at 420 °C (Fig. 4(f)), the layers are still separated but Ag has formed triangular spikes into GaAs. The EDS data, in Figs. 5(c) and 5(d), for the samples annealed at 200 °C and 420 °C, did not show mixing of Ag and GaAs, as indicated by the SEM images. Similar behavior was observed for the 10 nm Ag/Cu samples (Figs. 4(h), 4(i), 5(e), and 5(f)). Consequently, even 10 nm of Ag acts as an effective diffusion barrier for Cu and GaAs enabling process temperatures of at least 200 °C.

In conclusion, we have demonstrated the applicability of a double-layer Ag/Cu back contact reflector to enhance the EQE of the GaInNAs solar cell. The solar cell with the 30 nm Ag/Cu reflector resulted in the calculated $J_{sc}$ of $\sim$14 mA/cm$^2$ at AM1.5D (1000 W/m$^2$) under a GaAs filter. This value is 28% higher than that for the reference Ti/Au reflector. Furthermore, the adhesion tests showed no notable peeling of metals and the contact resistivity values were of the order of $10^{-6}$ $\Omega\cdot$cm$^2$. Moreover, the reflector withstands annealing temperatures of at least 200 °C. The results enable current-matching for GaInNAs materials with a high amount of N corresponding to bandgaps below 0.9 eV, ultimately allowing the development of lattice-matched solar cells with more than three junctions.

The research work of T. A. has been partially financed by European Union via Horizon 2020 research and innovation programme under Grant Agreement No. 687253. Additionally, T.A. acknowledges Ulla Tuominen Foundation and Jenny and Antti Wihuri Foundation for the financial support. The authors wish to thank Riku Isoaho, Jussi-Pekka Penttinen, and Joel Salmi for their technical support.

[1] S. Bailey, J. McNatt, R. Raffaelle, S. Hubbard, D. Forbes, L. Fritzenmeier, and W. Maurer, in *2009 IEEE 34th Photovoltaic Specialists Conference (PVSC), Philadelphia, PA, USA* (IEEE, 2009), pp. 001909–001913.
[2] M. A. Green, K. Emery, Y. Hishikawa, W. Warta, and E. D. Dunlop, Prog. Photovoltaics Res. Appl. **24**, 905 (2016).
[3] A. Luque, J. Appl. Phys. **110**, 031301 (2011).
[4] D. B. Jackrel, S. R. Bank, H. B. Yuen, M. A. Wistey, J. S. Jr. Harris, A. J. Ptak, S. W. Johnston, D. J. Friedman, and S. R. Kurtz, J. Appl. Phys. **101**, 114916 (2007).
[5] M. A. Green, K. Emery, Y. Hishikawa, W. Warta, and E. D. Dunlop, Prog. Photovoltaics Res. Appl. **21**, 1 (2013).
[6] A. Tukiainen, A. Aho, G. Gori, V. Polojärvi, M. Casale, E. Greco, R. Isoaho, T. Aho, M. Raappana, R. Campesato, and M. Guina, Prog. Photovoltaics Res. Appl. **24**, 914 (2016).
[7] D. J. Friedman, J. F. Geisz, S. R. Kurtz, and J. M. Olson, in *2nd World Conference and Exhibition on Photovoltaic Solar Energy Conversion, Vienna, Austria* (European Commission, 1998), pp. 6–10.
[8] A. J. Ptak, D. J. Friedman, S. R. Kurtz, and R. C. Reedy, J. Appl. Phys. **98**, 094501 (2005).
[9] A. Aho, V. Polojärvi, V.-M. Korpijärvi, J. Salmi, A. Tukiainen, P. Laukkanen, and M. Guina, Sol. Energy Mater. Sol. Cells **124**, 150 (2014).
[10] A. Gubanov, V. Polojärvi, A. Aho, A. Tukiainen, N. V. Tkachenko, and M. Guina, Nanoscale Res. Lett. **9**, 80 (2014).
[11] V. Polojärvi, A. Aho, A. Tukiainen, A. Schramm, and M. Guina, Appl. Phys. Lett. **108**, 122104 (2016).
[12] V. Polojärvi, A. Aho, A. Tukiainen, M. Raappana, T. Aho, A. Schramm, and M. Guina, Sol. Energy Mater. Sol. Cells **149**, 213 (2016).
[13] D. Redfield, Appl. Phys. Lett. **25**, 647 (1974).
[14] J. J. Schermer, G. J. Bauhuis, P. Mulder, E. J. Haverkamp, J. Van Deelen, A. T. J. Van Niftrik, and P. K. Larsen, Thin Solid Films **511–512**, 645 (2006).
[15] O. D. Miller, E. Yablonovitch, and S. R. Kurtz, IEEE J. Photovoltaics **2**, 303 (2012).

[16] M. J. Weber, *Handbook of Optical Materials* (CRC Press, 2002).

[17] T. Aho, A. Aho, A. Tukiainen, V. Polojarvi, J.-P. Penttinen, M. Raappana, and M. Guina, in *2015 IEEE 42nd Photovoltaic Specialist Conference (PVSC), New Orleans, LA, USA* (IEEE, 2015), pp. 1–4.

[18] C. Tsai, G. Liu, G. Fan, and Y. Lee, Solid-State Electron. **54**, 541 (2010).

[19] N. Vandamme, C. Hung-Ling, A. Gaucher, B. Behaghel, A. Lemaitre, A. Cattoni, C. Dupuis, N. Bardou, J. Guillemoles, and S. Collin, IEEE J. Photovoltaics **5**, 565 (2015).

[20] A. G. Baca and C. I. H. Ashby, in *Fabrication of GaAs devices* (IET, London, United Kingdom, 2005), pp. 200–211.

[21] R. H. van Leest, G. J. Bauhuis, P. Mulder, R. van der Heijden, E. Bongers, E. Vlieg, J. J. Schermer, and J. J. Schermer, Sol. Energy Mater. Sol. Cells **140**, 45 (2015).

[22] R. H. van Leest, K. de Kleijne, G. J. Bauhuis, P. Mulder, H. Cheun, H. Lee, W. Yoon, R. van der Heijden, E. Bongers, E. Vlieg, and J. J. Schermer, Phys. Chem. Chem. Phys. **18**, 10232 (2016).

[23] ASTM G173-03, *Standard Tables for Reference Solar Spectral Irradiances: Direct Normal and Hemispherical on 37° Tilted Surface* (ASTM International, 2008).

[24] A. Aho, A. Tukiainen, V. Polojärvi, and M. Guina, Nanoscale Res. Lett. **9**, 61 (2014).

[25] G. J. Bauhuis, P. Mulder, E. J. Haverkamp, J. C. C. M. Huijben, and J. J. Schermer, Sol. Energy Mater. Sol. Cells **93**, 1488 (2009).

[26] G. Stareev, H. Künzel, and G. Dortmann, J. Appl. Phys. **74**, 7344 (1993).

[27] I. G. Akdogan and M. A. Parker, Electrochem. Solid-State Lett. **8**, G106 (2005).

[28] K. Kuwahara, H. Hirota, and N. Umemoto, in *Adhesion Measurement of Thin Films, Thick Films, And Bulk Coatings* (ASTM Special Technical Publication, Philadelphia, PA, 1978), pp. 198–231.

[29] H. Okamoto, D. J. Chakrabarti, D. E. Laughlin, and T. B. Massalski, J. Phase Equilib. **8**, 454 (1987).

# PUBLICATION
# II

## Comparison of metal/polymer back reflectors with half-sphere, blazed, and pyramid gratings for light trapping in III–V solar cells

Timo Aho, Mircea Guina, Farid Elsehrawy, Federica Cappelluti, Marianna Raappana, Antti Tukiainen, A. B. M. Khairul Alam, Ismo Vartiainen, Markku Kuittinen, and Tapio Niemi

Optics Express, 26(6), pp. A331–A340 (2018)
DOI: 10.1364/OE.26.00A331

**Research Article** Vol. 26, No. 6 | 19 Mar 2018 | OPTICS EXPRESS A331

Optics EXPRESS

# Comparison of metal/polymer back reflectors with half-sphere, blazed, and pyramid gratings for light trapping in III-V solar cells

TIMO AHO,[1,*] MIRCEA GUINA,[1] FARID ELSEHRAWY,[2] FEDERICA CAPPELLUTI,[2] MARIANNA RAAPPANA,[1] ANTTI TUKIAINEN,[1] A. B. M. KHAIRUL ALAM,[3] ISMO VARTIAINEN,[4] MARKKU KUITTINEN,[3] AND TAPIO NIEMI[1]

[1] *Optoelectronics Research Centre, Laboratory of Photonics, Tampere University of Technology, P.O. Box 527, FI-33101 Tampere, Finland*
[2] *Department of Electronics and Telecommunications, Politecnico di Torino, Corso Duca degli Abruzzi 24, 10129 Torino, Italy*
[3] *Institute of Photonics, University of Eastern Finland, P.O. Box 111, FI-80101 Joensuu, Finland*
[4] *Dispelix Oy, Spektri Business Park - Duo, Metsänneidonkuja 6, FI-02130 Espoo, Finland*
[*] *timo.a.aho@tut.fi*

**Abstract:** We report on the fabrication of diffraction gratings for application as back contact reflectors. The gratings are designed for thin-film solar cells incorporating absorbers with bandgap slightly lower than GaAs, i.e. InAs quantum dot or GaInNAs solar cells. Light trapping in the solar cells enables the increase of the absorption leading to higher short circuit current densities and higher efficiencies. We study metal/polymer back reflectors with half-sphere, blazed, and pyramid gratings, which were fabricated either by photolithography or by nanoimprint lithography. The gratings are compared in terms of the total and the specular reflectance, which determine their diffraction capabilities, i.e. the feature responsible for increasing the absorption. The pyramid grating showed the highest diffuse reflection of light compared to the half-sphere structure and the blazed grating. The diffraction efficiency measurements were in agreement with the numerical simulations. The validated model enables designing such metal/polymer back reflectors for other type of solar cells by refining the optimal dimensions of the gratings for different wavelength ranges.

**OCIS codes:** (040.5350) Photovoltaic; (050.1950) Diffraction gratings; (220.4000) Microstructure fabrication.

## References and links

1. S. Bailey, J. McNatt, R. Raffaelle, S. Hubbard, D. Forbes, L. Fritzenmeier, and W. Maurer, "The future of space photovoltaics," in *2009 IEEE 34th Photovoltaic Specialists Conference (PVSC)*, (IEEE, 2009), pp. 001909.
2. D. B. Jackrel, S. R. Bank, H. B. Yuen, M. A. Wistey, J. S. J. Harris, Jr., A. J. Ptak, S. W. Johnston, D. J. Friedman, and S. R. Kurtz, "Dilute nitride GaInNAs and GaInNAsSb solar cells by molecular beam epitaxy," J. Appl. Phys. **101**(11), 114916 (2007).
3. M. A. Green, K. Emery, Y. Hishikawa, W. Warta, and E. D. Dunlop, "Solar cell efficiency tables (version 41)," Prog. Photovolt. Res. Appl. **21**(1), 1–11 (2013).
4. A. Tukiainen, A. Aho, G. Gori, V. Polojärvi, M. Casale, E. Greco, R. Isoaho, T. Aho, M. Raappana, R. Campesato, and M. Guina, "High-efficiency GaInP/GaAs/GaInNAs solar cells grown by combined MBE-MOCVD technique," Prog. Photovolt. Res. Appl. **24**(7), 914–919 (2016).
5. A. J. Ptak, D. J. Friedman, S. R. Kurtz, and R. C. Reedy, "Low-acceptor-concentration GaInNAs grown by molecular-beam epitaxy for high-current pin solar cell applications," J. Appl. Phys. **98**(9), 094501 (2005).
6. A. Aho, V. Polojärvi, V. Korpijärvi, J. Salmi, A. Tukiainen, P. Laukkanen, and M. Guina, "Composition dependent growth dynamics in molecular beam epitaxy of GaInNAs solar cells," Sol. Energy Mater. Sol. Cells **124**, 150–158 (2014).
7. A. Gubanov, V. Polojärvi, A. Aho, A. Tukiainen, N. V. Tkachenko, and M. Guina, "Dynamics of time-resolved photoluminescence in GaInNAs and GaNAsSb solar cells," Nanoscale Res. Lett. **9**(1), 80 (2014).
8. V. Polojärvi, A. Aho, A. Tukiainen, A. Schramm, and M. Guina, "Comparative study of defect levels in GaInNAs, GaNAsSb, and GaInNAsSb for high-efficiency solar cells," Appl. Phys. Lett. **108**(12), 122104 (2016).

#319895 https://doi.org/10.1364/OE.26.00A331
Journal © 2018 Received 16 Jan 2018; revised 1 Mar 2018; accepted 4 Mar 2018; published 13 Mar 2018

9. V. Polojärvi, A. Aho, A. Tukiainen, M. Raappana, T. Aho, A. Schramm, and M. Guina, "Influence of As/group-III flux ratio on defects formation and photovoltaic performance of GaInNAs solar cells," Sol. Energy Mater. Sol. Cells **149**, 213–220 (2016).
10. T. Aho, A. Aho, A. Tukiainen, V. Polojärvi, T. Salminen, M. Raappana, and M. Guina, "Enhancement of photocurrent in GaInNAs solar cells using Ag/Cu double-layer back reflector," Appl. Phys. Lett. **109**(25), 251104 (2016).
11. D. Redfield, "Multiple-pass thin-film silicon solar cell," Appl. Phys. Lett. **25**(11), 647–648 (1974).
12. F. Cappelluti, M. Gioannini, G. Ghione, and A. Khalili, "Numerical study of thin-film quantum-dot solar cells combining selective doping and light-trapping approaches," in *2016 IEEE 43rd Photovoltaic Specialists Conference (PVSC),* (IEEE, 2016), pp. 1282–1286.
13. F. Cappelluti, D. Kim, M. van Eerden, A. P. Cédola, T. Aho, G. Bissels, F. Elsehrawy, J. Wu, H. Liu, P. Mulder, G. J. Bauhuis, J. J. Schermer, T. Niemi, and M. Guina, "Light-trapping enhanced thin-film III-V quantum dot solar cells fabricated by epitaxial lift-off," Sol. Energy Mater. Sol. Cells, in press (2018).
14. A. Luque and A. Martí, "Increasing the efficiency of ideal solar cells by photon induced transitions at intermediate levels," Phys. Rev. Lett. **78**(26), 5014–5017 (1997).
15. A. Mellor, A. Luque, I. Tobías, and A. Martí, "The feasibility of high-efficiency InAs/GaAs quantum dot intermediate band solar cells," Sol. Energy Mater. Sol. Cells **130**, 225–233 (2014).
16. F. Cappelluti, G. Ghione, M. Gioannini, G. J. Bauhuis, P. Mulder, J. J. Schermer, M. Cimino, G. Gervasio, G. Bissels, E. Katsia, T. Aho, T. Niemi, M. Guina, D. Kim, J. Wu, and H. Liu, "Novel concepts for high-efficiency lightweight space solar cells," in *E3S Web of Conferences, Vol. 16*, (ESA Publications Division, 2017), pp. 03007.
17. N. Baldock and M. Mokhtarzadeh-Dehghan, "A study of solar-powered, high-altitude unmanned aerial vehicles," Aircr. Eng. Aerosp. Technol. **78**(3), 187–193 (2006).
18. J. J. Schermer, G. J. Bauhuis, P. Mulder, E. J. Haverkamp, J. Van Deelen, A. T. J. Van Niftrik, and P. K. Larsen, "Photon confinement in high-efficiency, thin-film III–V solar cells obtained by epitaxial lift-off," Thin Solid Films **511**, 645–653 (2006).
19. S. Mokkapati and K. R. Catchpole, "Nanophotonic light trapping in solar cells," J. Appl. Phys. **112**(10), 101101 (2012).
20. E. Yablonovitch and O. Miller, "The Influence of the 4n2 Light Trapping Factor on Ultimate Solar Cell Efficiency," in *Optics for Solar Energy*, (Optical Society of America, 2010), paper SWA1.
21. F. Elsehrawy, F. Cappelluti, T. Aho, T. Niemi, V. Polojärvi, and M. Guina, " Back grating optimization for light trapping in thin-film quantum dot solar cells," in *19th Italian National Conference on Photonic Technologies* (2017), pp. 34.
22. A. Cattoni, H. Chen, J. Goffard, R. De Lépinau, B. Behaghel, C. Dupuis, N. Bardou, and S. Collin, "Multiresonant light trapping in ultra-thin GaAs and CIGS solar cells," in *Optical Nanostructures and Advanced Materials for Photovoltaics*, (Optical Society of America, 2017), paper PW3A.2.
23. U. Palanchoke, V. Jovanov, H. Kurz, P. Obermeyer, H. Stiebig, and D. Knipp, "Plasmonic effects in amorphous silicon thin film solar cells with metal back contacts," Opt. Express **20**(6), 6340–6347 (2012).
24. E. Antolín, A. Martí, C. D. Farmer, P. G. Linares, E. Hernández, A. M. Sánchez, T. Ben, S. I. Molina, C. R. Stanley, and A. Luque, "Reducing carrier escape in the InAs/GaAs quantum dot intermediate band solar cell," J. Appl. Phys. **108**(6), 064513 (2010).
25. F. Elsehrawy, T. Niemi, and F. Cappelluti, "Guided-mode resonance gratings for intermediate band quantum dot solar cells," in *Optical Nanostructures and Advanced Materials for Photovoltaics*, (Optical Society of America, 2017), paper PM3A.4.
26. A. Musu, F. Cappelluti, T. Aho, V. Polojärvi, T. Niemi, and M. Guina, "Nanostructures for light management in thin-film GaAs quantum dot solar cells," in *Light, Energy and the Environment*, (Optical Society of America, 2016), paper JW4A–45.
27. SU-8 negative epoxy resists, http://www.microchem.com/Prod-SU8_KMPR.htm, accessed December 2017.
28. OrmoComp UV inprint, http://www.microresist.de/en/product/hybrid-polymers-0, accessed January 2018.
29. E. D. Palik, *Handbook of optical constants of solids* (Academic press, 1997), pp. 492–443.
30. A. D. Rakić, A. B. Djurišic, J. M. Elazar, and M. L. Majewski, "Optical properties of metallic films for vertical-cavity optoelectronic devices," Appl. Opt. **37**(22), 5271–5283 (1998).
31. M. Peters, M. Rüdiger, D. Pelzer, H. Hauser, M. Hermle, and B. Bläsi, "Electro–optical modelling of solar cells with photonic structures," in *25th European PV Solar Energy Conference and Exhibition* (2010), pp. 87–91.

## 1. Introduction

Owing to their high power-to-weight ratio, radiation durability, and high efficiency, III-V solar cells are the solution of choice for space solar power applications. Multi-junction solar cells have shown efficiencies of over 30% under AM0 spectrum [1]. Further improvements are expected by employing lattice-matched $Ga_{1-x}In_xN_yAs_{1-y}$ sub-junctions grown by molecular beam epitaxy (MBE) [2–4]. The main advantage offered by GaInNAs is the ability to tailor the bandgap in the range from approximately 0.8 eV to 1.42 eV, while remaining lattice-matched to GaAs and Ge. However, at high N compositions ($y \geq 0.04$) required for bandgaps below 0.9 eV, the photovoltaic properties of GaInNAs solar cells typically degrade due to relatively high p-type background doping level and short minority carrier diffusion lengths (<1 μm) [5–7]. High background doping level narrows the depletion region, which together with the short diffusion length limits the thickness of the absorption layer, resulting in lower quantum efficieny [6–9]. This can be alleviated by reducing the thickness of the absorber but then employing light trapping techniques for boosting up the carrier generation [10]. In general, when employing the light management, the physical thickness of the absorption layer can be reduced without sacrificing the current generation [11].

Another promising approach is represented by III-V quantum dot solar cells (QDSCs), where QDs will increase the short circuit current density ($J_{sc}$) of the GaAs solar cell [12,13]. QDSCs are promising devices both for bandgap tuning in multijunction cells and for realizing intermediate band solar cells (IBSCs) [14]. IBSCs may overcome the efficiency limit of single-gap cells through the absorption of two below-gap photons corresponding to interband and intraband optical transitions (which roughly set in the near-infrared and mid-infrared ranges) enabled by the nanostructured material. Under such conditions, increased photon harvesting is attained maintaining a high open circuit voltage. However, light absorption in the QD sheets is relatively low [15], which can again be mitigated by designs providing light trapping, as for example in the thin-film QDSC presented in Fig. 1.

Employing light trapping with substrate removal provides means for flexible, thinner, and lighter devices with high power-to-weight ratio. This approach enables fabrication of very thin solar cells, which would be beneficial e.g. for space and unmanned aerial vehicle applications [16,17].

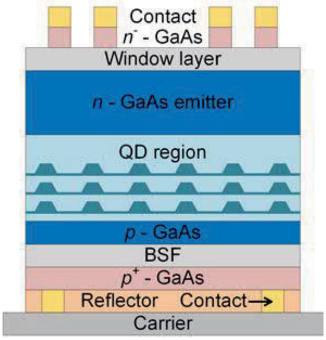

Fig. 1. Schematic structure of a thin-film QDSC employing light trapping.

As the simplest approach for improving the absorption, highly reflective planar back reflectors could effectively double the length of the optical path, increasing the $J_{sc}$. This approach has been demonstrated for GaAs solar cells [18], GaInNAs solar cells [10], and QDSCs [13]. The length of the optical path can be increased even more with a back reflector grating that induce light diffraction, of which various approaches have been published [19–21]. In connection with the III-V solar cells, we note for the recent work introducing nanostructures in GaAs solar cells [22].

Here, we concentrate on grating types with periods larger than the wavelength in order to have wider wavelength range in which the performance of the diffractive gratings is optimal. When the gratings are directly structured into the semiconductor, parasitic losses may occur due to surface plasmon effect resulting from the large microstructured interface area between the semiconductor and the metal [19]. However, one can use an interlayer between the semiconductor and the metal to alleviate the parasitic losses [23]. In this paper, we compare the diffraction properties of various backside gratings fabricated either by photolithography or by nanoimprint lithography (NIL) onto a polymer. Photolithography was used as a fabrication method for photoresists and NIL was used for NIL photoresist deposited on GaAs. To study the diffraction properties of the gratings, semi-insulating GaAs (SI-GaAs) was used as a substrate, since it is almost transparent for wavelengths above 900 nm. Thus, the comparison of the gratings using reflectance measurements is possible. The gratings were optimized for light trapping at the wavelengths corresponding to the energies slightly below the bandgap of GaAs. In particular, the gratings are designed for enhancing interband transitions of typical InAs/GaAs QDSCs in the wavelength range of 900 nm – 1200 nm [13,24]. While this is sufficient for optimizing QDSCs working in the single-gap limit [13], the ideas presented in this work should be further developed to devise suitable strategies for the simultaneous enhancement of QD intersubband transitions, involving longer wavelengths [15,25].

## 2. Design and experiments

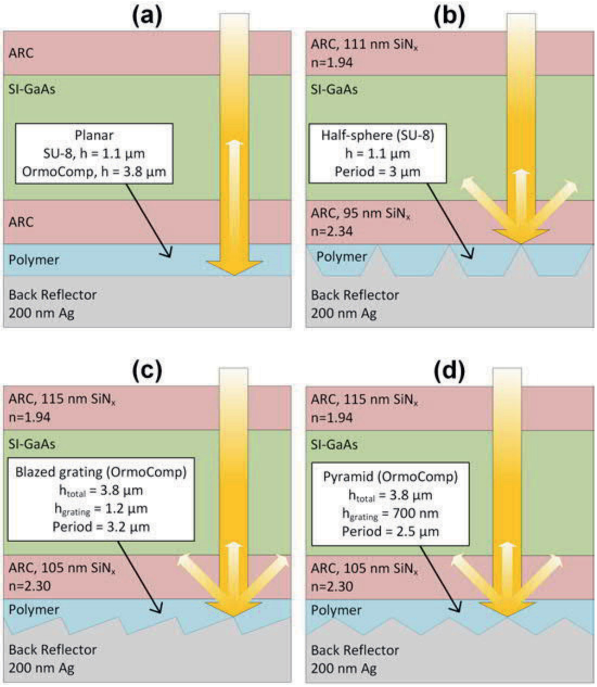

Fig. 2. The schematic drawing of the structures. (a) The planar reflector with SU-8 or OrmoComp layer, (b) the reflector with the half-sphere grating, (c) the reflector with the blazed grating, and (d) the reflector with the pyramid grating.

In this study, different structures were simulated and fabricated for assessing diffraction efficiencies and their dependence on the design features. Musu et al. [26] and Elsehrawy et al. [21] have simulated the gratings for the back reflector structures to find the optimum dimensions for absorption near the GaAs absorption edge. According to these simulations, the maximum photocurrent is achieved when the height/period aspect ratio is 0.32-0.38, which was employed to fabricate the gratings in this work. As substrate, we used double-sided polished SI-GaAs with a thickness of 350 µm. Single-layer $SiN_x$ antireflection coatings (ARCs) were deposited by plasma enhanced chemical vapor deposition on both sides of the substrate. The front ARC was optimized to minimize the reflectance at the air/GaAs interface, while the backside ARC was optimized to minimize the reflectance at the GaAs/polymer interface. The properties of the $SiN_x$ layers were tuned by varying the process parameters such as $NH_3$ and $SiH_4$ gas flows and deposition time. The ARC thicknesses and refractive indices are presented in Fig. 2, which also introduces the three structures and the planar references.

### *2.1 Half-sphere grating*

In the first approach, the photonic grating was fabricated by photolithography using a commercial epoxy based negative photoresist, SU-8 (MicroChem Corp.), which is commonly used in the electronic industry. SU-8 is chemically and mechanically stable and has low absorbance at least in the wavelength range from 400 nm to 1600 nm [27]. A sample with the planar SU-8 layer, shown in Fig. 2(a), was used as reference. A photolithography mask with the square openings of size $2 \times 2$ $\mu m^2$ and with 3 µm periodicity was used to obtain the desired half-sphere structure by varying photolithography process parameters, such as spin coating speed, exposure time, and baking temperatures. The fabricated half-spheres have height of 1.1 µm and period of 3 µm. The schematic drawing of the half-sphere grating is presented in Fig. 2(b). To realize the reflector, 200 nm Ag was deposited using electron beam evaporation on top of the polymer layer.

### *2.2 Blazed grating and pyramid grating*

In the second and the third approach, a commercial OrmoComp NIL photoresist (Micro Resist Technology GmbH) [28] was used for two different microstructures: blazed grating in Fig. 2(c), and pyramid grating in Fig. 2(d). A commercial master (Thorlabs) and an in-house fabricated Si master were used for the blazed grating and the pyramid grating, respectively. The Si master was fabricated in two steps. First, the structure was patterned with electron beam lithography and transferred into Si by anisotropic wet etching. With this, pyramids were obtained, but the height and the aspect ratio of the pyramids were not appropriate. In order to achieve the required dimensions, the pattern was imprinted onto NIL photoresist and dry etched with desired selectivity into another Si wafer, leading to the final master. In the NIL processes, the gratings from the masters were transferred into polydimethylsiloxane stamps, which were used for imprinting the gratings into the NIL photoresist. The fabricated blazed grating has height of 1.2 µm and period of 3.2 µm and the pyramid grating has height of 700 nm and period of 2.5 µm. On top of the polymer layer, 200 nm Ag was deposited using electron beam evaporation.

### *2.3 Characterization of the gratings*

The gratings were characterized with a Wyko NT1100 optical profilometer (Veeco Instruments Inc.) and with a scanning electron microscope (SEM) (Ultra-55, Carl Zeiss). The specular reflectance at 8° incident angle was measured with a PerkinElmer Lambda 1050 spectrophotometer. In addition, the total reflectance was measured with the integrating sphere module of the spectrophotometer. The diffuse reflectance can be retrieved by comparing the specular reflectance and the total reflectance. All the measurements were conducted through the SI-GaAs wafer and the performance of the back reflectors were evaluated at the wavelengths for which SI-GaAs is transparent.

To quantify the amount of diffracted light, the spectral diffraction efficiency was measured at diffraction orders of $m = 0, \pm 1$, and $\pm 2$. This measurement was carried out by variable angle measurement technique where the sample is illuminated by a white light beam at an incident angle of 8°. Diffracted light is collected at variable angles from 8° to 48° with an optical fiber connected to a spectrometer. As a result, the diffraction efficiency is defined as the diffracted power divided by the incident power. With our system, only the diffraction orders within the escape cone of the SI-GaAs wafer can be measured.

### *2.4 Simulations*

The grating structures were simulated using the rigorous coupled-wave analysis method (RCWA) with the RSoft DiffractMOD software (Synopsys) and the planar structures were analyzed with transfer-matrix method. The gratings exhibit both 2D (linear gratings) and 3D (crossed gratings) configurations. In the 2D simulations, the results are an average of the TE and TM polarizations for each of the diffraction orders. In the 3D case, the gratings are symmetric and therefore both polarizations are equal for the direct angle of incidence.

The simulated gratings have the nominal geometrical features, i.e. flattening and rounding of the grating shape due to processing imperfections were not taken into account in the simulations. Numerically, the grating structure is approximated by a layered geometry with a spatial resolution of 70-75 nm. All the presented simulations use 10 harmonics for each in-plane direction. The optical model for GaAs is obtained from [29] and for Ag from [30], while constant real refractive indices are used for the ARC layers (see values in Fig. 2) and the polymers ($n = 1.51$).

One limitation of the RCWA method lies in the simulation of structures thicker than the coherence length of sunlight (~1 μm), because fictitious interference effects cause high-frequency noise [31]. Such artifacts can be eliminated by using e.g. the methodology presented in [31]. In this work, the results were obtained by varying the substrate thickness of ± 5 μm in 5 steps and averaging across the simulations. Further reduction of interference effects was then achieved by averaging the calculated reflectance spectra and diffraction efficiency over 10 nm wavelength interval.

## 3. Results and discussion

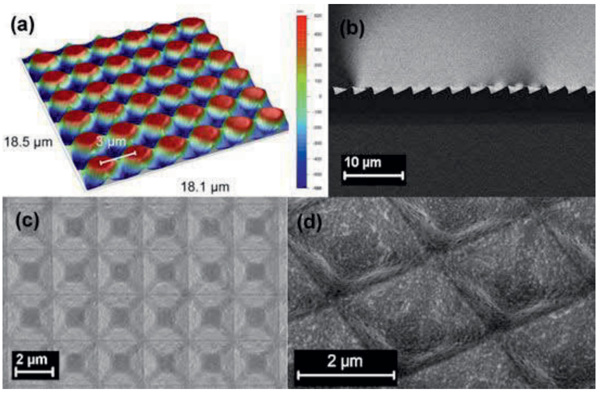

Fig. 3. (a) Optical profilometer image of the half-sphere structure, (b) Cross-sectional SEM image of the blazed grating, (c) and (d) SEM images of the pyramid grating.

Figure 3 shows the structural details of the three experimental structures: half-sphere, blazed grating, and pyramid grating. The top of the half-sphere appeared slightly flattened, as shown in the optical profilometer measurement in Fig. 3(a). The SEM images of the pyramid grating, presented in Fig. 3(c) and 3(d), are taken from the back surface of the sample where 200 nm Ag is evaporated, whereas the blazed grating image in Fig. 3(b) is the cross-section of the polymer without Ag. The pyramid grating shows flattened peak. This was already observed in the Si master, which means that the transfer of the pattern was successful and the flattening is due to the Si master.

### *3.1 Half-sphere grating results*

The reflectance measurement results of the half-sphere grating are presented in Fig. 4, where the difference between the total and the specular reflectance represents the diffuse reflectance. A strong interband absorption of light into SI-GaAs is observed in the wavelengths below 900 nm, as expected. The half-sphere grating shows high diffuse reflectance, which is desired for diffraction gratings. However, a local maximum in the specular reflectance is observed, decreasing the diffuse reflectance at the target wavelength range of 950nm-1150 nm. The planar structures used as reference showed high specular reflectance and ~10% higher total reflectance. This difference is possibly originating from the diffuse reflectance, which may occur also at planar surfaces due to scattering.

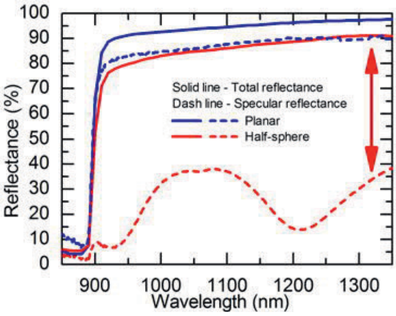

Fig. 4. Total and specular reflectance of the half-sphere structure and the planar reference. The red double-headed arrow represents the diffuse reflectance.

Figure 5 shows the measured and the 2D simulated diffraction efficiency of the half-sphere structure. The results show good correlation between measurements and simulations. Significant power coupling to the first two diffraction orders is observed. In addition, the measured diffraction efficiency of the zero order is in agreement with the specular reflectance measurements presented in Fig. 4.

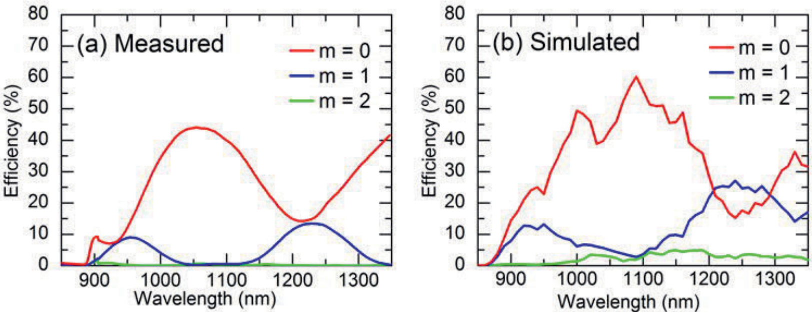

Fig. 5. The measured (a) and the simulated (b) diffraction efficiency of the half-sphere structured sample.

### *3.2 Blazed grating and pyramid structure results*

The reflectance measurements of the blazed grating and the pyramid grating are compared in Fig. 6(a). According to the measurements, the pyramid grating shows the highest diffuse reflectance when compared to the blazed grating or the half-sphere structure. Also, the blazed grating showed low specular reflectance, which is beneficial for high diffraction of light.

However, the total reflectance of the blazed grating was reduced compared to the pyramid grating. This means that there are some extra losses in the structure, potentially originating from the surface plasmon resonance (SPR) in the metal reflector. This behavior can be seen also in the simulations in Fig. 6(b). The simulated total reflectance for both the blazed grating and the pyramid grating is approximately 10 percentage points lower than the measured total reflectance, since simulations are probably overestimating the losses in the structured metallic reflector. In fact, the analysis of the calculated distribution of absorbed photon density (not shown here) pointed out large optical loss at the polymer/metal interface of the patterned structures, whereas marginal optical loss was observed in the reflector of the planar structure. The lower loss observed in the experiments could be attributed to a reduction of the SPR effect owing to the flattening of the fabricated structures with respect to the nominal ones. Moreover, some inaccuracy might originate also from the simple optical model adopted for the $SiN_x$ and polymer layers. Despite this, an overall good agreement between the measured and the simulated trends is achieved, supporting the conclusions of the diffractive properties of the structures.

As a final remark, for the planar reflector, the simulated total reflectance curve is flat, whereas the measured one is increasing towards higher wavelengths. This difference mostly arises from the residual absorption into SI-GaAs. From transmittance measurements across the SI-GaAs wafer, an extinction coefficient $k \sim 6 \times 10^{-6}$ was estimated, whereas the adopted GaAs optical model [29] uses $k = 1 \times 10^{-6}$ above 890 nm.

To display the limits imposed by the layer structure and the ARC, the front surface reflectance was simulated and is presented in Fig. 6(b). The single-layer ARC on top of the samples was designed to have the lowest reflectance at the wavelength of 900 nm. This means that part of light is reflected already from the surface of the sample without reaching the diffraction grating, increasing the measured specular reflectance.

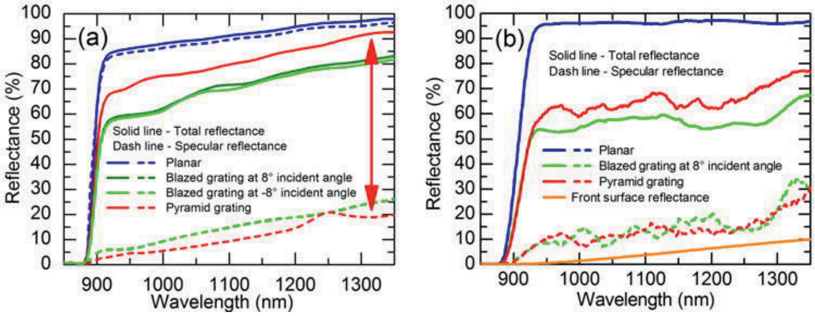

Fig. 6. The measured (a) and the simulated (b) reflectance of the blazed grating, the pyramid grating, and the planar reference. The difference between the total and the specular reflectance represents the amount of diffracted light (the red double-headed arrow).

The diffraction efficiency results of the blazed grating are presented in Fig. 7. Since the grating is asymmetric, the diffraction orders are not symmetric along the xz-plane, which is well observed at m = ± 1 and m = ± 2 diffraction orders. In addition, at m = 0, a small difference between the 8° and −8° angles of incident light is observed, due to the asymmetric grating. This difference seems to be negligible in the corresponding specular reflectance measurement shown Fig. 6(a), possibly due to the accuracy of the measurement. The diffraction orders of m = 0, + 1, and + 2 in the 2D simulations shown in Fig. 7(b) are supporting the measurements, even though they are not perfectly matching. In particular, simulations predict low frequency oscillations of the m = 0 spectrum, which were not observed in the experiments. Such oscillations could be attributed to the onset of a Fabry-Perot cavity effect in the polymer layer. The wavelength period (about 75-80 nm at $\lambda = 1050$

nm) is in fact well correlated with the polymer thickness and the oscillations were mainly visible in the TE polarization, which suffers less for the optical loss at the polymer/metal interface. On the other hand, such interference effects are not visible in the experimental data due to the non-uniformity of the fabricated polymer layer.

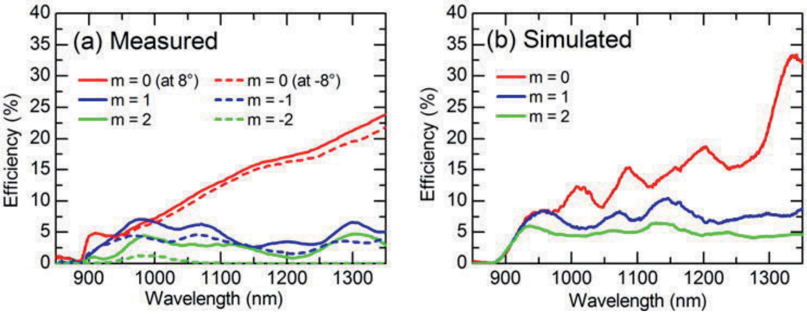

Fig. 7. The measured (a) and the simulated (b) diffraction efficiency of the blazed grating. The measurements are presented in two different directions whereas the simulations are only in single direction.

The diffraction efficiency results for the pyramid grating are presented in Fig. 8. In the measurements, power coupling to the first diffraction order is observed. The second diffraction order was not observed in the measurements, since they were performed up to 48° angle, where m = 2 is not yet present. However, according to the simulations, there is power coupling also to the second diffraction order. Furthermore, the m = 0 diffraction order is well in line with the specular reflectance results, presented in Fig. 6(a).

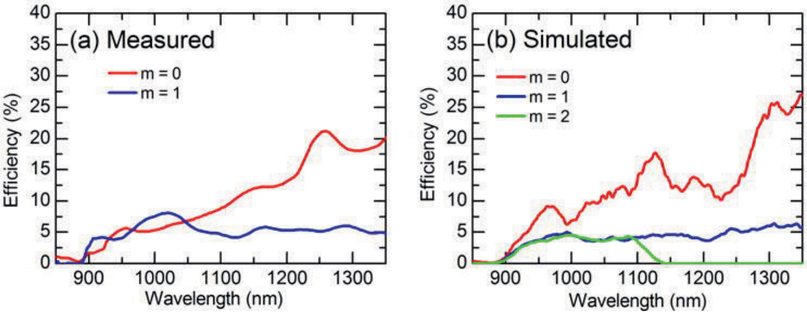

Fig. 8. The measured (a) and the simulated (b) diffraction efficiency of the pyramid grating. The measured diffraction efficiency is an average of the two directions.

### *3.3 Thin-film QD solar cell simulations*

Implementing the studied metal/polymer back reflectors in a thin-film QD solar cell can provide significant enhancement of the QD photogenerated current. As an example we can consider a QDSC structure with 2.6 µm thick GaAs active region embedding a stack of 20 InAs/GaAs QD layers with overall thickness of about 400 nm [21,26]. The structure includes top and bottom ARC layers similar to those reported in Fig. 2. Further details on the structure can be found in [21]. The QD stack's optical model was extracted from the external quantum efficiency measurements in [13]. Figure 9 shows the calculated absorbance spectrum for the QDSC in the substrate-based configuration and for two thin-film configurations, one with planar backside reflector and one integrating the pyramid backside grating described in Sec.

3.2. The grating has period of 3 µm and height of 0.75 µm and is terminated by a 200 nm thick Ag mirror. The absorbance spectrum is calculated by integrating the absorbed photon density only in the cell active region (i.e. low-doped GaAs and QD stack), and thus is not affected by optical loss in the contact and metal layers. The pyramid grating shows a significant increase of absorbance in the QD wavelength region with respect to the reference structures. The corresponding QD photocurrent density is calculated by integrating the absorbance over the AM1.5G sun spectrum in the 895 nm – 1200 nm range. The photocurrent per QD layer turns to be about 0.024 mA/cm$^2$, 0.038 mA/cm$^2$, and 0.095 mA/cm$^2$ for the substrate-based, thin-film with planar reflector and polymer/metal backside grating configurations, respectively. Therefore, the light trapping scheme allows for a four times increase of the current density from the quantum dot stack. This is a remarkable result if one considers the technological effort in terms of the epitaxial growth needed to increase by a factor of four the number of QD layers or the QD areal density. As reported in [13,26], further optimization of the structure and e.g. the use of higher index materials for the grating could yield even higher current enhancement.

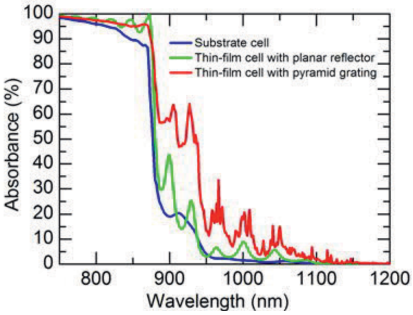

Fig. 9. Absorbance spectrum for QDSCs in three different configuration.

## 4. Conclusions

We studied structured metal/polymer back reflectors for the III-V solar cells with the half-sphere gratings, the blazed grating, and the pyramid grating. Efficient diffraction of light was observed for all the structures, indicating potential for improving the absorption and hence the current generation in thin-film solar cells. The pyramid grating showed the highest diffuse reflectance in the wavelengths corresponding to the photogeneration in GaInNAs solar cells and InAs/GaAs QDSCs. The microstructures can be applied to other types of solar cells by tuning the dimensions of the polymer structure to match the required wavelength range.

## Funding

European Union Horizon 2020 project TFQD (Grant Agreement No. 687253); ERC AdG project AMETIST (Grant Agreement No. ERC-2015-AdG 695116); Jenny and Antti Wihuri Foundation.

## Acknowledgments

Portions of this work were presented at the Light, Energy and the Environment Congress in 2017, paper JW5A.23. The author wish to thank Ville Polojärvi, Jussi-Pekka Penttinen, and Lauri Hytönen for their technical support.

# PUBLICATION
# III

## Back reflector with diffractive gratings for light-trapping in thin-film III–V solar cells

Timo Aho, Antti Tukiainen, Farid Elsehrawy, Sanna Ranta, Marianna Raappana,
Arto Aho, Riku Isoaho, Federica Cappelluti, and Mircea Guina

In Proceedings of IEEE European Space Power Conference (ESPC), pp. 1–4 (2019)
DOI: 10.1109/ESPC47532.2019.9049262

# Back Reflector with Diffractive Gratings for Light-Trapping in Thin-Film III-V Solar Cells

Timo Aho
*Optoelectronics Research Centre,*
*Physics Unit, Tampere University*
Tampere, Finland
timo.aho@tuni.fi

Antti Tukiainen
*Optoelectronics Research Centre,*
*Physics Unit, Tampere University*
Tampere, Finland
antti.tukiainen@tuni.fi

Farid Elsehrawy
*Department of Electronics and*
*Telecommunications*
*Politecnico di Torino*
Torino, Italy
farid.elsehrawy@polito.it

Sanna Ranta
*Optoelectronics Research Centre,*
*Physics Unit, Tampere University*
Tampere, Finland
sanna.ranta@tuni.fi

Marianna Raappana
*Optoelectronics Research Centre,*
*Physics Unit, Tampere University*
Tampere, Finland
marianna.raappana@tuni.fi

Arto Aho
*Optoelectronics Research Centre,*
*Physics Unit, Tampere University*
Tampere, Finland
arto.aho@tuni.fi

Riku Isoaho
*Optoelectronics Research Centre,*
*Physics Unit, Tampere University*
Tampere, Finland
riku.isoaho@tuni.fi

Federica Cappelluti
*Department of Electronics and*
*Telecommunications*
*Politecnico di Torino*
Torino, Italy
federica.cappelluti@polito.it

Mircea Guina
*Optoelectronics Research Centre,*
*Physics Unit, Tampere University*
Tampere, Finland
mircea.guina@tuni.fi

***Abstract*—We report on the development of light-trapping architectures applied to thin-film solar cells. In particular, we focus on enhancing the absorption at 1-eV spectral range for dilute nitride and quantum dot materials and report on the influence of planar back reflectors on the photovoltaic properties. Moreover, we discuss the properties of polymer diffraction gratings with enhanced light-trapping capability pointing to advantageous properties of pyramidal gratings. In order to understand the suitability of these polymer grating architectures for space applications, we have performed an electron irradiation study (1 MeV) revealing the absence of reflectance changes up to doses of 1×10$^{15}$ e$^{-}$/cm$^{2}$.**

***Keywords*—solar cell, III-V semiconductor, quantum dot, back reflector, optical design, diffractive grating, electron irradiation**

## I. INTRODUCTION

Space photovoltaic generators require solar cells with high efficiency, high power-to-weight ratio, and additional functionality in terms of flexibility. To this end, III-V solar cells with substrate removal and employing light-trapping to enhance photogeneration are gaining increased attention. For example, by using a highly reflective planar reflector on the backside of the solar cell, the length of the optical path is effectively doubled while further enhancement of the absorption can be obtained by using diffraction gratings combined with back reflector [1]. Planar reflectors have been initially utilized for thin-film single-junction GaAs solar cells [2], and more recently also applied to more advanced GaInNAs solar cells [3], and quantum dot (QD) solar cells [4]. Furthermore, different approaches utilizing diffraction gratings as back reflectors have been published [1], [5] and introduced as nanostructured back reflectors in GaAs solar cells [6].

In this work, we compare the performance of different planar reflectors and discuss the properties of diffraction gratings fabricated onto a polymer film deposited on the backside of the solar cells. The suitability of the polymer diffraction gratings for space application is assessed by performing electron irradiation study (1 MeV). In addition, we present the results of a thin-film QD solar cell with back reflector.

## II. BACK REFLECTORS

### *A. Planar Back Reflectors*

In an initial study, different planar metal back reflectors were compared. The Ag/Cu reflector showed high reflectance and resulted in enhanced external quantum efficiency (EQE) when compared to conventional Ti/Au back metals for dilute nitride (GaInNAs) solar cells as shown in Fig. 1. The EQE results show correlation with the reflectance results of the back reflectors, revealing higher reflectance of the reflector

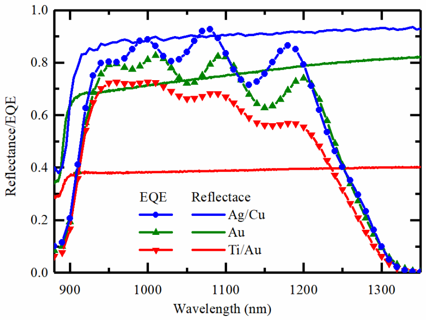

Fig. 1. Reflectance results of semi-insulating (SI) GaAs samples with the metal reflector are presented as solid lines and EQE results of GaInNAs solar cells with metal reflectors are presented as symbol and line.

---

The research work has been financed by European Union Horizon 2020 project TFQD (Grant Agreement No. 687253) and by ERC AdG project AMETIST (Grant Agreement No. ERC-2015-AdG 695116).

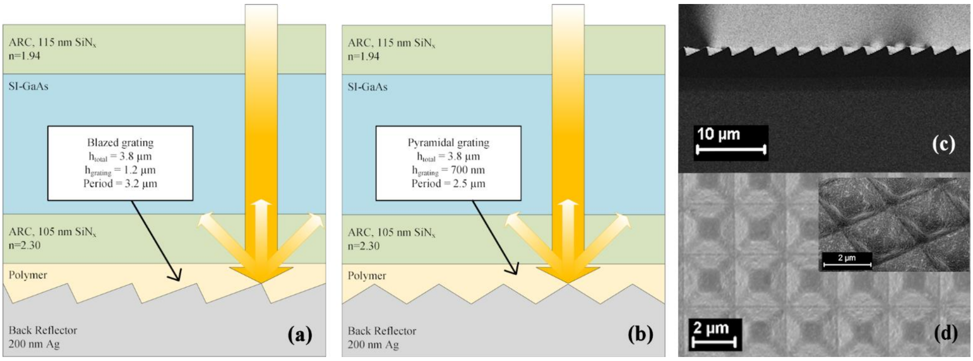

Fig. 2. Schematic drawing of (a) blazed gratings and (b) pyramidal gratings. SEM images of (c) blazed gratings and (d) pyramidal gratings.

resulted in higher EQE. Detailed study of the metal reflectors showed Ag/Cu and Au reflectors to be suitable for use in thin-film solar cell design [3]. In particular, the metal adhesion to semiconductor showed no peeling in the adhesion tests and the contact resistivity values were of the order of magnitude of $10^{-6}$ Ω/cm$^2$, which indicates to the formation of ohmic contact. Moreover, no discernible diffusion of metals into semiconductor was observed after thermal annealing (at 200 °C).

### *B. Back Reflector with Diffractive Gratings*

To further enhance the EQE, two different diffractive gratings, blazed and pyramidal, were fabricated using a commercial nanoimprint lithography (NIL) polymer (Ormocomp) with a Ag reflector [7]. If the diffractive gratings would be directly structured into the semiconductor, parasitic losses may occur due to surface plasmon effect resulting from the large microstructured interface area between the semiconductor and the metal [1]. For this reason, the diffractive gratings were fabricated onto a polymer, which acts as an interlayer, alleviating the parasitic losses. Schematic drawings and scanning electron microscopy (SEM) images of the fabricated grating structures are presented in Fig. 2, where the dimensions of the gratings are also shown. Prior to the fabrication of the diffractive gratings, optimum dimensions of the gratings for wavelength range of 900–1300 nm were simulated [8]. The simulation result pointed to the use of a height/period aspect ratio of 0.32–0.38, which was then used in the fabrication.

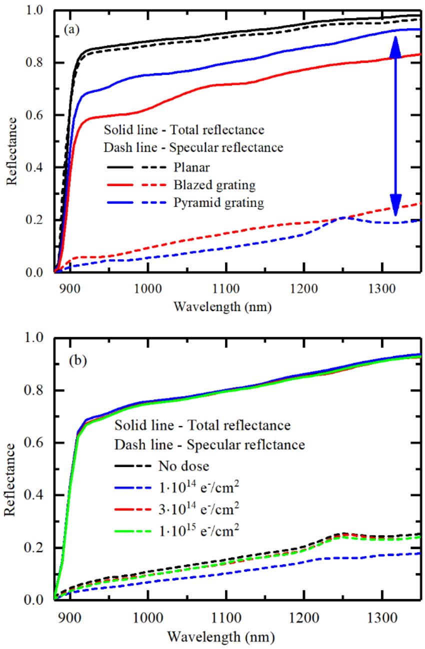

Fig. 3. (a) Reflectance of the diffractive grating structures. (b) The reflectance of the pyramidal grating structure after electron irradiation.

The diffractive gratings were characterized by measuring the total and specular (at 8° angle) reflectance spectra, which are presented in Fig. 3(a). The diffuse light is defined as the difference between the total and specular reflectance. The pyramidal grating showed higher diffuse reflectance when compared to blazed gratings in the wavelength range corresponding to dilute nitride junction and QD solar cells (900 nm to 1300 nm). Blazed grating showed also low specular reflectance, which is beneficial for high diffraction of light. However, the total reflectance of the blazed grating was reduced compared to the pyramidal grating, indicating some extra losses in the structure, potentially originating from parasitic absorption in the metal reflector. In addition to diffractive grating samples, a reference sample with planar polymer layer and Ag reflector was fabricated, showing almost identical specular and total reflectance spectra, verifying that only specular refection occurs in the planar reflector.

### *C. Electron Irradiation of the Diffractive Gratings*

The samples with pyramidal gratings were exposed to 1 MeV electron irradiation with three different doses, to study the suitability of the polymer gratings in the space environment. The total and specular reflectance results after the irradiation are presented in Fig. 3(b). These results reveal that the performance is mainly equivalent to the sample without the irradiation. Only for the sample exposed to the lowest dose ($1\times10^{14}$ e$^-$/cm$^2$), the specular reflectance was decreased, which might possibly originate from the fabrication of the sample or from the handling of the sample during irradiation, transport, and measurement. However, the higher dose samples showed no changes in the specular reflectance relative to the sample without any irradiation dose. These irradiation results indicate that the polymer are suitable for diffractive gratings in space solar cells in terms of radiation hardness.

## III. Thin-Film QD Solar Cell with Back Reflector

### A. *EQE of the QD Layers*

The effect of a planar back reflector on photocurrent generation in QD layers was experimentally investigated for InAs/GaAs solar cells containing 10 QD layers fabricated by molecular beam epitaxy [9]. QD solar cells were processed both as thin-film with Au reflector and wafer-based (i.e. with the substrate and without the back reflector) configurations. The measured EQE of the cells are presented in Fig. 4(a), which shows an increased photogeneration in the QD solar cell with back reflector when compared to QD solar cell without the reflector.

The photocurrent generation in QD layers (900–1100 nm) was calculated by integrating the EQE over the AM1.5D spectrum (1 000 W/m$^2$). The QD solar cell with reflector increased the current density ($J_{sc}$) component obtained from the QD layers by a factor of two when compared to the QD layers without the back reflector. The additional current density components to $J_{sc}$ were 0.35 mA/cm$^2$ and 0.17 mA/cm$^2$ for QD solar cell with the reflector and QD solar cell without the reflector, respectively.

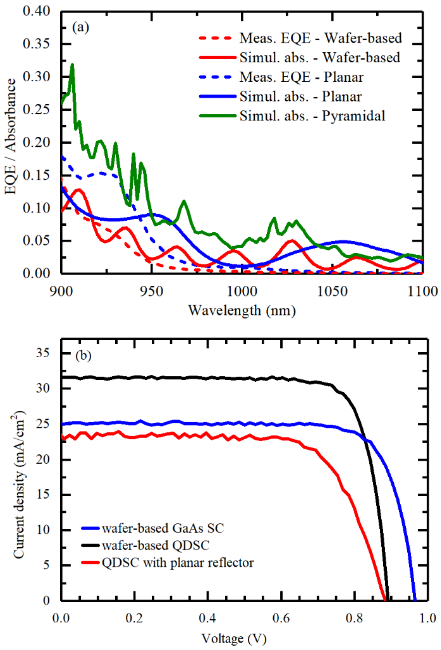

Fig. 4. *IV* results of the QD solar cell with and without planar back reflector and GaAs solar cell without reflector.

The absorbance spectrum of the QDs were simulated by using the rigorous coupled wave analysis method and the results are presented in Fig. 4(a). In addition to planar reflector, the absorbance of the QD solar cell utilizing a reflector with pyramidal grating was simulated, revealing a theoretical four-fold increase in the additional $J_{sc}$ component originating from the QD layers.

### B. *Current-Voltage Characteristics*

The measured current-voltage (*IV*) characteristics of the QD solar cells with and without the planar reflector are presented in Fig. 4(b). In addition, Fig. 4(b) shows the *IV* results of a GaAs solar cell, which was fabricated as a reference. The comparison of the measured $J_{sc}$ values is not simplistic due to the structural differences in the epitaxial layers of the QD solar cells and GaAs solar cell. For example, QD solar cell with back reflector has a 600 nm thick window layer, which absorbs photons lowering the $J_{sc}$ when compared to wafer-based QD solar cell, which has 20 nm thick window layer. In addition, the thicknesses of the p-GaAs base are 750 nm, 2 100 nm, and 900 nm for QD solar cell with reflector, wafer-based QD solar cell and wafer-based GaAs solar cell, respectively. However, despite these differences, the comparison of the open circuit voltage ($V_{oc}$) values is meaningful. The QD solar cell with back reflector has a very similar $V_{oc}$ to the QD solar cell with substrate, indicating that the high $V_{oc}$ is preserved during the thin-film process. The measured $V_{oc}$ of 0.884 V for thin-film QD solar cell with back reflector is high when compared to the reported values for thin-film QD solar cells [4], [10].

## IV. Conclusions

Diffraction grating structures implemented as back reflector were developed for light-trapping in thin-film III-V solar cells. Pyramidal gratings in Ormocomp polymer showed high diffuse reflectance and ability to enhance photocurrent generation in 1-eV cells, e.g. in multijunction solar cells with dilute nitride bottom junction and in QD solar cells. In addition, the polymer was resistant against the electron irradiation indicating possible suitability for space applications.

The effect of the planar back reflector on the performance of InAs/GaAs QD solar cell was studied by fabricating thin-film QD solar cell with back reflector. The photocurrent generation in the QD layers increased by a factor of two when QD solar cell with planar back reflector was compared to wafer-based configuration and at the same time the Voc remained high as in the wafer-based sample. The photocurrent generation could be further enhanced with a back reflector based on pyramidal gratings.

## Acknowledgment

The work has been financially supported and carried out as part of the European Union Horizon 2020 project TFQD (Grant Agreement No. 687253) and ERC AdG project AMETIST (Grant Agreement No. ERC-2015-AdG 695116). It is also a part of the Academy of Finland Flagship Programme PREIN #320168. T.A. thanks Jenny and Antti Wihuri Foundation for their financial support and would like to thank Ville Polojärvi and Elina Anttola for their technical support.

## References

[1] S. Mokkapati and K. Catchpole, "Nanophotonic light trapping in solar cells," J. Appl. Phys., vol. 112, pp. 101101, 2012.

[2] J. J. Schermer, G. J. Bauhuis, P. Mulder, E. J. Haverkamp, J. Van Deelen, Van Niftrik, A. T. J., and P. K. Larsen, "Photon confinement in high-efficiency, thin-film III–V solar cells obtained by epitaxial lift-off," Thin Solid Films, vol. 511, pp. 645-653, 2006.

[3] T. Aho, A. Aho, A. Tukiainen, V. Polojärvi, T. Salminen, M. Raappana, and M. Guina, "Enhancement of photocurrent in GaInNAs solar cells using Ag/Cu double-layer back reflector," Appl. Phys. Lett., vol. 109, pp. 251104, 2016.

[4] F. Cappelluti, D. Kim, M. van Eerden, A. Cédola, T. Aho, G. Bissels, F. Elsehrawy, J. Wu, H. Liu, and P. Mulder, "Light-trapping enhanced thin-film III-V quantum dot solar cells fabricated by epitaxial lift-off," Sol. Energy Mater. Sol. Cells, vol. 181, pp. 83-92, 2018.

[5] E. Yablonovitch and O. Miller, "The influence of the 4n2 light trapping factor on ultimate solar cell efficiency," in proceedings of Optics for Solar Energy, pp. SWA1, 2010.

[6] A. Cattoni, H. Chen, J. Goffard, R. De Lépinau, B. Behaghel, C. Dupuis, N. Bardou, and S. Collin, "Multiresonant light trapping in ultra-thin GaAs and CIGS solar cells," in proceedings of Optical Nanostructures and Advanced Materials for Photovoltaics, pp. PW3A2, 2017.

[7] T. Aho, M. Guina, F. Elsehrawy, F. Cappelluti, M. Raappana, A. Tukiainen, A. K. Alam, I. Vartiainen, M. Kuittinen, and T. Niemi, "Comparison of metal/polymer back reflectors with half-sphere, blazed, and pyramid gratings for light trapping in III-V solar cells," Opt. Express, vol. 26, pp. A331-A340, 2018.

[8] F. Elsehrawy, F. Cappelluti, T. Aho, T. Niemi, V. Polojärvi, and M. Guina, "Back grating optimization for light trapping in thin-film quantum dot solar cells," in proceedings of 19th Italian National Conference on Photonic Technologies, pp. 34, 2017.

[9] A. Tukiainen, J. Lyytikäinen, T. Aho, E. Halonen, M. Raappana, F. Cappelluti, and M. Guina, "Comparison of ‘shallow’and ‘deep’junction architectures for MBE-grown InAs/GaAs quantum dot solar cells," in proceedings of 2018 IEEE 7th World Conference on Photovoltaic Energy Conversion (WCPEC)(A Joint Conference of 45th IEEE PVSC, 28th PVSEC & 34th EU PVSEC), pp. 2950-2952, 2018.

[10] T. Sogabe, Y. Shoji, P. Mulder, J. Schermer, E. Tamayo, and Y. Okada, "Enhancement of current collection in epitaxial lift-off InAs/GaAs quantum dot thin film solar cell and concentrated photovoltaic study," Appl. Phys. Lett., vol. 105, pp. 113904, 2014.

# PUBLICATION
# IV

## Thin-film InAs/GaAs quantum dot solar cell with planar and pyramidal back reflectors

Timo Aho, Farid Elsehrawy, Antti Tukiainen, Sanna Ranta, Marianna Raappana, Riku Isoaho, Arto Aho, Arttu Hietalahti, Federica Cappelluti, and Mircea Guina

Applied Optics, 59(21), pp. 6304–6308 (2020)
DOI: 10.1364/AO.396590

# PUBLICATION
# V

## High performance low-bandgap (0.8 eV) single junction GaInNAsSb solar cells incorporating Au-based back surface reflectors

Riku Isoaho, Timo Aho, Arto Aho, Jarno Reuna, Marianna Raappana, Antti Tukiainen, and Mircea Guina

Submitted to Solar Energy Materials and Solar Cells, 9th of July (2020)